Winter 2017

SELF-SIMILAR PROPERTIES AND LEADING BALANCE SCALING STRUCTURE OF WALL-BOUNDED TURBULENT FLOWS

Ang Zhou
University of New Hampshire, Durham

SELF-SIMILAR PROPERTIES AND LEADING BALANCE SCALING STRUCTURE OF WALL-BOUNDED TURBULENT FLOWS

BY

ANG ZHOU

B.S. Theoretical and Applied Mechanics
Sun Yat-sen University, China, 2010

DISSERTATION

Submitted to the University of New Hampshire

in Partial Fulfillment of the Requirements for the Degree of

Doctor of Philosophy

in

Mechanical Engineering

December 2017

The dissertation has been examined and approved in partial fulfillment of the requirements for the degree of Doctor of Philosophy in Mechanical Engineering by:

Dissertation Director, Joseph C. Klewicki
Professor of Mechanical Engineering
Professor of Integrated Applied Mathematics

Gregory P. Chini
Professor of Mechanical Engineering
Professor of Integrated Applied Mathematics

John P. McHugh
Associate Professor of Mechanical Engineering
Associate Professor of Integrated Applied Mathematics

Christopher M. White
Associate Professor of Mechanical Engineering

Martin Wosnik
Associate Professor of Mechanical Engineering

John Gibson
Associate Professor of Mathematics & Statistics
Associate Professor of Integrated Applied Mathematics

In November 2017

Original approval signatures are on file with the University of New Hampshire Graduate School.

"Live Free or Die. This is New Hampshire."

Official motto of the U.S. state of New Hampshire

DEDICATION

Dedicated to my parents - Yueming Zhou and Tao Li

ACKNOWLEDGEMENTS

I would like to express my gratitude to many people without whom I would not have been able to complete my doctoral study and to have written this dissertation. First and foremost, I would like to give my deepest appreciation to my advisor Dr. Joseph Klewicki for his continuous and patient support for my PhD study, research and life. His encouragement and guidance helped me in all the time of research and writing of this dissertation. Working with him on such interesting projects is one of the best choices I have made for the past few years.

Besides my advisor, I would like to thank my colleagues, Dr. Caleb Morrill-Winter, Dr. Faraz Mehdi and Mr. Paschal Vincenti for their help in experimental instrumentations, measurements and valuable advice; and I would also like to thank my collaborator, Dr. Sergio Pirozzoli in University of Rome "La Sapienza" for his DNS data and the researchers cited in my dissertation who made their DNS data publicly available. I acknowledge my committee members, Dr. Gregory Chini, Dr. John McHugh, Dr. Christopher White, Dr. Martin Wosnik and Dr. John Gibson for their helpful comments and suggestions on my dissertation, and I also acknowledge Dr. Marianna Shubov for her arrangement of one of my PhD qualifying exams. The assistance from the administrators Tracey Harvey and Lauren Foxall are also gratefully acknowledged.

Most importantly, I would like to thank my family: my mother Tao Li and my father Yueming Zhou. Without their support, quiet patience, encouragement and unwavering love, I would be lost. Finally, financial support from the National Science Foundation (Project No. NSF-1437851), the Australian Research Council (Grant No. DP150102593) and CEPS Fellowship for my research is greatly appreciated.

TABLE OF CONTENTS

LIST OF FIGURES

LIST OF TABLES

ABBREVIATIONS

VF: Viscous Force

TI: Turbulent Inertia

MI: Mean Inertia

PG: Mean Pressure Gradient

MVD: Mean Viscous Diffusion

WRS: Rate of Work by Net Reynolds Stress

MD: Mean Dissipation

MPD: Mean Pressure diffusion

MA: Mean Advection

TVD: Turbulent Viscous Diffusion

PTD: Production/turbulent Diffusion

TD: Turbulent Dissipation

TPD: Turbulent Pressure Diffusion

TAPD: Turbulent Advection/Pressure Diffusion

VD: Viscous Diffusion

PT: Production/Turbulent Diffusion

D: Dissipation

PD: Total Pressure Diffusion

APD: Advection/Turbulent Pressure Diffusion

MD: Molecular Diffusion

GT: Gradient of Turbulent Flux

HG: Heat Generation

MMD: Mean Molecular Diffusion

PGT: Product Gradient of Turbulent Transport Flux

PG: Product Heat Generation

TD: Turbulent Diffusion

TMT: Turbulent Molecular Transport

GP: Gradient Production TD: turbulent Dissipation

MT: Molecular Transport

GPTD: Gradient Production/Turbulent Diffusion

SYMBOLS

$UppercaseLetters$	Average Quantities
$LowercaseLetters$	Fluctuating Quantities
x	Streamwise Direction
y	Wall-normal Direction
z	Spanwise Direction
U	Streamwise Mean Velocity
V	Wall-normal Mean velocity
W	Spanwise Mean Velocity
u	Streamwise Fluctuating Velocity
v	Wall-normal Fluctuating velocity
w	Spanwise Fluctuating Velocity
Θ	Mean Temperature
θ	Fluctuating Temperature
δ	Half Channel Height or Boundary Layer Thickness
ν	Kinematic Viscosity
μ	Dynamic Viscosity
k	Thermal Conductivity
ρ	Density
C_p	Specific Heat at Constant Pressure
$\alpha = k/(\rho C_p)$	Thermal Diffusivity
$u_\tau = \sqrt{\tau_w/\rho}$	Friction Velocity

Re_τ or $\delta^+ = \delta u_\tau / \nu$	Friction Reynolds Number
$Pr = \nu / \alpha$	Prandtl Number
$+$	Inner-normalization

ABSTRACT

SELF-SIMILAR PROPERTIES AND LEADING BALANCE SCALING STRUCTURE OF WALL-BOUNDED TURBULENT FLOWS

by

Ang Zhou

University of New Hampshire, December, 2017

Wall-bounded turbulent flows are ubiquitous in numerous technological applications, and thus much effort has been devoted to investigate their properties. Scaling analyses involving the application multiple-scale approaches are effectively used to explore parameters (Reynolds, Prandtl numbers) dependent scaling behaviors of these flows. The objective of this dissertation research is to firstly extend the analysis of self-similar behaviors on the inertial domain as admitted by the mean dynamics in wall-bounded turbulent flows (WBTF). It then mathematically and physically characterizes the existence of a leading order balance structure in both the kinetic energy and passive scalar transport budgets, and subsequently uses this leading balance structure for scaling purposes.

Recent evidence indicates that, at sufficiently high Reynolds number, a number of the statistical measures of wall-turbulence exhibit self-similar behaviors on an interior inertial domain. Experimental measurements in the Flow Physics Facility at the University of New Hampshire have been acquired, and well-resolved streamwise velocity measurements up to high Reynolds number are used to investigate three measures of self-similarity in turbulent boundary layers, and compare their behaviors with those revealed through analysis of the mean momentum equation. The measures include the Kullback-Leibler divergence (KLD), the logarithmic decrease of even statistical moments, and the so-called diagnostic plot. The findings indicate that the approximately constant KLD profiles and the approximately logarithmic moment profiles follow the same scaling but reside interior

to the bounds of the self-similar inertial domain associated with the mean dynamics. Conversely, the bounds of the self-similar region on the diagnostic plot correspond closely to the theoretically estimated bounds.

Multiple-scale analysis involving the consideration of the relative magnitude of terms in the governing equation is applied to kinetic energy budgets for fully developed turbulent flow in pipes and channels, and in the zero-pressure gradient turbulent boundary layer. These analyses are based on available high-quality numerical simulation data. The mean kinetic energy budget is analytically verified to exhibit the same four-layer structure as the mean momentum equation, while the turbulence budget only shows either a two- or three-layer structure depending on channel/pipe versus boundary layer flow. A distinct four-layer structure is observed in position and size for the total kinetic energy budget. Here the width of the third layer, which is located in the inertia domain of the mean dynamics, is mathematically reasoned to scale with $\delta^+ - \sqrt{\delta^+}$ at finite Reynolds number.

Like the velocity field, the passive scalar field equation in WBTF can also be quantified in terms of its leading balance structure. Both the mean scalar and scalar variance equations with constant heat generation for fully-developed turbulent channel are explored. A similar four-layer structure is found using the same methodology. Both the Reynolds number and Prandtl number dependent scaling of the layer thickness is empirically quantified with available DNS data and verified through rigorous scaling analysis. The analysis also indicates that the mean scalar equation can be cast into an invariant form that properly reflects the local dominant physical mechanism, which uncovers the governing effect of a small and constant parameter on an underlying scaling layer hierarchy. There exists a linear region in the distribution of the inner-normalized widths of this layer hierarchy. Like the momentum equation, analysis indicates that this region coincides with where the mean scalar profile exhibits a logarithmic increase and leads to a distinct expression for the scalar log law. The scalar variance equation manifests itself like the total kinetic energy budget with a distinctive four-layer structure, in which the third layer size has a special scaling under the effects of both Reynolds number and

Prandtl Number. The underlying causes of the difference between the Kármán constant and the scalar Kármán constant, i.e., $k_\theta > k$, are also investigated and clarified.

CHAPTER 1

INTRODUCTION

1.1 Background

Fluid flows (e.g., of air or water) are ubiquitous in nature. Generally, there are two basic flow types, laminar flow and turbulent flow. Laminar flow is characterized by smooth variations in parallel layers. For example, in a fully-developed laminar pipe flow, the fluid particles move in straight lines that are parallel to the walls. In this type of flow, the cross-stream transport of mass, momentum, and energy is attributed to viscous (molecular) diffusion. In contrast, turbulent flow is both spatially disorganized and unsteady. Seemingly chaotic motion is characteristic of all turbulent flows, and the high rates of mixing of mass, momentum, and energy are related to the enhanced diffusivity of the flow caused by the stirring motion of the turbulent eddies.

Wall turbulence is important to industry and human life applications. For industrial applications, such as in oil pipelines, these flows require additional energy, relative to laminar flow, to overcome the increased drag due to turbulence. The lowest portion

of atmosphere, the troposphere, is vital to us where we breathe and live. Within the troposphere, closest to the ground and sea level lies the atmospheric boundary layer, which is about 1 km thick. It forms the layer where the atmosphere "feels" the contact with the ground surface. The friction exerted by the wind against the ground surface causes the wind to be sheared and creates turbulence. Process such as pollutant transport and the advection of plant spores are largely dictated by the turbulence in the atmospheric boundary layer.

Generally, wall-turbulence is characterized by a spatially complex vorticity field, which advects itself in a chaotic manner. In iso-themral flow, the vorticity is generated at a solid surface, owing to the pressure variation in the streamwise and spanwise directions. In the classical picture the vortices/eddies of the largest integral scale obtain energy from the mean flow. And this energy is passed down by eddies of Taylor microscale through the energy cascade to the smallest eddies of Kolmogorov scale, where the kinetic energy is dissipated into heat. Wall-bounded turbulent flows (fully-developed channel and pipe flows and flat plate boundary layer) at high Reynolds number have become an increasingly active area of research over the past several decades (Smits et al., 2011a; Marusic et al., 2010; Klewicki, 2010). In this dissertation, I investigate the scaling behaviors of these flows as function of Reynolds number. This accomplishes through the multiple-scale analysis of the relevant mean equations. These analyses, however, are distinct from the traditional approach.

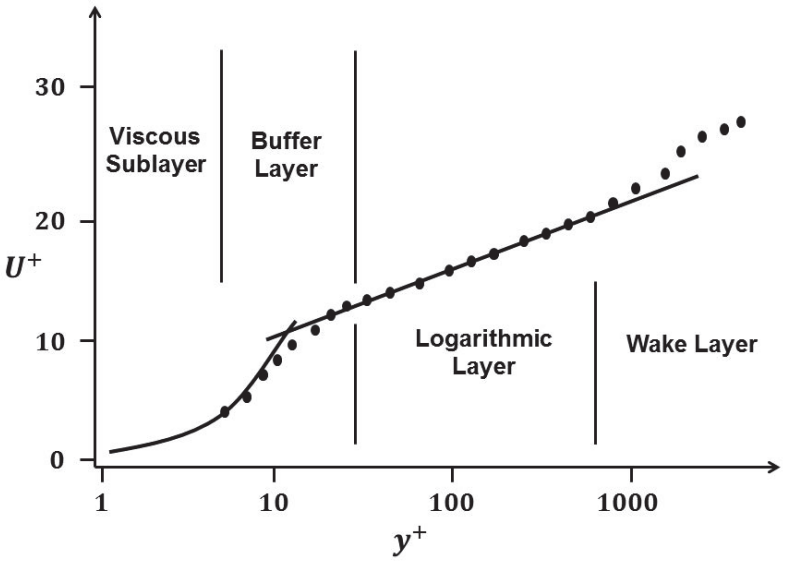

FIGURE 1.1: Sketch of the inner-normalized mean velocity profile.

1.1.1 Traditional Wall-Flow Description

The traditional description of turbulent wall-flow structure has direct connection to the properties of the mean velocity profile (Tennekes and Lumley, 1972). A schematic of this well-used structure is shown in Fig. 1.1. U is the streamwise mean velocity and y is the wall-normal distance. This profile is typically made non-dimensional using inner variables, u_τ and ν, where $u_\tau = \sqrt{\tau_w/\rho}$ is the friction velocity, τ_w is the mean wall shear stress and ν is the kinematic viscosity. The '+' denotes the inner-normalization. With this description, the viscous sublayer flow, $0 \lesssim y^+ \lesssim 5$, is dominated by the effects of viscosity and characterized by a linear mean velocity profile. In the buffer layer, $5 \lesssim y^+ \lesssim 30$, the viscous and Reynolds stresses are both dynamically significant, and the profile transitions from linear to approximately logarithmic. Under the mean profile description, these two layers are associated with the direct effects of viscosity, and their thickness remains a fixed

number of viscous lengths, independent of Reynolds number. Consistently, the velocity increments across these layers are a fixed number in inner units. In the third classical layer, the mean velocity has a logarithmic variation from near $y^+ \simeq constant$ to $y/\delta \simeq 0.2$. The dynamics here are seen to be dominated by the inertial effects of the turbulence. In the wake layer, $0.2 \lesssim y/\delta \lesssim 1$, mean inertia (or mean pressure gradient) and turbulent inertia comprise the predominant dynamical mechanisms. The logarithmic and wake layers grow at a rate proportional to δ with their velocity increments approaching a fixed fraction of U_∞ as $\delta^+ \to \infty$ (Pope, 2000; Davidson, 2015).

Wosnik et al. (2000) proposed a layer structure for turbulent channel and pipe flows. Near the wall ($y^+ \lesssim 0.1\delta^+$), there exist two separate regions: the viscous sublayer and the overlap region. Each of these two regions has its two subregions. The linear sublayer closest to the wall ($y^+ \lesssim 3$) where the viscous stress dominates and the buffer layer ($3 \lesssim y^+ \lesssim 30$) where both the Reynolds stress and viscous stress are dynamically relevant constitute the viscous sublayer. Above the near wall viscous sublayer, the overlap region is composed of a mesolayer ($30 \lesssim y^+ \lesssim 300$) where the viscous stress is negligible but acts on the turbulence scale and produce the Reynolds stress, and an inertial sublayer ($300 \lesssim y^+ \lesssim 0.1\delta^+$) which is dominated by the inertia.

1.1.2 Four-Layer Structure of Mean Momentum Balance and Its Implications for Scaling

Over the past decades, an increasing number of studies have been focusing on an increasing use of the Reynolds-averaged Navier-Stokes (RANS) equations to predict scaling behaviors (Marusic et al., 2010; Klewicki, 2010). These include the use of the mean momentum equation to reveal the scaling properties of WBTF (Klewicki, 2010; Fife et al., 2005b). The mean dynamical structure of these flows is quite distinct from laminar flow. The dynamics of laminar wall-bounded flows is everywhere a balance between a driving pressure force or inertia and a retarding viscous force. Instability occurs with increasing Reynolds number and the turbulent inertia comes into being, and it represents the non-linear interaction mechanism in the mean dynamics. This marks the appearance of the transitional regime (Elsnab et al., 2011; Klewicki et al., 2011, 2012), and eventually the onset of four-layer regime when the Reynolds number becomes large enough, i.e., $\delta^+ \gtrsim 180$ for channel/pipe flow or $\delta^+ \gtrsim 370$ for boundary layer flow (Elsnab et al., 2011; Klewicki et al., 2011; Klewicki, 2013b). In contrast to the traditional layer structure described above, direct analysis of the mean momentum equation reveals a different four-layer structure for Reynolds numbers above the transitional regime. The relative magnitude of the terms in the mean momentum equation are used to reveal this four-layer structure. The inner-normalized mean momentum equations for statistically stationary, fully developed, incompressible turbulent channel/pipe flow and zero-pressure gradient

turbulent boundary layer flow are

$$\frac{d^2U^+}{dy^{+2}} + \frac{dT^+}{dy^+} + \frac{1}{\delta^+} = 0 \tag{1.1}$$

and

$$\frac{\partial^2U^+}{\partial y^{+2}} + \frac{\partial T^+}{\partial y^+} + \left(-U^+\frac{\partial U^+}{\partial x^+} - V^+\frac{\partial U^+}{\partial y^+}\right) = 0 \tag{1.2}$$

respectively. Here, x denotes the streamwise direction, with the wall-normal direction given by y. The x and y velocity components are given by variants of u and v respectively, and the upper case letter denotes the averaged quantities. $T^+ = -\langle uv \rangle^+$ is referred to as the Reynolds stress. The first two terms are common in (1.1) and (1.2), and these represent the viscous force (VF) term and turbulent inertia (TI) term. The third term is mean pressure gradient (PG) term for the channel/pipe, and mean inertia (MI) term for the boundary layer. By taking the ratio of VF/TI, one can reveal the leading balance in (1.1) and (1.2) with wall-normal distance. A sketch of the resulting layer structure is presented in Fig. 1.2. Close to the wall, layer I is reflected by the nominal balance between the viscous stress gradient and the mean pressure gradient in the channel/pipe or mean advection in the boundary layer. The next adjacent layer, layer II, exists where the viscous stress gradient and the Reynolds stress gradient constitute the leading order balance. Across layer III, the Reynolds stress attains its maximum value, and the zero-crossing of the Reynolds stress gradient is associated with a balance breaking and exchange of dominant terms. All the three terms in the relevant mean momentum equation are of the equal order in layer III. The fourth layer represents a balance between the Reynolds stress

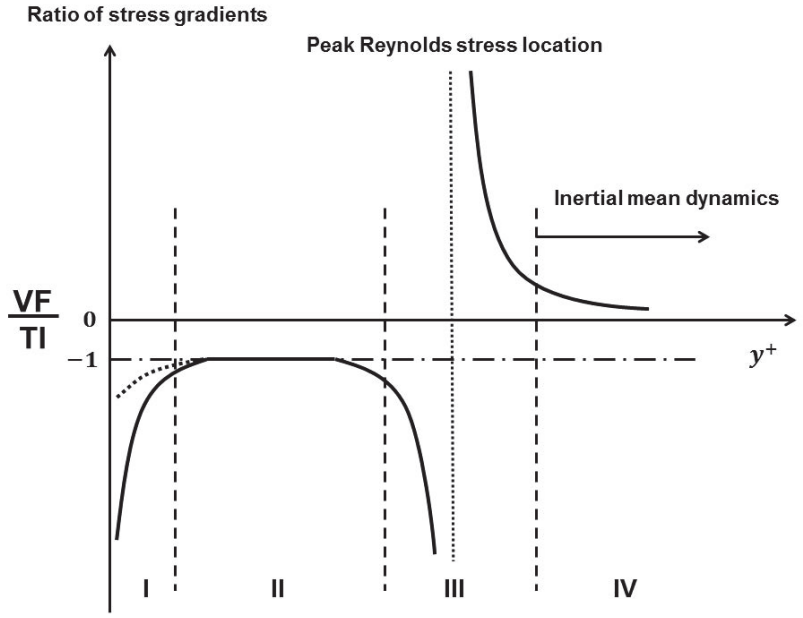

FIGURE 1.2: Sketch of the ratio of the viscous stress gradient to the Reynolds stress gradient in boundary layer, pipe, and channel flows at any given Reynolds number. The dotted line in layer I is for a boundary layer, and the solid line is for a pipe or channel.

TABLE 1.1: Scaling behaviors of the layer thicknesses and velocity increments of the four-layer structure of the mean momentum balance. (Note that the values in the parentheses are asymptotically attained as $\delta^+ \to \infty$.)

Physical layer	Δy increment	ΔU increment
I	$O(\nu/u_\tau)\,(\simeq 3)$	$O(u_\tau)\,(\simeq 3)$
II	$O\left(\sqrt{\nu\delta/u_\tau}\right)\,(\simeq 1.6)$	$O(U_\infty)\,(\simeq 0.5)$
III	$O\left(\sqrt{\nu\delta/u_\tau}\right)\,(\simeq 1.0)$	$O(u_\tau)\,(\simeq 1)$
IV	$O(\delta)\,(\to 1)$	$O(U_\infty)\,(\to 0.5)$

gradient and the mean pressure gradient or mean advection due the loss of the leading order viscous stress. Quantitatively, the layer thicknesses and the velocity increments across these layers have been shown both empirically and analytically to exhibit distinct Reynolds number dependencies. Table 1.1 shows these scaling behaviors. As expected, layer I and layer IV respectively comply with inner and outer scaling. However, an intermediate length scale, i.e., $\sqrt{\nu\delta/u_\tau}$, is empirically observed and analytically shown to

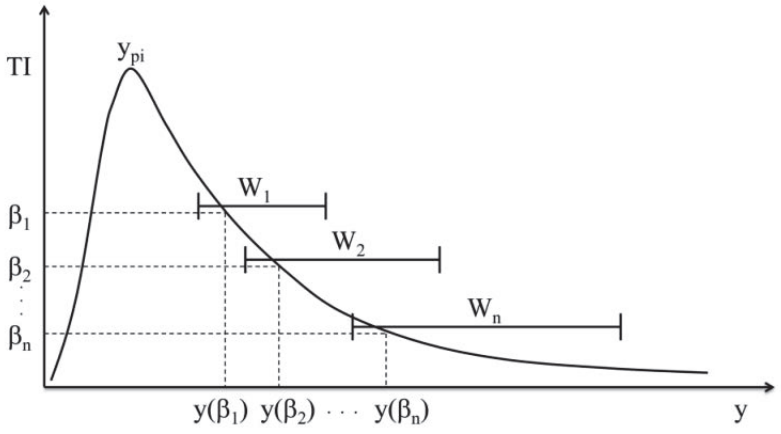

FIGURE 1.3: Schematic depiction of the scaling layer hierarchy described by continuous distribution of widths. Figure is from Klewicki et al. (2014).

characterize the other two layers, with their thicknesses respectively given by $3 \lesssim y^+_{II} \lesssim 1.6\sqrt{\delta^+}$ and $1.6\sqrt{\delta^+} \lesssim y^+_{III} \lesssim 2.6\sqrt{\delta^+}$. The velocity increment across layer II remains about one half of U_∞, independent of δ^+, while there is only about a $1.0u_\tau$ increment across layer III. With increasing Reynolds number, all the scaling properties of the four-layer regime become increasingly well established (Wei et al., 2005a).

1.1.3 L_β Hierarchy of Scaling Layer

A complementary structure of the mean equations that will be revisited in significant detail herein is that the mean momentum equation admits an invariant form on each layer of a hierarchy of scaling layers. (Fife et al., 2005b; Wei et al., 2005b; Fife et al., 2005a; Klewicki, 2013b; Klewicki et al., 2014). A sketch of this hierarchy is depicted in Fig. 1.3. This hierarchy resides between the inner and outer peak positions of the turbulent inertia term, and is physically associated with the changing (increasing) size of the momentum transporting motions with distance from the wall.

The mathematical construction of this layer hierarchy begins by applying a transformation to $T^+ = -\langle uv \rangle^+$

$$T_\beta^+ = T^+ + \frac{y^+}{\delta^+} - \beta y^+, \tag{1.3}$$

On each hierarchy layer, the parameter β has a small positive and constant value, and, as depicted in Fig. 1.3, β is related to the value of the TI term and a specific y^+. With the transformation 1.3, the mean momentum equation for turbulent channel/pipe flow becomes

$$\frac{d^2U^+}{dy^{+2}} + \frac{dT_\beta^+}{dy^+} + \beta = 0. \tag{1.4}$$

Across each scaling layer, the local mean dynamics undergoes a balance breaking and exchange of terms analogous to what occurs across layer III. For each value of β, the T_β^+ attains its maximum value $T_{\beta m}^+$ at a position $y_{\beta m}^+$. Thus on each layer, all three terms in Eq. (1.4) are of the same order of magnitude. This motives the need to rescale the Eq. (1.4) in such a way that each term is $O(1)$ independent of β for all δ^+. In the simplest manifestation, rescalings can be shown to occur according to

$$y^+ = y_{\beta m}^+ \beta^{-1/2} \hat{y}, \quad T_\beta^+ = T_{\beta m}^+ + \beta^{1/2} \hat{T}. \tag{1.5}$$

Application of these rescalings leads to an invariant form of (1.4)

$$\frac{d^2U^+}{d\hat{y}^{+2}} + \frac{d\hat{T}}{d\hat{y}} + 1 = 0 \tag{1.6}$$

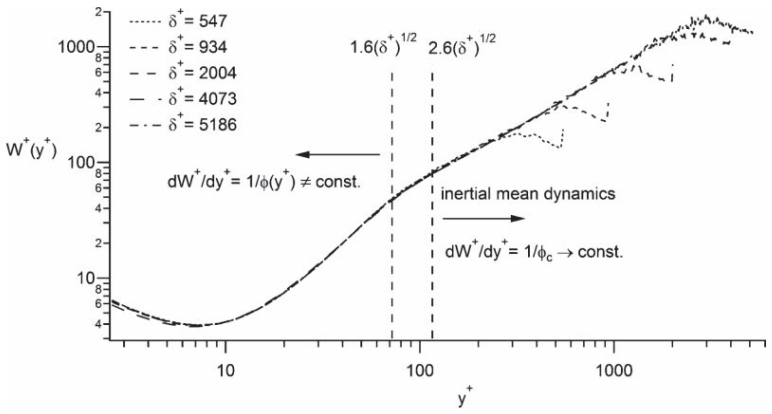

FIGURE 1.4: Distribution of W^+ for channel flows. Figure is from Klewicki and Oberlack (2015).

that is operative on every layer of the L_β hierarchy (Klewicki, 2013b; Klewicki et al., 2014).

There is a function, $W^+(y^+)$, quantifying the inner-normalized width of the layers on hierarchy. Without loss of generality, W^+ can be shown to equal $\beta^{-1/2} = (-d^2U^+/dy^{+2})^{-1/2}$. Distributions of $W^+(y^+)$ are shown in Fig. 1.4. W^+ is physically recognized as the averaged size of the motions that are responsible for the net wallward flux of momentum from layer to layer. It also quantifies the average size of motions responsible for the generation of $T^+ = -\langle uv \rangle^+$. On the inertial portion of the hierarchy, i.e., $y^+ \gtrsim 2.6\sqrt{\delta^+}$ (See Table 1.1), the W^+ profile is well-approximated by a linear function with the accuracy of this linear approximation increasing with increasing δ^+. Subsequent analysis reveals that the quantity

$$\frac{1}{\phi} = \frac{A}{2} = -\frac{1}{2}\frac{d^2\hat{T}}{d\hat{y}^2} = -\frac{1}{2}\frac{d^2T^+}{dy^{+2}}\beta^{-\frac{3}{2}} = -\frac{1}{2}\frac{d^2T^+}{dy^{+2}}\left(-\frac{d^2U^+}{dy^{+2}}\right)^{-\frac{3}{2}} \tag{1.7}$$

is $O(1)$ and approaches a constant over the inertial domain as $\delta^+ \to \infty$, i.e., $\phi \to \phi_c$

as $\delta^+ \to \infty$ (Fife et al., 2009; Klewicki et al., 2009; Klewicki, 2013b). The coordinate stretching function, ϕ, is exactly given by

$$\phi = \frac{dW^+}{dy^+}, \tag{1.8}$$

and this function becomes constant on the inertial domain (See Fig. 1.4). Physically, ϕ is the stretching of the y coordinate required to produce an invariant representation of the flux of turbulent force as generated by the momentum transport of W sized eddies (Klewicki et al., 2014). The invariance properties of ϕ just described provide a basis for constructing a similarity solution on the inertial domain where ϕ_c is a constant. A similarity solution to the mean velocity U^+ is analytically found to be

$$U^+ = \phi_c^2 ln\left(y^+ - y_0^+\right) + By^+ + C. \tag{1.9}$$

Eq. (1.9) is found by directly integrating the mean momentum equation (Klewicki and Oberlack, 2015). As is apparent by comparing with the traditional log law, the Von Kármán constant is given by $k = \phi_c^{-2}$. The coefficient B is tends to be 0 as $\delta^+ \to \infty$, since $dU^+/dy^+ \to 0$ as $y^+ \to \infty$. With (1.9), T^+ can be exactly determined from Eq. (1.1). The theory and data analysis provides the evidence that the coefficient on the linear term, i.e., B, should decay to zero as $\delta^+ \to \infty$, since $dU^+/dy^+ \to 0$ as $y^+ \to \infty$. And that k should asymptotically attain constant value, i.e., $k \to (3 - \sqrt{5})/2$ at sufficiently high δ^+ (Klewicki and Oberlack, 2015). The region between $2.6\sqrt{\delta^+}$ and 0.5δ is where the mean momentum equation admits the self-similar behavior associated with $\phi = \phi_c = constant$

on the inertial domain.

A similar approach has recently been applied to the mean momentum equation for zero pressure gradient turbulent boundary layer flow (Morrill-Winter et al., 2017). This analysis is complicated by the fact that, unlike the pressure gradient in the channel/pipe, the mean inertia term in Eq. (1.2)is not constant. The mean inertia term, i.e., $\bar{A}^+ = -[U^+(\partial U^+/\partial x^+) + V^+(\partial U^+/\partial y^+)]$, can, however, be written as $\alpha \bar{A}_p^+$, where $0 \leqslant \alpha \leqslant 1$ and $\hat{A}_p^+$ is the peak magnitude of $\hat{A}^+$. An apparent integral property of α is that its average value,

$$\bar{\alpha} = \frac{1}{\delta^+} \int_0^{\delta^+} \alpha dy^+, \tag{1.10}$$

is empirically found to be a constant, $\bar{\alpha} = 0.57$, over a large δ^+ range (Morrill-Winter et al., 2017). With this α can be normalized by $\hat{\alpha}$ such that $\underline{\alpha} = \alpha/\bar{\alpha}$. Lastly, to obtain a similar balance between constant terms in the outer region, the Reynolds stress, T^+, is transformed using

$$\tilde{T} = T^+ + \frac{1}{\delta^+} \int_0^{y^+} \Lambda\left(y^+, \delta^+\right) dy^+, \tag{1.11}$$

where $\Lambda(y^+, \delta^+) = \underline{\alpha} - \underline{\alpha}_m$, $\underline{\alpha}_m$ is evaluated at y_m^+, and y_m^+ is where the the turbulent inertia term crosses zero from above. With these definitions, (1.2) becomes

$$\frac{\partial^2 U^+}{\partial y^{+2}} + \frac{\partial \tilde{T}}{\partial y^+} + \frac{\underline{\alpha}_m}{\delta^+} = 0, \tag{1.12}$$

which shows that the boundary layer equation admits the same self-similarity as the channel/pipe.

1.2 Dissertation outline

To data, the relative magnitudes of the terms in the mean momentum equation has been shown to determine an underlying a self-similar structure that exists on a inertial domain quantified by considering the leading balances of the mean dynamics equation. Based on these previous studies, Chapter 2 herein provides the description of three recently developed measures, i.e., the Kullback-Leibler divergence (KLD) (Tsuji et al., 2005), the logarithmic decrease of even statistical moments (Meneveau and Marusic, 2013) and the diagnostic plot (Alfredsson and Örlü, 2010), to quantify properties of the inertial domain. New data are computed based on the high Reynolds number turbulent boundary layer streamwise velocity measurements using hot-wire anemometry. Comparisons are made between the domain where these measures provide evidence of self-similarity and the domain where the mean momentum equation exhibits inertially dominated self-similar behavior.

Chapter 3 provides a detailed description of the leading balance in kinetic energy balance theory wall-bounded turbulent flows. A similar approach to previous study of the mean momentum balance is used to explore the mean, turbulence, and total kinetic energy balances in planar channels, circular pipes, and flat plate boundary layer flows. The analytical treatment of the total kinetic budget is, however, more challenging than the mean momentum equation, since there are more physical terms in the equation. The Reynolds number dependent scaling behavior of the layer thicknesses are empirically quantified using available numerical simulation data, and analytically reasoned using

multiple-scale analysis. This analysis reveals a four-layer structure that is distinct from that of the mean momentum balance.

Chapter 4 documents a study of the passive scalar transport equations involving both the mean scalar and scalar variance for fully-developed turbulent channel flow. Unlike previous studies of channel flow with constant surface heat flux, this flow has a uniform heat generation. This configuration has distinct analytical advantages relative to precisely elucidating the underlying self-similar structure admitted by the mean transport equation. The leading balances of terms in the mean equation are empirically determined and analytically described, while those in the variance equation is quantified based on available simulation data. As expected, the scalar field shows a similar structure to the velocity field, but it has a dependence on both the Reynolds number and Prandtl number.

The dissertation concludes with Chapter 5, which summaries the key findings from the previous chapters. Here the present work is only able to present a small quantity of results that support the theory of wall-bounded turbulent flows. With these facts in mind, more analytical, experimental and computational results are needed to make the wall-turbulence problem more analytically tractable.

CHAPTER 2

THREE MEASURES OF SELF-SIMILARITY AND THEIR CONNECTIONS TO SELF-SIMILAR MEAN DYNAMICS IN INERTIAL SUBLAYER OF TURBULENT BOUNDARY LAYER

2.1 Background

The concept of an inertial sublayer is common to many empirical, phenomenological and (semi) analytical approaches to describing the statistical structure of the turbulent boundary layer. In the classical spectral representations of turbulence (not necessarily wall-turbulence) the inertial sublayer is seen to exist in a spectral range where the wavelengths are large relative to those associated with the dissipative motions, and simultaneously small relative to the integral scales of motion that are directly influenced by the external boundary conditions (Kolmogorov, 1941). Analogously, the inertial layer of wall-turbulence is seen to exist over an interior spatial domain that is sufficiently far from from the wall, and simultaneously sufficeintly small relative to the overall width of the

flow, e.g., Tennekes and Lumley (1972). The present study explores this spatial inertial sublayer and its connections to the self-similarities formally admitted by the mean momentum equation. The broader aim is to advance a more unified theoretical framework for describing turbulent boundary layer scaling and structure. To generate an appropriate context, it is useful to recognize that there have traditionally been two predominant, and in some respects complementary, descriptions of the flow structure within the spatial inertial sublayer of the turbulent boundary layer.

2.1.1 Attached-Eddy Description and Logarithmic Mean Profile

As originally postulated by Izakson (1937) and Millikan (1938), one of these descriptions assumes the existence of an overlap layer where respective functions of inner and outer normalized distance from the wall are simultaneously valid. Here inner normalized variables are rendered dimensionless using the kinematic viscosity, ν, and the friction velocity, $u_\tau = \sqrt{\tau_w/\rho}$ (where τ_w is the mean wall shear stress and ρ is the mass density), and outer normalizations use u_τ and the boundary layer thickness, δ. For the mean velocity profile, this set of assumptions promotes the further hypothesis that the gradients of the inner and outer functions match across the overlap layer. The leading order term in the proposed expansions describing this overlap leads directly to the familiar form of the logarithmic mean velocity profile,

$$\frac{U}{u_\tau} = \frac{1}{k} ln \left(\frac{y u_\tau}{\nu} \right) + B, \tag{2.1}$$

where where k is the von Kármán constant, and B is a constant that depends on the boundary conditions. Borrowing heavily from the mathematical machinery of matched asymptotic expansions, the notion that the inertial sublayer is where inner and outer functions can be simultaneously matched has been used in similar formulations that seek to describe the profiles of a number of other wall-flow statistics, e.g., Panton (2005).

The second description follows from the arguably less prescriptive hypothesis that across the inertial sublayer the only dynamically relevant length scale is proportional to the distance from the wall itself. Relative to the mean velocity gradient, the simplest rendering of this hypothesis follows from dimensional analysis and is encapsulated in the statement,

$$\frac{\partial U}{\partial y} = \frac{u_\tau}{ky}, \tag{2.2}$$

where U is the streamwise (x component) mean velocity, y is the coordinate normal to the wall, and the equality holds owing to the appropriate specification of the von Kármán constant, k. In effect, Eq. (2.2) is the basis for Prandtls construction of the logarithmic mean velocity profile (Prandtl, 1925). Perhaps more profoundly, following Townsend (1961) a number of researchers (Perry and Chong, 1982; Perry and Marusic, 1995) have demonstrated that this situation is physically consistent with the existence of a self-similar internal hierarchy of motions, the attached eddy hierarchy, that, in a statistical sense, is comprised of motions of characteristic wall-normal sizes that are proportional to the distance from the wall. (It is in this sense that they are attached to the wall.)

Owing to this, the attached eddy phenomenology is inherently consistent with the existence of a logarithmic mean velocity profile, and, as discussed further below, also leads to the expectation that the streamwise velocity variance, $\langle u^2 \rangle$, exhibits a logarithmic decrease across the spatial inertial sublayer. (Note that angle brackets denote the time average.) The attached eddy paradigm is additionally attractive relative to observations of instantaneous and conditional flow structure, as numerous observations over the past three decades have revealed evidence of a hierarchical eddy structure in boundary layers; perhaps most notably in the form of packets of hairpin-like vortices (Adrian et al., 2000; Adrian, 2007), or self-similar vortex clusters (Del Álamo et al., 2006).

As is apparent, both the overlap and attached eddy (distance from the wall scaling) based descriptions apply to an interior inertial domain of the flow. Neither of these approaches, however, provide particularly specific insight into how or why the flow properties behave the way they do on this domain, or provide guidance regarding the bounds of this inertial domain. Similarly, while both have a general descriptive capability, neither explicate the underlying dynamics. The fundamental reason for this is that both the overlap layer framework and the attached eddy phenomenology rely upon additional hypotheses and assumptions. These assumptions and hypotheses have, at best, limited basis in the underlying equations of motion, and this lack of a firm theoretical foundation presents challenges toward better predicting or controlling boundary layer dynamics.

2.1.2 Primary Aims

The results of the analyses of the mean dynamical equation, described briefly below, are leveraged for the present purposes by clarifying the mechanisms underlying how and why the inertial domain of interest obtains its self-similar properties, and by revealing (predicting) specific Reynolds number dependent spatial bounds for the domain over which this self-similar behavior is expected to emerge with increasing Reynolds number. Given this, the primary aims herein are to calculate and characterize recently developed measures that quantify properties of the inertial domain, and compare the domain where these measures provide evidence of self-similarity with the domain where the mean momentum equation exhibits inertially dominated self-similar behavior.

2.2 Three Measures of Self-Similarity

In addition to the logarithmic region of the streamwise mean velocity profile itself, three other heuristically/semi-empirically derived measures of self-similarity are developed and quantified.

2.2.1 KullbackLeibler Divergence

Building upon the ideas of information and entropy first introduced by Shannon and Weaver (1949),Kullback and Leibler (1951) developed the KL divergence (KLD), or relative entropy. The KLD provides an objective measure of the degree to which two probability density functions (pdf) differ. For discrete pdfs, P and Q, the KLD is a measure of the information lost when Q is used to approximate P. The KLD is calculated by

$$D\left(P \parallel Q\right) = \sum_{s_i} P(s_i) ln(P(s_i)/Q(s_i)). \tag{2.3}$$

KLD has a non-negative value for any P and Q, and it is zero only when P is exactly equal to Q. The more the P and Q come to resemble each other, the smaller is the KLD. Thus KLD indicates quantitatively the resemblance between P and Q.

Self-similar distributions are thus characterized by an invariant KLD, when measured relative to a fixed reference pdf. The KLD was first used in a turbulence context by Tsuji and Nakamura (1999), Lindgren et al. (2004), and Tsuji et al. (2005). In Tsuji et al. (2005), for each velocity time series the experimentally determined pdfs, $P_y(s)$, are compared to a Gaussian pdf, $P_G(s)$, having the same mean and variance. A primary consideration of the analysis herein is the domain over which the KLD exhibits self-similarity. For these analyses they employed boundary layer data up to Reynolds numbers of about $\delta^+ = 5200$. Fig. 2.1 shows the representative divergence $D\left(P_y \parallel P_G\right)$ as a function of y^+ together with the mean velocity profile at $Re_\theta = 12633$, where Re_θ is the Reynolds number based on the momentum thickness θ ($Re_\theta = \frac{U_\infty}{u_\tau}\frac{\theta}{\delta}\delta^+$). There is a small

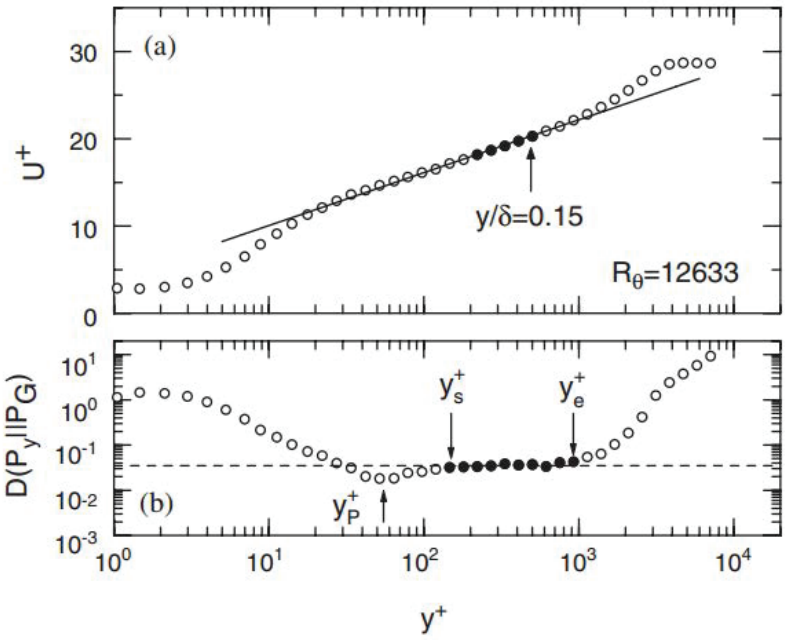

FIGURE 2.1: (a) Inner-normalized mean velocity profile. The solid line is the log-law profile, $U^+ = 1/0.38\, ln\,(y^+) + 4.1$. The end of the logarithmic region is at $y/\delta = 0.15$, which is suggested by Österlund (1999). (b) KLD. Solid circles are the constant KLD region. The starting and end points are expressed as y_s^+ and y_e^+, respectively. Figures are from Tsuji et al. (2005).

hump in mean velocity profile around $y^+ \simeq 50$. Beyond this hump, the KLD is seen to become constant. In this region, the KLD is self-similar. Tsuji et al. (2005) indicates the starting point, y_s^+, of this constant KLD region is located closer to the wall than the beginning of the logarithmic dependence of the mean velocity profile. And the ending point y_e^+ is beyond $0.15\delta^+$. In-depth study denotes the starting point, y_s^+, is evaluated to be 180 ± 15 independent of Reynolds number, when Re_θ is greater than 5000. But the ending point, y_e^+, is approximately a linear function of Reynolds number. The relation is given by the least-square fit as $y_e^+ \simeq 0.3\delta^+$.

A primary consideration of the analysis herein is the domain over which the KLD exhibits self-similarity, as compared to the location of the inertial self-similar domain

associated with the mean momentum equation.

2.2.2 Logarithmic Region for Higher-Order Even Moments

Based upon his attached eddy phenomenology, Townsend (1980) reasoned that as the Reynolds number becomes large the inner-normalized variance of the streamwise velocity fluctuations, $\langle u^2 \rangle^+$, should exhibit a logarithmic decay over nominally the same region where the mean velocity exhibits its logarithmic dependence.

Meneveau and Marusic (2013) provide substantive evidence that the reasoning logarithmic decay can be extended to the higher order even moments for the turbulent boundary layers. Their analysis results in the equation below,

$$\left\langle \left(u^+\right)^{2p} \right\rangle^{\frac{1}{p}} = B_p - A_p ln(\frac{y}{\delta}) = D_p\left(\delta^+\right) - A_p ln\left(y^+\right). \tag{2.4}$$

where $p = 1, 2, ...$,and, as with A_1, the A_p are expected to approach universal constants on the inertial domain as $\delta^+ \to \infty$. Fig. 2.2 shows the higher-order even moments for $p = 1, 2, 3, 4$ and 5 as a functions of inner-normalized distance from the wall at $Re_\tau = 19030$. The range between $y^+ > 400$ and $y/\delta < 0.3$ is used to perform the curve fits. The slope coefficients A_p for different Reynolds number are plotted in Fig. 2.3 as symbols. For $1p = 1$, A_1 appears to be independent of Reynolds number with an approximately universal value of 1.25, with an accuracy of 5%. For $p > 1$, A_p tends to values that fall below the Gaussian values.

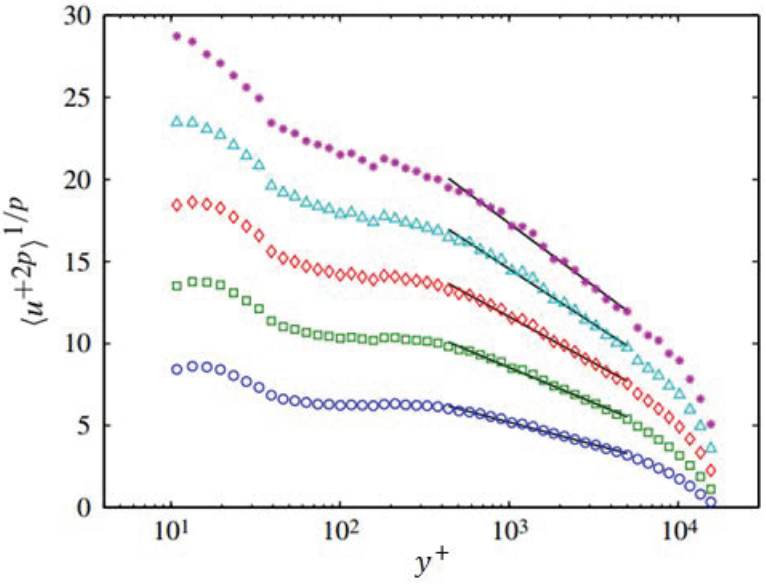

FIGURE 2.2: Higher-order even moments of order $2p = 2\,(\circ)\,, 4\,(\square)\,, 6\,(\diamond)\,, 8\,(\triangle)$ and $10\,(*)$ of streamwise velocity fluctuation as a function of inner-normalized wall distance at $Re_\tau = 19030$. The lines show the fits in the range $y^+ > 400$ and $y/\delta < 0.3$. Figure is from Meneveau and Marusic (2013).

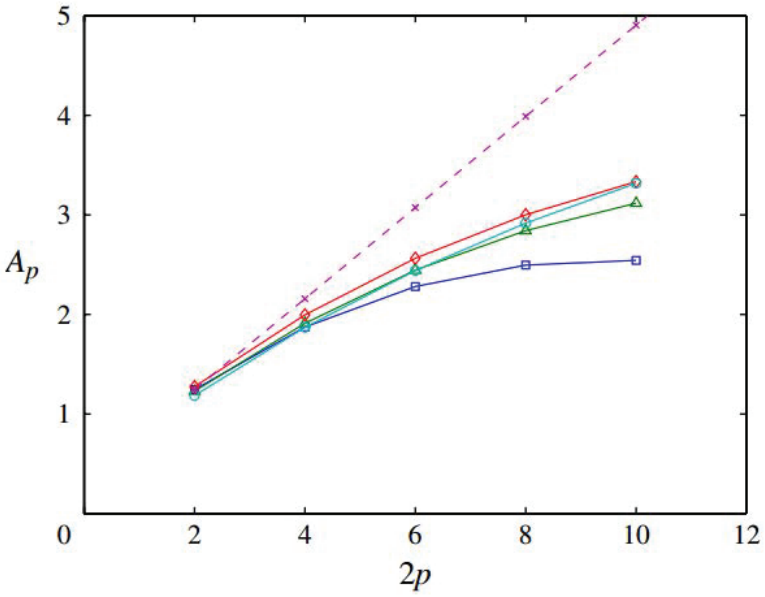

FIGURE 2.3: Logarithmic coefficients Ap as a function of order $2p$ for different Reynold numbers $Re_\tau = 2800\,(\square)\,, 3900\,(\triangle)\,, 7300\,(\diamond)$ and $19030\,(\circ)$. The crosses and dashed line show the results expected for Gaussian statistics, $A_p = A_1\,[(2p-1)!!]^{1/p}$. Figure is from Meneveau and Marusic (2013).

The analysis goal is to explore the behavior of Eq. (2.4), and especially the behavior of the logarithmic coefficients A_p over the domain where the mean momentum admits its self-similarity solution as $\delta^+ \to \infty$.

2.2.3 Diagnostic Plot

The diagnostic plot presents the streamwise velocity variance profile in a manner that only implicitly employs the distance from the wall. As first described by Alfredsson and Örlü (2010), this involves plotting, u_{rms}/U_∞ versus U/U_∞ or similarly, u_{rms}/U versus U/U_∞, where $u_{rms} = \sqrt{\langle u^2 \rangle}$ is the R.M.S. velocity, and U_∞ is the free stream velocity. Although originally developed to better understand the uncertainties associated wall turbulence measurements, this plot has subsequently been used in attempts to better understand scaling behaviors in both smooth and rough wall flows (Alfredsson et al., 2011; Castro et al., 2013).

Fig. 2.4 and Fig. 2.5 respectively show the plots of u_{rms}/U_∞ versus U/U_∞ and u_{rms}/U versus U/U_∞ from Alfredsson et al. (2011). The plot of u_{rms}/U_∞ versus U/U_∞ is shown to adhere closely to a quadratic function over the domain where $U/U_\infty \gtrsim 0.6$, which, of course, corresponds to the outer portion of the boundary layer. Similarly, the plot of u_{rms}/U versus U/U_∞ exhibits a linear variation for $U/U_\infty \gtrsim 0.6$. In essence, the diagnostic plot provides evidence of statistical self-similarity between the streamwise velocity fluctuations and the mean about which these fluctuations are measured. Herein, the research is to explore the behavior of the diagnostic plot over a reasonably large Reynolds

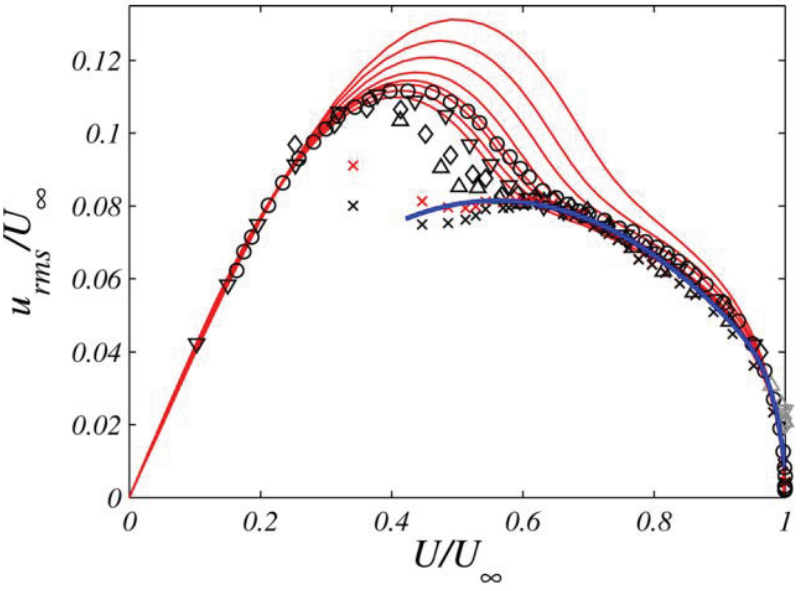

FIGURE 2.4: The diagnostic plot of u_{rms}/U_∞ versus U/U_∞. Solid lines: $Re_\tau = 250 - 1300$, DNS (Schlatter and Örlü, 2010), $\circ$: $Re_\tau = 850$, hot wire measurement (Örlü, 2009), $\triangledown$: $Re_\tau = 1700$, $\diamond$: $Re_\tau = 4200$, $\triangle$: $Re_\tau = 9500$, LDV measurements (De Graaff and Eaton (2000)), $\times$: $Re_\tau = 18000$, hot wire measurements (Fernholz et al., 1995) (light symbols indicate same data corrected for spatial resolution effects (Smits et al., 2011b). Thick dark line corresponds to the quadratic function between $U/U_\infty \gtrsim 0.6$ and $U/U_\infty \lesssim 0.9$. Figure is from Alfredsson et al. (2011).

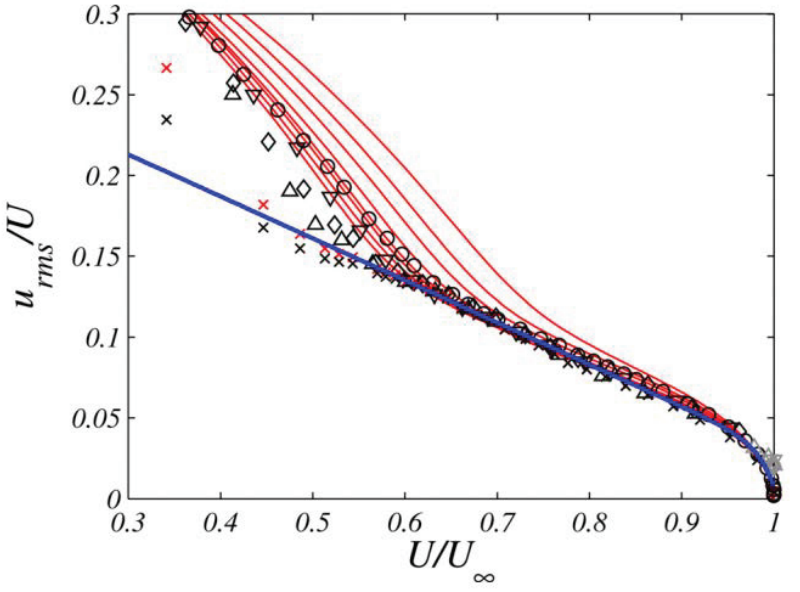

FIGURE 2.5: The diagnostic plot of u_{rms}/U versus U/U_∞. Data and symbols are the same as in Fig. 2.4. Figure is from Alfredsson et al. (2011).

number range, and, in particular, compare the domain of self-similarity indicated by this measure with that predicted via analysis of the mean dynamical equation.

2.3 Experimental Measurements

2.3.1 Flow Physics Facility

The experimental measurements were conducted in the flow physics facility (FPF) at the University of New Hampshire (UNH). The FPF is an open circuit suction tunnel that draws from, and discharges to, the atmosphere. The flow speed is driven by two $2.6m$ diameter vane-axial fans, powered by two $300KW$ AC motors. Speed control is attained by two ultra low-noise variable frequency drives that are operated in a coupled leader-follower configuration. The maximum flow speed in the FPF test section is currently about $14.5m/s$. This corresponds to a volume flow rate of about $252m^3/s$. The test section of this wind tunnel has the dimensions of $72m \times 6m \times 2.8m$. The height of this test section, $2.8m$, is approximately evaluated, since the upper wall is divergent accounting for the displacement thickness growth downstream. This large test section affords high Reynolds numbers at relative low wind speeds, and thus it retains the high spatial resolution in measurements.

Fig. 2.6 shows the an exterior view of the FPF, and Fig. 2.7 give a cut-away schematic of the FPF. Relative to Fig. 2.7, the flow is from left to right and is drawn through the test section by the pair of fans located in the low pressure plenum. The flow enters the

FIGURE 2.6: FPF wind tunnel, air flow enters the text section through the inlet at the front and discharges into the atmosphere at the rear.

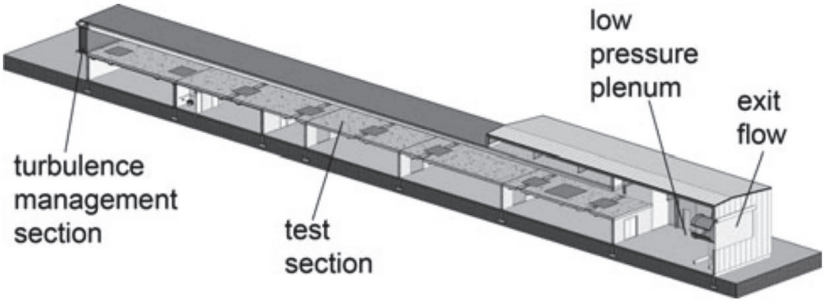

FIGURE 2.7: Cut-away schematic drawing of the FPF. Air flow is from left to right through the test section.

test section through a constant area turbulence management section, which consists of honeycomb followed by a series of five screens. The measurements were acquired in the boundary layer that develops along the lower wall of the FPF test section. The floor consists of three slabs of concrete separated by two expansion joints, at $25m$ and $50m$ downstream, respectively. The slabs are $25.4cm$ thick and were poured in place $3m$ above the ground plane using an extensive series of wooden frames. The mix of concrete was

specially formulated to yield a dense micro-structure. This promotes dimensional stability and produces an unusually flat and smooth surface. As verified by a professionally conducted survey, the deviations from flat are everywhere less than $0.26mm/m$.

The boundary layers on the lower wall and side walls of the FPF are tripped immediately downstream of the turbulence management section, the floor boundary layer in the FPF formally starts only about $1.4m$ in front of the trip. The trip consists of a $6mm$ threaded rod raised about $1mm$ above the surface, i.e., so that there is flow both above and below the trip. Previous low-speed studies found that this trip fixes the point of transition, and that the artifacts associated with the trip rapidly diminish downstream (Klewicki and Falco, 1990).

The flow quality and consistency in FPF is estimated by the streamwise free-stream turbulence intensity, u_{rms}/U_∞. The streamwise free-stream turbulence intensity generally ranges between 0.2% and 0.5%, depending on different flow speeds. The atmospheric wind conditions outside the FPF are monitored by a pair of tower-mounted 3D sonic anemometers located outside and near the inlet. Except for storm-like conditions, the effects of external gustiness are not detectable for flow speeds greater than $3m/s$. For $U_\infty \gtrsim 7m/s$, the streamwise free-stream intensity is less than 0.3%.

2.3.2 Experiments and Instrumentation

Experimental data were acquired in FPF (Vincenti et al., 2013; Zhou and Klewicki, 2015). The profile measurements were conducted using a standard single wire hotwire sensor.

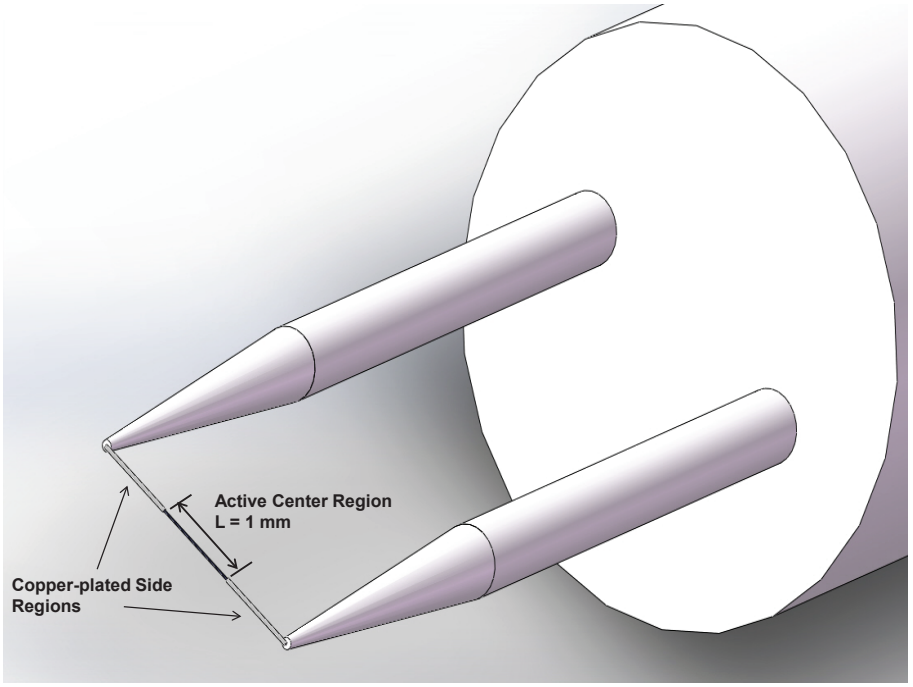

FIGURE 2.8: Hot-wire single wire probe.

The copper-plated $5\mu m$ diameter tungsten wires contained within the probe are $3mm$ in length with a $1mm$ active center region. A sketch of the probe is shown in Fig. 2.8. The copper plating allows the wires to be soft-soldered to the support prongs and serves to aerodynamically isolate the center sensing region. The probes were operated using AA Lab Systems (AN-1004) anemometers at heating ratios between 1.5 and 1.7. The frequency response of the sensor anemometer system was estimated using the impulse response module on the anemometer and always exceeded $15kHz$. This was always significantly beyond the range of turbulent frequencies in the present flows. Pre- and post-calibrations were performed in the free-stream flow. The velocities for the calibrations were derived from a Pitot-static tube connected to an MKS-Baratron 10 Torr differential pressure transducer. The barometric pressure and temperature was monitored throughout each experiment used to calculate the air density and viscosity. Temperature data were

TABLE 2.1: Turbulent boundary layer experimental data from Flow Physics Facility.

Symbol	$x(m)$	$U_\infty(m/s)$	$u_\tau(m/s)$	$\delta_{99}(m)$	$\delta^*(m)$	$\theta(m)$	δ^+	l^+	T_sU_∞/δ
◊	4	6.87	0.263	0.0861	0.0130	0.0096	1450	16.8	23940
▷	8	6.95	0.252	0.1356	0.0216	0.0154	2180	16.1	15370
◁	16	6.87	0.240	0.2456	0.0340	0.0295	3820	15.9	8390
▽	32	7.01	0.234	0.4284	0.0572	0.0437	6430	15.0	3920
∗	32	6.82	0.238	0.4274	0.0507	0.0391	6510	15.2	11490
△	66	6.95	0.226	0.7363	0.0898	0.0697	10770	14.6	2260
☆	66	6.78	0.223	0.7501	0.0890	0.0693	10750	14.3	6510
♦	4	10.43	0.397	0.0838	0.0114	0.0088	2280	25.5	3730
▶	8	10.52	0.374	0.1340	0.0185	0.0142	3270	24.4	3530
◀	16	10.63	0.351	0.2336	0.0308	0.0235	5680	24.1	3640
▼	32	10.72	0.345	0.3953	0.0482	0.0369	8970	22.7	3250
▲	64	10.21	0.327	0.7439	0.0739	0.0585	15480	20.8	2470
□	66	10.33	0.330	0.7171	0.0792	0.0632	15740	22.0	3450
○	66	13.75	0.432	0.6885	0.0722	0.0574	19670	28.6	5990

measured with a thermocouple at each x station and were collected in concert with the freestream dynamic pressure and hotwire time series. Temperature variations during any given experiment were generally $\pm 1.5^oC$. The hotwire data were sampled using a National Instruments PXI-6221 16 bit analog-to-digital converter. The sampling durations depend on the distance downstream and the free-stream velocity. The profiles were obtained using a stepper motor driven Velmex $1.4m$-high traverse fitted with a custom-built aerodynamic shroud. The probe was attached to the end of a rod that extended $0.5m$ upstream of the traverse. The friction velocity was found using the Clauser chart method employing log law constants of $k = 0.387$ and $B = 4.32$ (Marusic et al., 2013).

Table (2.1) provides a summary of the flows studied. Here x denotes the distance from the trip located at the start of the test section, δ^* is the displacement thickness, θ is the momentum deficit thickness, l^+ is the inner-normalized length of the hotwire sensor, and T_s is the sampling duration. As documented, the spatial resolution of the measurements

is very good, and at fixed speed actually improves with increasing δ^+. The polygonal symbols (including the circle) in Table (2.1) are from the study of Vincenti et al. (2013), while the star and asterisk represent additional measurements where I acquired the time series with a longer sampling duration, $12mins$ for each elevation points in the profile, to assess the effect of averaging time and reduce the convergence uncertainty. The respective maximum standard deviations from the two corresponding same velocity measurements are compared. The deviation was less than 4% of their average value. The effect of statistical convergence uncertainty did not make a significant influence on the data, and thus all the data listed in Table (2.1) were used in the analysis.

2.3.3 Experimental Results and Analyses

The measures of self-similar behavior discussed in Section (2.2) are now computed using the data sets of Table (2.1), and their properties are compared with self-similarity admitted by the mean momentum equation. When reading the data presentation section it is useful to keep in mind that the self-similar behaviors of present interest emerge as an asymptotic property of the inertial layer. Owing to this, at any finite δ^+ empirical evidences of self-similarity will necessarily be approximate. Thus, for increasing δ^+ the mean profile will become increasingly well-approximated by a logarithmic function, as will the higher order even moments of the u fluctuations. Similarly, the diagnostic plot will increasingly adhere to its linear dependence and the KLD will increasingly approximate constancy within the inertial domain. It is anticipated that the KLD will approach its asymptotic behavior most slowly with δ^+. This is because the KLD is a measure that

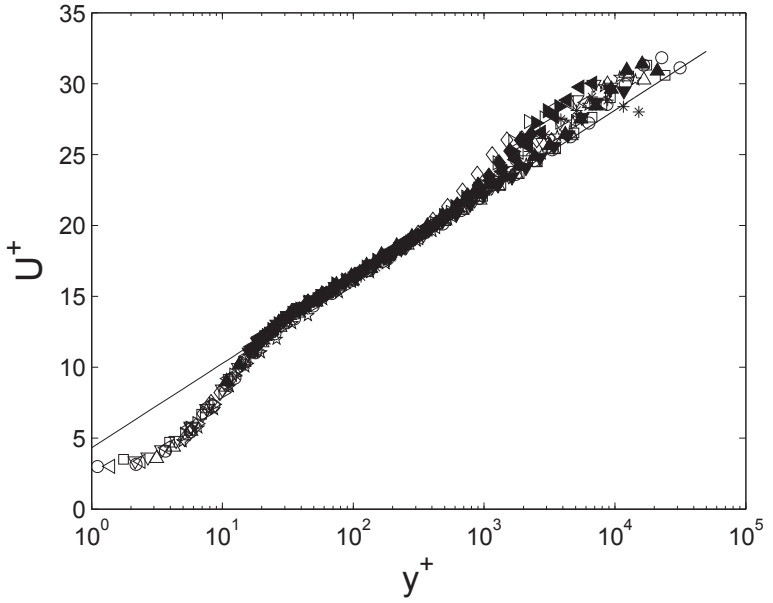

FIGURE 2.9: Inner-normalized mean velocity profiles. Symbols are the same as in Table (2.1).

effectively incorporates the information contained in the entire pdf (i.e., incorporates the information in all moments), whereas, for example, the mean profile only reflects the behavior of the first moment. Conversely, it is expected that the diagnostic plot will convincingly express its self-similar behavior at the lowest δ^+. This is because it essentially constitutes the ratio of the two lowest order moments (second to first) of the underlying pdf.

2.3.3.1 Mean Velocity Profiles

Mean velocity profile data are plotted in Fig. 2.9. All profiles in Fig. 2.9 exhibit good agreement with logarithmic mean velocity profile, and particularly adhere to the logarithmic formula, $U+ = (0.387)^{-1} ln(y^+) + 4.32$, given by Marusic et al. (2013). These data also consistently collapse onto each other down towards the wall. The analysis of high

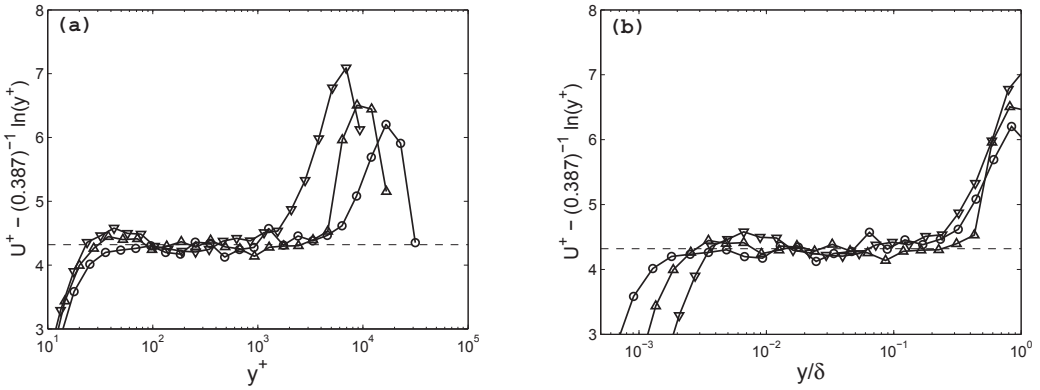

FIGURE 2.10: Deviation of the measured representative mean profiles from $0.387^{-1}ln(y^+)$; (a) versus y^+, (b) versus y/δ. $\bigtriangledown, Re_\tau = 6430$, $\bigtriangleup, Re_\tau = 10770$, $\circ, Re_\tau = 19670$. Horizontal line denotes $B = 4.32$.

Reynolds number pipe and boundary layer data by Marusic et al. (2013) indicates that the start of the logarithmic variation is empirically evaluated as $3\sqrt{\delta^+}$. Klewicki (2013b) revealed that the mean dynamics become wholly inertial near $y^+ \simeq 2.6\sqrt{\delta^+}$, and over the domain between this location and $y^+ \simeq 0.5\delta^+$, the mean velocity profile exhibits a logarithmic dependence associated with the self-similarity solution admitted by the mean momentum equation as $\delta^+ \to \infty$.

An unambiguous indication of the start point for the where U^+ becomes logarithmic cannot be discerned from the present mean profiles. By plotting the deviation of U^+ from the logarithmic line one can, however, assess this position to within an order of magnitude. Figs. 2.10 (a) and (b) respectively show representative profiles of the deviation from the logarithmic line under inner and outer normalized wall normal position. Here, the values of $k = 0.387$ and $B = 4.32$ are used (Marusic et al., 2013). These data show that the position where the data begin to approach the horizontal line moves outward under inner normalization and inward under outer normalization with increasing Reynolds number,

and thus at this level are in accord with the theoretical prediction. A distinctive Reynolds number trend indicated by the present data is that the near-wall bump in the profile is quite pronounced and rises above the logarithmic line at low δ^+. With increasing δ^+, the bump flattens and the entire profile shifts downward such that the logarithmic line is approached from below at higher Reynolds number. The evolution of the bump prior to the logarithmic region is associated with the scale separation between the near-wall region and outer region. It is where the inner length scale, ν/u_τ, transitions to the outer length scale, δ. This "bump" region has the intermediate length scale, $\sqrt{\nu\delta/u_\tau}$.

2.3.3.2 KLD Analysis

The present KLD analysis generically adheres to the procedures used in previous studies by Tsuji and Nakamura (1999), Lindgren et al. (2004), and Tsuji et al. (2005), but with some differences in detail. Estimating the pdf from experimental data involves normalizing the associated histogram. This histogram necessarily has a finite number of bins, and thus care must be taken in selecting the bin width. Several bin width values were tested to determine the range of sizes over which the final result remained invariant. Figs. 2.11 shows the dependence of the KLD on bin size at $\delta^+ = 6510$. Based upon analyses such as these, a bin size of 0.15σ (σ = standard deviation) was employed for the present analysis of KLD. This is consistent with the study of Tsuji et al. (2005), as is the range of u values employed to calculate the pdf, i.e., $-10\sigma \leqslant u \leqslant 10\sigma$.

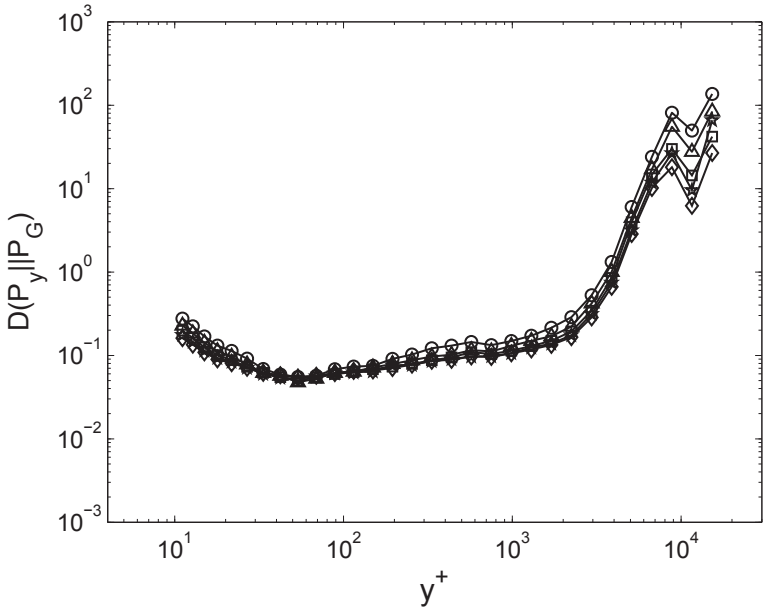

FIGURE 2.11: Effect of relative bin size on the calculated value of the KLD profile at $Re_\tau = 6510$; bin size= $0.1\sigma, \circ$; $0.125\sigma, \triangle$; $0.15\sigma, \square$; 0.175σ, $\star$; $0.2\sigma, \diamond$.

Fig. 2.12 and Fig. 2.13 present example KLD profiles at $\delta^+ = 6510$ and $\delta^+ = 10750$ respectively. For reference, these figures also show the mean velocity profiles. Three features are noted; the position where the KLD is a minimum, y_p^+ , and the starting and ending points of the (approximately) constant KLD region, y_s^+ and y_e^+ , respectively. At y_p^+ the pdf of u is closest to Gaussian. This position was quantified from the present data by simply locating the position where the measured KLD is a minimum.

In the previous studies, the criteria employed to identify the starting and ending points of the region where the pdfs of u are self-similar (approximately constant KLD) was either not used or not explicitly indicated. In the present analysis, these positions are self-consistently, yet subjectively defined. To do this, the region of the constant KLD was approximately located, and the average value of this region was computed. This average value is given by the horizontal dashed line in Fig. 2.11 and Fig. 2.12. The extent of the

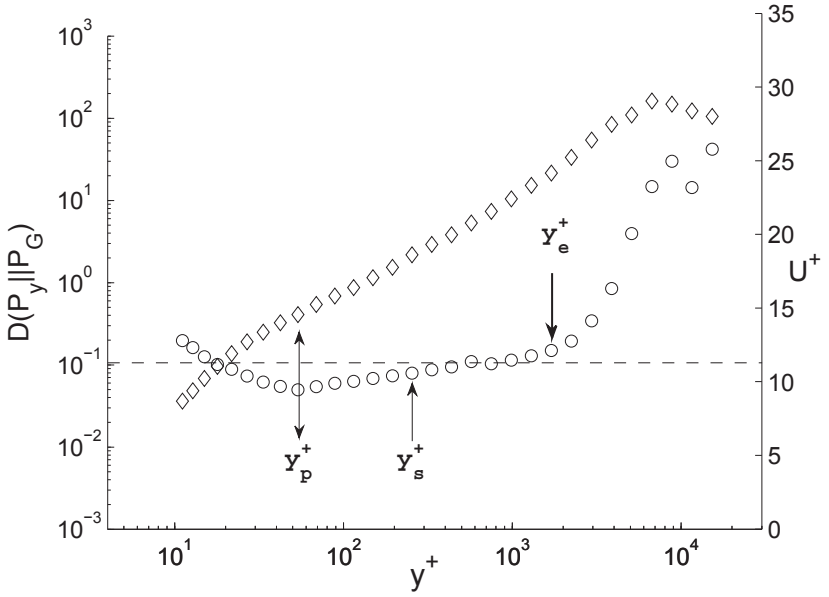

FIGURE 2.12: KLD (∘, left axis) profiles measured relative to a Gaussian pdf, and mean velocity profiles (◇, right axis) at $\delta^+ = 6510$. The position of the minimum KLD is given by y_p^+, while the starting and ending points of the region of approximately constant KLD are given by y_s^+ and y_e^+, respectively.

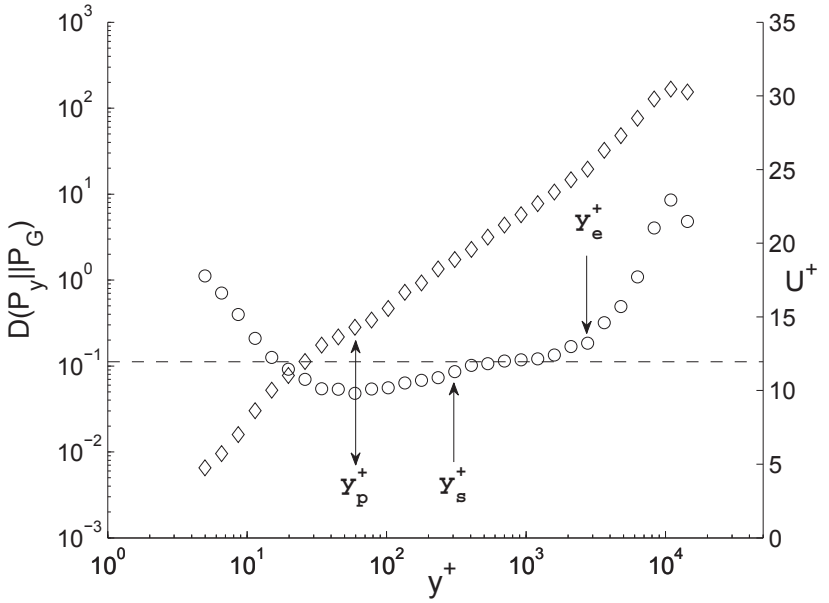

FIGURE 2.13: KLD (∘, left axis) profiles measured relative to a Gaussian pdf, and mean velocity profiles (◇, right axis) at $\delta^+ = 10750$. The position of the minimum KLD is given by y_p^+, while the starting and ending points of the region of approximately constant KLD are given by y_s^+ and y_e^+, respectively.

constant KLD region was then defined as those points that fell within ±40% of this average value. On face value, this criterion may seem somewhat large. The values of the average KLD are, however, only about 0.1, and thus in absolute terms the admitted variations are quite small (from about 0.07 to 0.14) relative to the orders of magnitude variation in KLD across the boundary layer. The 40% criterion exceeds the maximum value of the data scatter about the average line, and captures the scaling behaviors exhibited by the emerging region of increasingly constant KLD. In this regard, it is further noted that the vast majority of beginning and ending points easily fell within ±30% of the average value. The data of Fig. 2.11 and Fig. 2.12 (and those at other δ^+) also provide some evidence of a non-zero slope through the inertial layer of interest. This non-constancy is consistent with the finite δ^+ effects discussed at the beginning of this section.

As might be expected, the measured values of y_s^+ and y_e^+ predictably changed for variations in the criterion used to detect approximate constancy. For example, a smaller percentage criterion caused the starting point to move to larger y^+ and the ending point to shift to smaller y^+. For all reasonably defined criteria, however, these variations were relatively small and the underlying scaling properties reported herein were preserved, see below. Overall, the region of approximately constant KLD was always estimated to fall interior to the range between $2.6\sqrt{\delta^+}$ and $0.3\delta^+$.

The measured values of y_p^+ ranged from about 35 to 73, but did not exhibit any discernible trend with Reynolds number. This relatively large scatter stems from the minimum not occurring at a sharp peak, especially with increasing δ^+. The overall average value of y_p^+ is about 52.7. These findings agree with those by Tsuji et al. (2005),

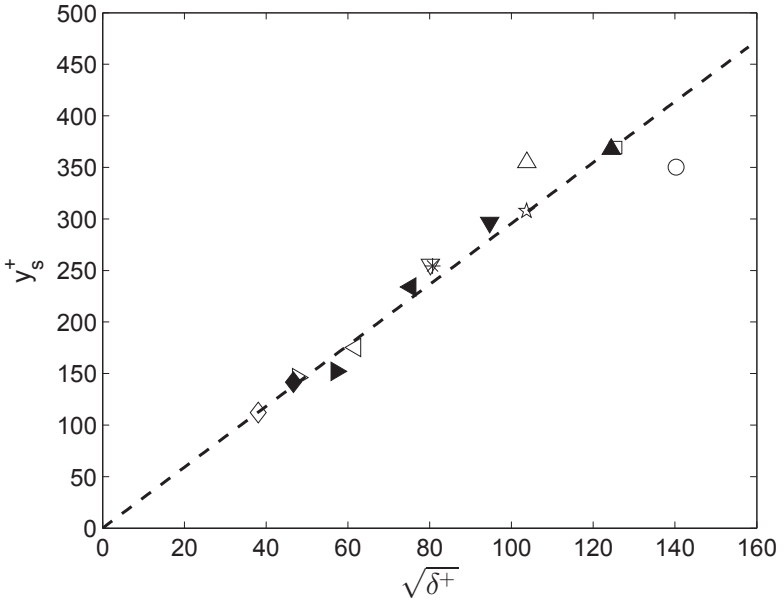

FIGURE 2.14: Reynolds number dependence of the starting point estimate for the constant KLD region. Curve fit is given by $y_s^+ = 2.95\sqrt{\delta^+}$.

as well as with their observation that y_p^+ correlates with the position where the $U^+(y^+)$ profile exhibits a shallow rise (bump) above the logarithmic line at least at lower δ^+.

The y_s^+ and y_e^+ values for the profiles listed in Table (2.1) were computed as just described. These values plotted versus Reynolds number in Fig. 2.14 and Fig. 2.15., reveals that the starting position of the self-similar region follows a $\sqrt{\delta^+}$ dependence, with a measured multiplicative coefficient of about 2.95. This result is different from what Tsuji et al. (2005) found, as they estimated that y_s^+ is essentially constant for $\delta^+ \gtrsim 1500$. In this regard, it is noted that the y_s^+ data in their study exhibits a mildly increasing trend with Reynolds number, and that the highest Reynolds number on their plot was $\delta^+ \simeq 4400$. The values of y_e^+ in Fig. 2.14 follow an approximately linear trend with increasing δ^+. The leading coefficient in the linear curve fit is about 0.28. This result is close to the value reported by Tsuji et al. (2005) of about 0.3. Here it is further noted

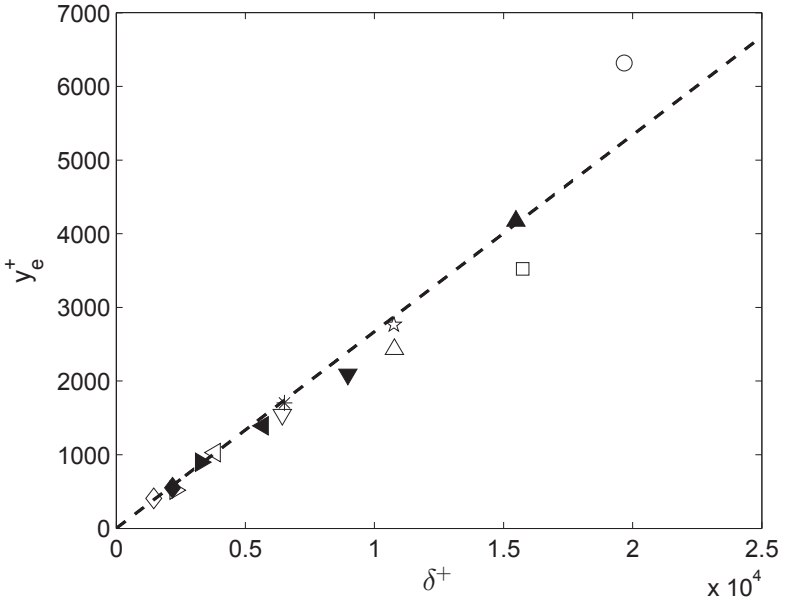

FIGURE 2.15: Reynolds number dependence of the ending point estimate for the constant KLD region. Curve fit is given by $y_e^+ = 0.27\delta^+$.

that if a $\pm 20\%$ criterion is used to detect the constant KLD region, then y_s^+ and y_e^+ shift to $3.21\sqrt{\delta^+}$ and $0.19\delta^+$, respectively. For either the 20% or 40% criteria, the increasing domain width with increasing δ^+ necessarily translates to a decreasing average slope, and thus supports the KLD approaching a constant the inertial domain as $\delta^+ \to \infty$. In regard to these scaling behaviors, it is also relevant to note that the similarity solution of the mean momentum equation reproduces the U^+ and T^+ profiles generated by low δ^+ DNS to within 0.1% over the domain $2.6\sqrt{\delta^+} \lesssim y^+ \lesssim 0.3\delta^+$ (Klewicki, 2013b).

2.3.3.3 Higher-Order Even Moments Analysis

Statistical moments of the u signals were computed up to $2p = 10$ for the data represented in Table (2.1). In accord with the last equality in (2.4), the profiles of these statistical moments were then plotted versus y^+. Similar to the variance profile, the higher-order

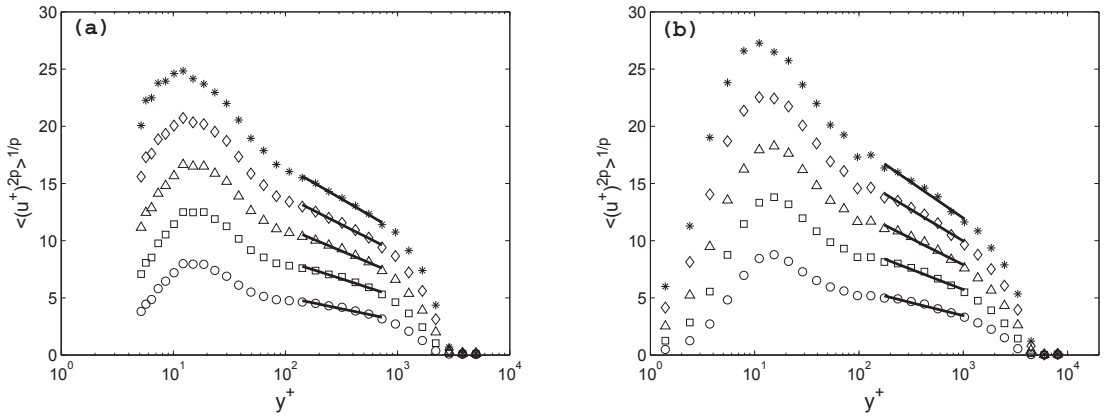

FIGURE 2.16: Statistical moment profiles of order $2p = 2(\circ), 4(\square), 6(\triangle), 8(\diamond)$ and $10(*)$ of the u signals at two Reynolds numbers less than 5000. (a) $\delta^+ = 2180$ and (b) $\delta^+ = 3820$.

even moments exhibit an inner peak near $y^+ = 5$, and an emerging mid-layer peak with increasing δ^+. Vincenti et al. (2013) demonstrated with the present data sets that the mid-layer peak in the variance profile emerges near $y^+ = 2.3\sqrt{\delta^+}$ to within about $\pm 0.4\sqrt{\delta^+}$. Given this, and the results of the KLD analysis, the moment profiles were fit to logarithmic decay curves over the domain $2.6\sqrt{\delta^+} \lesssim y^+ \lesssim 0.3\delta^+$. Note that the lower limit used here is different from the fixed value of $y^+ = 40$ used by Meneveau and Marusic (2013).

Representative profiles of the even moment profiles for $\delta^+ \lesssim 5000$ are shown in Fig. 2.16, while representative profiles for $\delta^+ \gtrsim 5000$ are shown in Fig. 2.17. Each of these profiles includes the curve fit according to the logarithmic decay Eq. (2.4). As is apparent, with increasing δ^+ the middle region of each profile shows evidence of an emerging plateau that eventually develops into a mild peak. It is beyond this peak that the logarithmic decay must occur. Recalling that the curve fits on these figures are over the domain $2.6\sqrt{\delta^+} \lesssim y^+ \lesssim 0.3\delta^+$, it also becomes apparent that the onset of the zone of

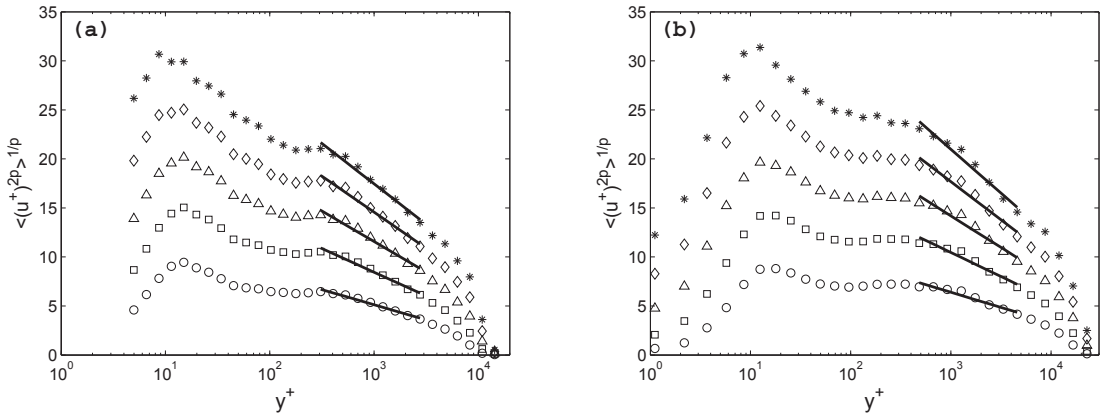

FIGURE 2.17: Statistical moment profiles of order $2p = 2(\circ), 4(\square), 6(\triangle), 8(\diamond)$ and $10(*)$ of the u signals at two Reynolds numbers greater than 5000. (a) $\delta^+ = 10750$ and (b) $\delta^+ = 19670$.

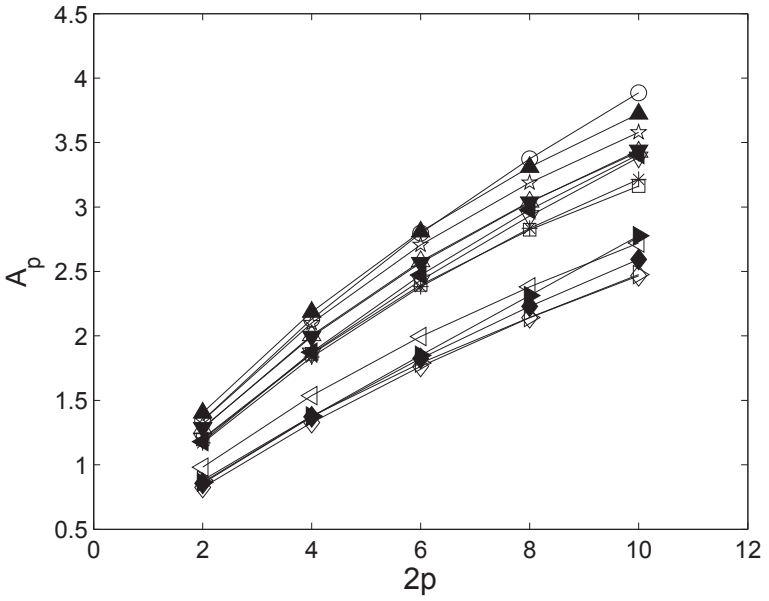

FIGURE 2.18: Logarithmic slope coefficients, A_p, values as a function of even moment $2p$. Symbols are the same as in Table (2.1).

logarithmic decay begins near to or just beyond where the leading order mean dynamics become wholly inertial.

Behaviors associated with the totality of the A_p are graphically summarized in Fig. 2.18 and Fig. 2.19. Regarding the uncertainty of these estimates, it is relevant to note that

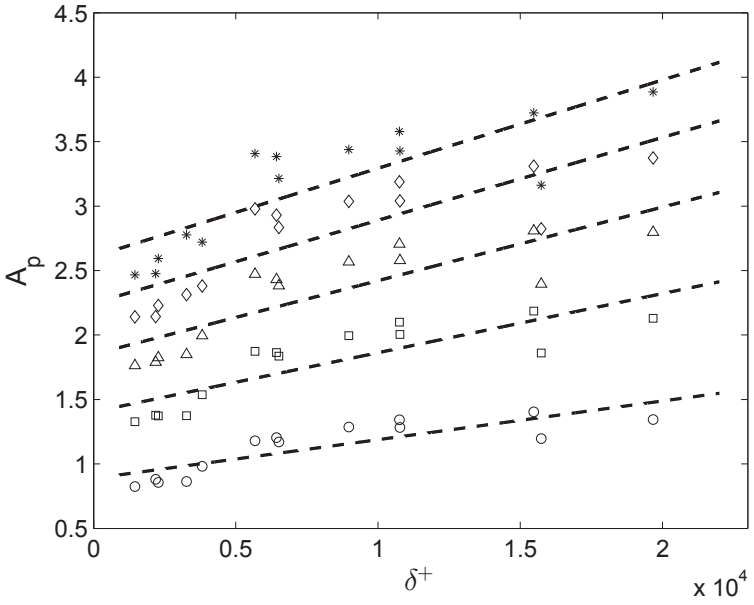

FIGURE 2.19: Logarithmic slope coefficients, A_p, values as a function of δ^+; $2p = 2, \circ; 2p = 4, \square; 2p = 6, \triangle; 2p = 8, \diamond$ and $2p = 10, *$. Dashed lines are a linear fit over all δ^+.

the deviation of the individual data points from the respective logarithmic curve fit is at most about 7%, but more typically is considerably less. Fig. 2.17 shows curves of the A_p values for each δ^+ plotted versus the order of the even moment, $2p$. As is apparent, the data nominally segregate into two similar sets of curves; one cluster for $\delta^+ \lesssim 5000$ and another cluster for $\delta^+ \gtrsim 5000$. Comparison indicates that the $\delta^+ \gtrsim 5000$ grouping of curves is similar, but not identical, to those presented in the study of Meneveau and Marusic (2013). This is consistent, since they primarily considered flows having δ^+ greater than 5000.

The distinction between the lower δ^+ and higher δ^+ behaviors is similarly reflected by individually plotting the A_p values for each moment as a function of Reynolds number, as shown in Fig. 2.18. In this figure, the linear curve fit that considers the full δ^+ range

TABLE 2.2: Logarithmic slope coefficients, A_p, of the higher-order even moment curve fits up to $2p = 10$ for $\delta^+ > 5000$.

δ^+	5680	6340	6510	8970	10750	10770	15480	15740	19670	Average
A_1	1.18	1.20	1.17	1.29	1.34	1.28	1.41	1.20	1.35	1.27
A_2	1.87	1.86	1.84	2.00	2.10	2.00	2.19	1.86	2.13	1.98
A_3	2.47	2.43	2.38	2.57	2.17	2.57	2.81	2.40	2.80	2.51
A_4	2.98	2.93	2.84	3.04	3.19	3.04	3.31	2.82	3.37	3.06
A_5	3.41	3.38	3.22	3.44	3.58	3.42	3.72	3.16	3.89	3.47

helps to clearly reveal that the data undergo a nearly discrete jump near $\delta^+ = 5000$, and then exhibit a much slower variation for greater δ^+. This much smaller variation for $\delta^+ \gtrsim 5000$ is potentially indicative of an approach to an asymptotic value, as suggested by the $2p = 2$ pipe data presented in Marusic et al. (2013) at much higher δ^+.

The logarithmic slope coefficients, A_p, for the flows with $\delta^+ > 5000$ are presented in Table (2.2), with their average values given in the final column. It is noted that the present average for A_1 is 1.27, which is close but not identical to the value reported by Marusic et al. (2013). On the other hand, while the values of the present $A_2 - A_5$ are qualitatively similar to those presented in Meneveau and Marusic (2013), at nominally the same δ^+ the present data exhibit slightly higher values for each moment. Some of this difference can be explained by the fact that they used a boundary layer thickness that is about 15% larger than the present $\delta = \delta_{99}$, and thus when δ_{99} is consistently employed their δ^+ values decreased by about 15%.

Well-resolved data indicate that the inner-normalized near-wall peak in the velocity variance in boundary layers increases with increasing δ^+ (Metzger and Klewicki, 2001; Hutchins et al., 2009). Consistent with this, and the results for $2p > 2$ reported by

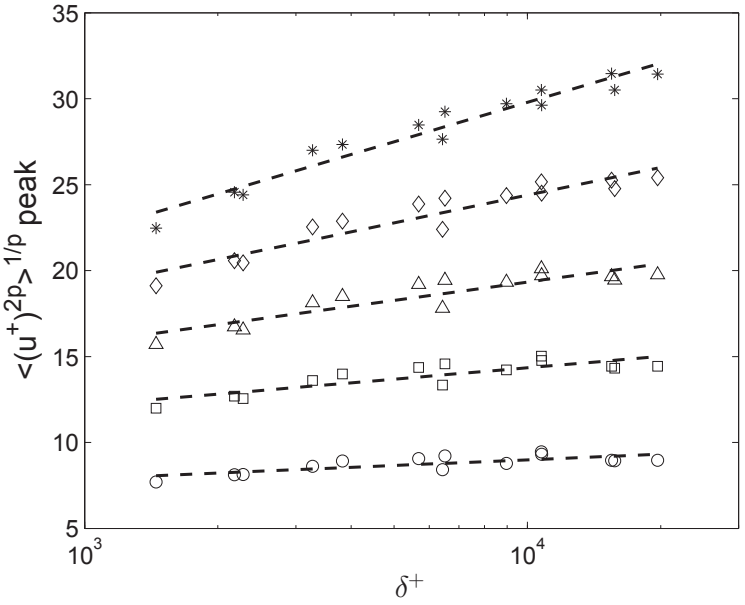

FIGURE 2.20: Near-wall peak values of moments of order $2p = 2(\circ), 4(\square), 6(\triangle), 8(\diamond)$ and $10(*)$ plotted as a function of δ^+. The dashed lines are logarithmic curve fits according to Eq. (2.5).

Meneveau and Marusic (2013), the present higher-order even moment profiles also exhibit an increasing trend in their near-wall peak values. These peak values are plotted versus δ^+ in Fig. 2.20. The replicated Reynolds numbers in this figure near $\delta^+ = 6500, 11000$ and 15000 provide an indication of the uncertainty of these measurements. The present data indicate that with increasing p the position of the peak undergoes a mild shift toward the wall. Namely, for $2p = 2$ the peak is close to $y^+ = 15$, while for $2p = 10$, the peak occurs near $y^+ = 10$.

The peak values for each moment were fit to a logarithmic curve in Fig. 2.19 according to

$$\left\langle \left(u^+\right)^{2p} \right\rangle_{peak}^{1/p} = J_p ln\left(\delta^+\right) + K_p, \tag{2.5}$$

with the fit parameters listed in Table (2.3). While qualitatively similar to the results

TABLE 2.3: Coefficients in the curve fits of Eq. (2.5) describing the increase in the near-wall peak with δ^+, and a comparison of the multiplicative coefficients, A_p and J_p.

$2p$	2	4	6	8	10
J_p	0.46	0.93	1.53	2.34	3.35
K_p	4.75	5.76	5.27	2.91	−0.93
A_p	1.27	1.98	2.51	3.06	3.47
J_p/A_p	0.36	0.47	0.61	0.76	0.97

reported in Meneveau and Marusic (2013), the results of Fig. 2.19 and Table (2.3) exhibit some notable differences. As with the A_p data of Fig. 2.18, for any given p the present data are slightly greater than their similar δ^+ result. Furthermore, the present δ^+ dependence of the higher-order moments is slightly more pronounced than what their data indicate. They also report that for $2p = 8$ and 10, $J_p \simeq A_p/2$. The present data, however, exhibit a trend that is quantitatively different from this. For $2p = 2$, the present slope is less than $A_p/2$, and for increasing moment the ratio of J_p to A_p increases such that it approaches unity for $2p = 10$. The reasons for this observed difference are not known, but may at least be partly associated with the difference in the domain used to determine the A_p, and our selection of the actual near-wall peak value rather than the value of the moment at $y^+ = 15$. It is lastly noted that the interesting observation that for each increase in $2p$ the ratio J_p/A_p (last row in Table (2.3)) increases by a constant factor of about 1.26.

2.3.3.4 Diagnostic Plot

Fig. 2.21 and Fig. 2.22 respectively present the original diagnostic plot and the modified diagnostic plot as described by Alfredsson and Örlü (2010) and Alfredsson et al. (2011). Relative to the initial intended use of the diagnostic plot, the data near the wall deviate

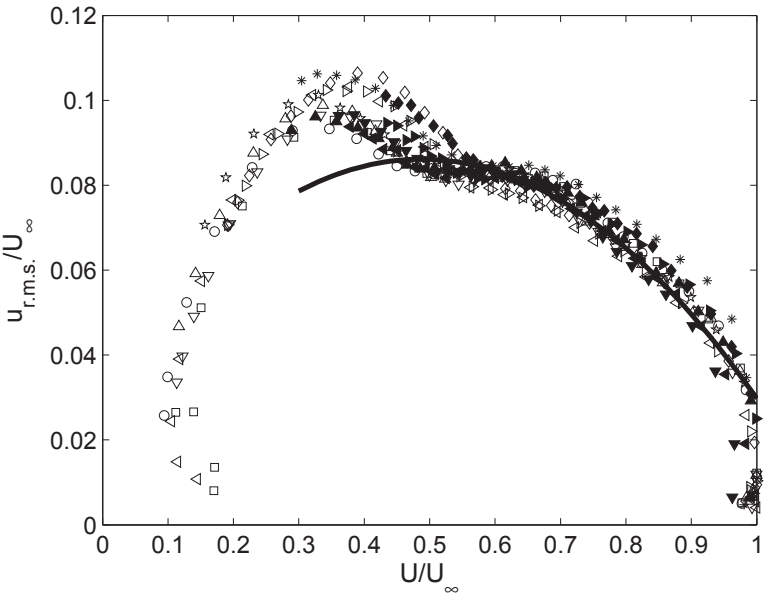

FIGURE 2.21: Original diagnostic plots of the streamwise velocity intensity as derived from the data of Table (2.1). Quadratic curve fit is given by $u_{r.m.s}/U_\infty = -0.215\,(U/U_\infty)^2 + 0.209\,(U/U_\infty) + 0.035$.

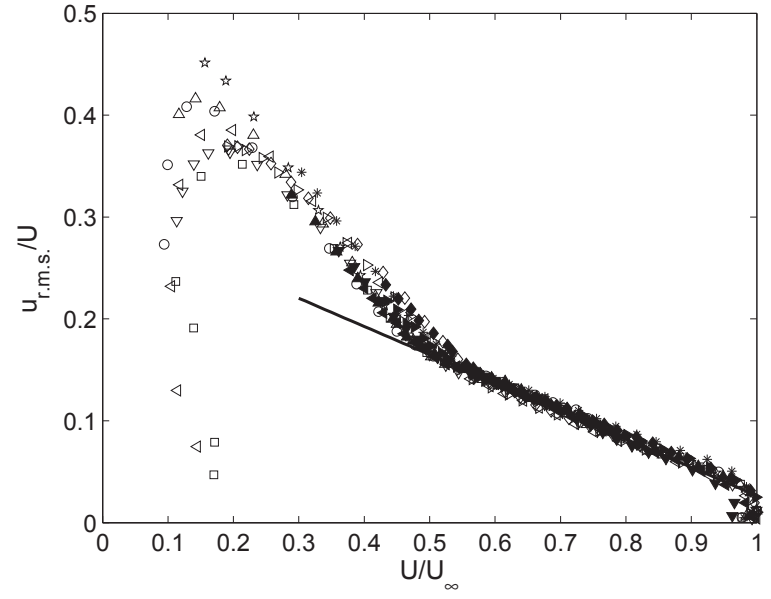

FIGURE 2.22: Modified diagnostic plots of the streamwise velocity intensity as derived from the data of Table (2.1). Linear curve fit is given by $u_{r.m.s.}/U = -0.277\,(U/U_\infty) + 0.303$.

from a monotone decay toward zero, and this indicates that the data very close to the wall are not correct. Note further that in Fig. 2.21 the data in the outer region of interest follow a quadratic curve, while those in Fig. 2.22 convincingly adhere to a straight line over the horizontal axis coordinates between about 0.55 and 0.9. Relative to Fig. 2.22, the present data yield slightly different fit parameters than found by Alfredsson et al. (2011), but the overall agreement and evidence of linear dependence is compelling. Both plots reveal that the mean and rms streamwise velocity profiles vary self-similarly over this domain. A primary aim of the present analysis is to quantify the extent of this self-similar region in spatial (y^+) coordinates, and compare this with the domain where mean momentum equation exhibits its $\phi \to \phi_c$ self-similarity.

The bounds of the linear region in Fig. 2.22 were determined as follows. For each Reynolds number the data were fit to a line using data in the middle of the region where the linear dependence unambiguously holds. Data points were then successively added to both sides of this subdomain, and the curve fit was updated. With each addition of data points, the curve fit became more robust. For all of the data that reliably fell within in the linear region, the maximum deviation from the straight line fit was less than 8%. Eventually, however, the newly added data deviated from the line fit by more than 8%, and the locations of the data points immediately adjacent to these were identified as the starting and ending positions of the linear region. As before, these positions are denoted as y_s^+ and y_e^+ , respectively.

The y_s^+ and y_e^+ values for the data of Table (2.1) are respectively plotted versus δ^+ in Fig. 2.23 and Fig. 2.24. These plots indicate that $y_s^+ \simeq 2.55\sqrt{\delta^+}$, and $y_e^+ \simeq 0.51\delta^+$.

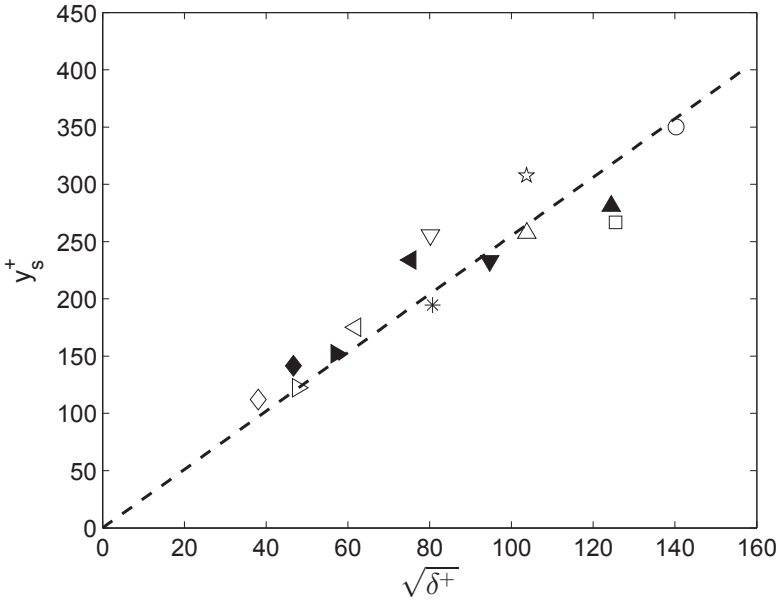

FIGURE 2.23: Reynolds number dependence of the starting point estimates for the linear region on the diagnostic plot. Curve fit is given by $y_s^+ = 2.55\sqrt{\delta^+}$.

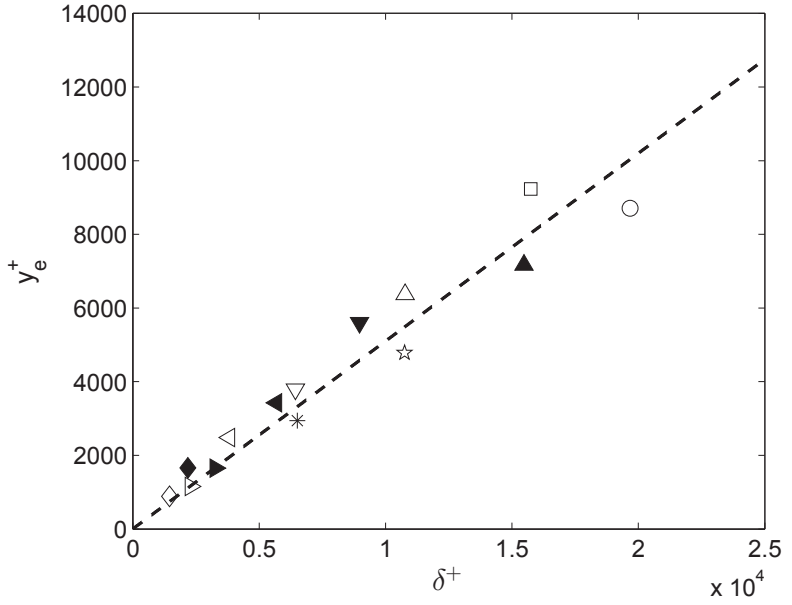

FIGURE 2.24: Reynolds number dependence of the ending point estimates for the linear region on the diagnostic plot. Curve fit is given by $y_e^+ = 0.51\delta^+$.

Thus, to within the scatter of the data the diagnostic plot domain of self-similarity is indistinguishable from that associated with the $\phi \to \phi_c$ self-similarity admitted by the mean momentum equation.

Relative to the coordinates of Fig. 2.22, Alfredsson and Örlü (2010) and Alfredsson et al. (2011) note that the mid-layer peak in $\langle u^2 \rangle^+$ will emerge if the region of linear dependence extends to sufficiently low values of U/U_∞. They estimate this value to be $U/U_\infty \simeq 0.55$. Given this, it is relevant to describe how these and other empirical observations connect to the mean flow theory of Fife et al. (2005a). The analysis by Vincenti et al. (2013) provides evidence that the position of the mid-layer peak occurs at about $y^+ = 2.3\sqrt{\delta^+} + 0.4\sqrt{\delta^+}$. Scalings derived from analysis of the mean momentum equation indicate that the value of U^+ at the outer edge of layer III is approximately $U^+ = 0.5U_\infty^+ + 3.6$. Thus, according to the theory, the value of U/U_∞ at this location is weakly Reynolds number dependent and asymptotically approaches 0.5. Consistent with this, the data of Fig. 2.21 and Fig. 2.22 indicate that the position of the outer peak occurs where $U/U_\infty \simeq 0.62$, while the region of linear dependence in the diagnostic plot starts closer to 0.55. This slight discrepancy is similar to the results noted by Klewicki (2013b) relative to the slope of mean velocity gradient profile, and the apparent start of the region of logarithmic U^+. This observation is probably at least partially connected to the capacity to accurately discern properties from experimental measurements; especially in layer III where the balance exchange of dominant order terms that leads to inertial mean dynamics occurs. Overall, however, it would seem that the empirical observations by Alfredsson et al. (2011) are consistent with the Reynolds number dependent properties

derived from the mean equation based theory.

2.4 Summary

Two primary conclusions are noted:

1. The region where the KLD and even moment profiles exhibit evidence of emerging self-similar behavior are indistinguishable from each other to within the present data scatter. This region of emerging self-similarity scales like but lies interior to the estimated bounds, $2.6\sqrt{\delta^+} \lesssim y^+ \lesssim 0.5\delta^+$, of the inertial domain associated with the $\phi \to \phi_c$ self-similarity formally admitted by the mean dynamical equation.

2. To within the scatter of the present measurements, the self-similar domain of the diagnostic plot is indistinguishable from $2.6\sqrt{\delta^+} \lesssim y^+ \lesssim 0.5\delta^+$.

At a minimum, these findings reveal a strong correlation between the domain where the three empirical measures indicate self-similarity, and the $\phi \to \phi_c$ domain determined through analysis of mean momentum equation.

A physical interpretation of the present findings is gained by the depiction of Fig. 2.25. Adapted from the study of Klewicki (2013a), this figure describes the mechanisms and scaling behaviors associated with the relative scale separation between the characteristic motions of the velocity and vorticity fields in the boundary layer.

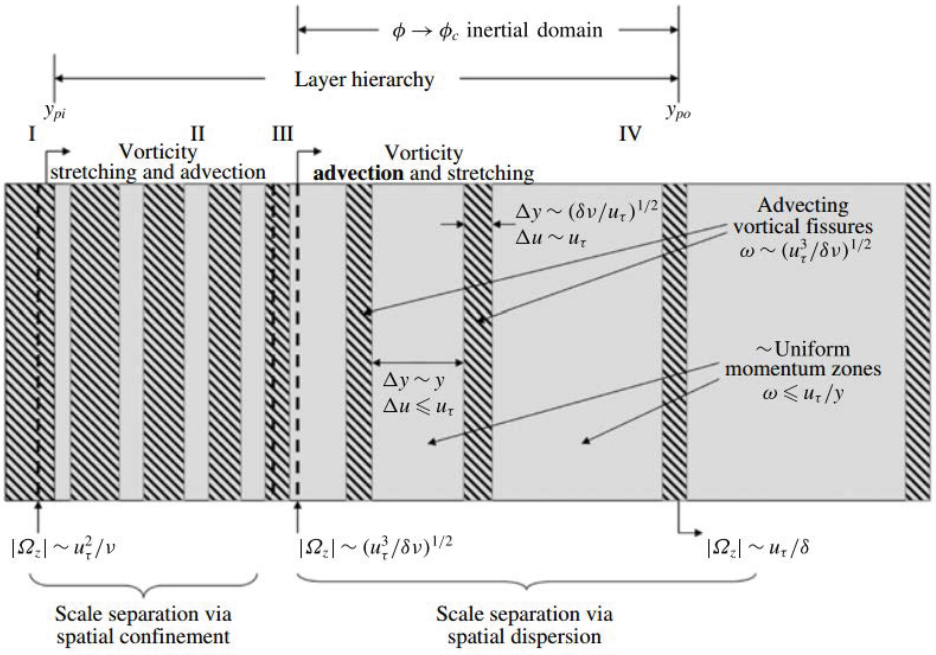

FIGURE 2.25: Depiction of the vorticity field attributes in turbulent wall-flows. The dominant processes responsible for scale separation between the velocity and vorticity fields change across layer III. The velocity field motions (light gray) are space-filling throughout the flow. The vorticity field motions (hatched regions) are confined to a sub-volume near the wall via vorticity stretching, and then the resulting thin regions of concentrated vorticity (vortical fissures) are dispersed by advective transport over the upper portion of the layer hierarchy (inertial subdomain of present interest) where $\phi \to \phi_c$ as $\delta^+ \longrightarrow \infty$. Figure is adapted from Klewicki (2013b).

Near the wall there is intense vorticity stretching and reorientation. This results in the vigorous three-dimensionalization of the vorticity field with wall-normal distance. This vorticity stretching also causes a relative reduction in the scale of the concentrated vortical motions, and an exchange of mean flow enstrophy to fluctuating enstrophy (Klewicki, 2013a). Although not depicted in Fig. 2.25, existing data suggest that, independent of δ^+, most of the mean-to-fluctuating enstrophy exchange occurs in the region $y^+ \lesssim 40$ (Klewicki, 2013a). The completion of this randomizing process may have connection to the present and previous observations indicating that the KLD attains its minimum relative to a Gaussian pdf just beyond this region, i.e., near $y^+ = 50$.

The region of primary present interest, however, is the inertial portion of the scaling layer hierarchy that resides beyond the outer edge of layer III ($y^+ \gtrsim 2.6\sqrt{\delta^+}$). Here both vorticity and momentum transport predominantly occur via advective transport, i.e., for momentum by the mean inertia and turbulent inertia mechanisms . Analysis of mean vorticity and vorticity fluctuation statistics leads to the inertial layer depiction. Consistent with the findings of Meinhart and Adrian (1995) and Adrian et al. (2000) and velocity vorticity product measurements at high δ^+ (Priyadarshana et al., 2007), this flow domain is characterized by large scale zones of nearly uniform momentum that are segregated by narrow (high aspect ratio) regions of elevated vorticity so-called vortical fissures (Priyadarshana et al., 2007). On this domain, $W^+(y^+)$ approaches a linear function, and over the extent of this region the magnitude of the mean vorticity, $\mid \Omega_z \mid$, attenuates from $O\left(\sqrt{u_\tau^3/\delta\nu}\right)$ to $O(u_\tau/\delta)$. These behaviors are associated with the mean momentum equation admitting a logarithmic mean solution. The decrease in $\mid \Omega_z \mid$, along with the continuing effect of vorticity stretching, leads to a self-similar increase in the vorticity intensities relative to $\mid \Omega_z \mid$ across the inertial layer (Klewicki, 2013a).

With increasing δ^+ the vorticity fluctuations are increasingly concentrated in the narrow vortical fissures. Thus, the depiction of Fig. 2.25 suggests that the logarithmic decrease in the moments of u stems from the decreasing difference between the uniform momentum zone velocities and the local U value as y approaches δ. Similarly, this same depiction suggests that the diagnostic plot is the velocity field complement of the self-similarity between the mean vorticity and vorticity intensities noted above. Namely, with each linear increment in mean velocity (associated with a logarithmic step in y^+ and

the above noted attenuation of $|\ \Omega_z\ |$), there is a decreasing difference between u^+ and the range of velocities in the uniform momentum zones at the given y^+ position. Overall, these interpretations lead one to further suspect that the measures of self-similarity investigated herein are manifestations of the self-similar behaviors admitted by mean momentum equation.

The similarity solution to the mean momentum equation is accomplished by analytically determining the coordinate stretching, ϕ, that yields an invariant form of the mean dynamical equation. This theory faithfully does not rely upon additional assumptions or hypotheses. As such, the interpretation for the emergence of the mid-layer peak in $\langle u^2 \rangle^+$ quite naturally derives from its correlation with the onset of the inertial layer at $y^+ \simeq 2.6\sqrt{\delta^+}$. Townsend (1980) associates the logarithmic behaviors for U^+ and $\langle u^2 \rangle^+$ with the action of his attached eddy hierarchy. The Biot-Savart basis of the attached eddy model naturally places this hierarchy on the inertial sublayer of present interest. Accordingly, the onset of this inertial layer also coincides with where Townsends outer layer similarity hypothesis should become valid. The leading order behaviors of mean momentum equation indicate that this domain starts at the outer edge of layer III, which for the smooth-wall flow is located at $y^+ \simeq 2.6\sqrt{\delta^+}$. More generally (e.g., for rough-wall flows), the outer edge of layer III is where the viscous force term loses leading order importance.

Castro et al. (2013) demonstrated that the diagnostic plot properties are also retained on an outer domain in rough-wall flows. Mehdi et al. (2013) showed that the layer II−IV structure is generically preserved in rough-wall flows, but that the transitions from layer to

layer depend on the combined effects of roughness and Reynolds number. Consistent with the present findings that the linear region of the diagnostic plot coincides with the domain where the mean momentum equation admits its $\phi \rightarrow \phi_c$ self-similarity, Mehdi et al. (2013) provide evidence that for rough-wall flows the onset of the outer layer similarity approximation still physically occurs where the viscous force term loses leading order importance provided that the signature of the motions directly created by the roughness is sufficiently attenuated by the three-dimensionalization processes interior to the outer edge of layer III. These findings thus provide evidence that the coincidence between the inertial portion of the layer hierarchy and and the linear region of the diagnostic plot also extends to rough-wall flows.

CHAPTER 3

SCALING PROPERTIES OF KINETIC ENERGY BUDGETS IN WALL TURBULENCE

3.1 Background

Efforts to describe kinetic energy and kinetic energy equation behaviors in turbulent wall-flows arguably began in earnest with the experimental studies by Laufer and Klebanoff (Laufer, 1951, 1954; Klebanoff, 1955). As remains the case for physical experiments today, analyses were conducted without the benefit of the comprehensive quantification of terms that is now provided by direct numerical simulations, DNS. These earlier descriptions were generally given within the context of the traditional layer structure just described, and often (but not exclusively) focused on the turbulence kinetic energy (TKE). These early measurements revealed that not all terms in the TKE budget are leading order across the entire flow, and in particular the production and dissipation terms were found to nominally comprise the leading balance across the logarithmic layer. Guided by such measurements, subsequent analyses and interpretations were made within the context of

the budget equations. Using his attached eddy concepts, Townsend (Tennekes and Lumley, 1976) surmised that in the logarithmic layer the streamwise and spanwise velocity fluctuation contributions to the TKE are, in the asymptotic limit, given by functions that logarithmically decrease with distance from the wall, with the wall-normal velocity fluctuation contribution approaching a constant. Townsend further described equilibrium boundary layer energy transport as consisting of an inward flux of mean kinetic energy that is coincident with an outward flux of turbulence energy, and with the primary conversion of mean to turbulence kinetic energy occurring in the logarithmic layer and below. Near the outer edge, he surmised that the approximate balance is between the advection and turbulent transport terms, and thus is inviscid at leading order. The approximate balance between production and dissipation in the logarithmic layer is often employed in wall-turbulence scaling arguments, and is regularly used to explain the existence of a logarithmic mean profile, e.g., (Tennekes and Lumley, 1972; Davidson, 2015)

Of course, the interest in Reynolds number effects also extends to the TKE equation. As such, an equation based characterization of the leading balances, similar to that just given for the mean momentum equation, is desired. The difficulties in obtaining accurate experimental measurements of the relevant quantities postponed the accurate determination of each term in the TKE budget until the advent of DNS. Since the early DNS of Mansour et al. (1988), numerous other studies have explored the behavior of the terms in the TKE equation (Spalart, 1988; Antonia and Kim, 1994; Moser et al., 1999; Coleman et al., 2003). From these studies, it is probably safe to surmise that a clear scaling structure to the TKE budget (and associated Reynolds stress budgets) has yet to emerge

(Hoyas and Jiménez, 2008).

Some general behaviors are, however, known to hold. At the wall the dissipation term is maximal and is balanced with the viscous diffusion term. Near the wall, the dissipation term balances with the sum of the viscous diffusion and pressure diffusion terms. Moving away from the wall, the pressure diffusion term is small compared to other terms, and the turbulent diffusion term becomes important. This term is positive near the wall, but negative for $8 \lesssim y^+ \lesssim 30$. It thus plays a role in transporting TKE towards the wall. In the region $y^+ \gtrsim 30$, however, the balance is nominally composed of the production and dissipation terms. It is rationally expected that both the dissipation term, which is dependent on small scale structure, and the turbulent diffusion term, which is typically associated with larger scales, are sensitive to Reynolds number via the effects of scale separation. Also, above the traditional buffer layer, most terms in the TKE transport equation scale reasonably well with u_τ^3/δ. Within the viscous and buffer layers, inner-normalization, u_τ^4/ν, seems to apply, but the inner scaling works poorly very close to the wall, especially for the dissipation and pressure-related terms. The former is attributed to the effect of the large scale motions, and the latter is due to the scaling of pressure itself (Hoyas and Jiménez, 2008).

The above and similar descriptions of kinetic energy transport are referenced to the traditional layer structure. The relevance of this structure to scaling the flow field energetics is, however, not well-established. Given this, the present study mimics the more recent approach used in the analysis of the mean momentum equation (Wei et al., 2005a). This approach is used to explore the mean, turbulence, and total kinetic energy balances

in planar channels, circular pipes, and flat plate boundary layer flows. The DNS and LES data from Hoyas and Jiménez (2008); El Khoury et al. (2013); Bernardini et al. (2014); Eitel-Amor et al. (2014); Lee and Moser (2015) are used in the analysis. The analysis reveals that the leading order layer structure of the mean kinetic energy balance is identical to that of the mean momentum balance, while for Reynolds numbers available to DNS, the profiles of the terms in the turbulence kinetic energy equations are very similar in pipes and channels. The present analyses indicate that there exists a four-layer structure to the total kinetic energy budget equation, with the property that in each of these layers a balance occurs between a subset of the relevant terms. This layer structure is, however, shown to be distinct from the layer structure of the mean momentum balance. The Reynolds number dependent scaling of the thickness of each layer is empirically quantified using DNS data, and for one layer (layer iii) is also analytically reasoned. The physical processes associated with each layer and their connections to the kinetic energy balance for the mean flow and turbulence are also discussed and clarified.

3.2 Kinetic Energy Budgets

In the following, x denotes the streamwise direction, y is the wall-normal direction, with the spanwise direction given by z. Uppercase letters or angle brackets denote the averaged quantities, and lowercase letters indicate fluctuations about the mean. The x, y, and z velocity components are given by variants of u, v, and w, respectively, and δ is used to denote the half channel height, pipe radius or boundary layer thickness.

3.2.1 Mean Kinetic Energy Budgets

Consideration of the mean kinetic energy balance reveals an important connection to the structure of the mean dynamics. With the Reynolds stress denoted by $\tau_{ij}^R = -\langle u_i u_j \rangle$, in a Cartesian system the balance equation for the mean kinetic energy, $E = 1/2\,(U_i U_i)$, is

$$\frac{\partial}{\partial t}\left(\frac{1}{2}U_i U_i\right) + U_k \frac{\partial}{\partial x_k}\left(\frac{1}{2}U_i U_i\right) = -\frac{1}{\rho}\frac{\partial}{\partial x_i}\left(U_i P\right) + \nu U_i \frac{\partial^2 U_i}{\partial x_k \partial x_k} + U_i \frac{\partial}{\partial x_k}\tau_{ij}^R, \qquad (3.1)$$

where the conventions of indicial notation are taken to hold.

3.2.1.1 Fully Developed Turbulent Channel and Pipe Flows

Statistically stationary and fully developed turbulent flow in a planar channel or circular pipe with smooth walls is considered. Since this flow is both planar (axis-symmetric) and fully developed, derivatives of averaged quantities with respect to x and z are zero, and such mean quantities are solely a function of y, e.g., $U = U\,(y)$. For the pipe, the coordinate transformation, $y = \delta - r$, yields the same equations as the channel.

The condition of a steady flow in the mean yields

$$\frac{\partial}{\partial t}\left(\frac{1}{2}U_i U_i\right) = 0, \qquad (3.2)$$

while the fully developed condition and $V = W = 0$ give

$$U_k \frac{\partial}{\partial x_k}\left(\frac{1}{2}U_i U_i\right) = \underbrace{U\frac{\partial}{\partial x}\left(\frac{1}{2}U_i U_i\right)}_{\frac{\partial}{\partial x}=0} + \underbrace{V\frac{\partial}{\partial y}\left(\frac{1}{2}U_i U_i\right)}_{V=0} = 0, \tag{3.3}$$

$$-\frac{1}{\rho}\frac{\partial}{\partial x_i}\left(U_i P\right) = U\left(-\frac{1}{\rho}\frac{\partial P}{\partial x}\right). \tag{3.4}$$

Now a basic relation between the mean pressure gradient and the friction velocity for fully developed channel flow is invoked

$$-\frac{\delta}{\rho}\frac{\partial P}{\partial x} = u_\tau^2, \tag{3.5}$$

where $u_\tau = \sqrt{\tau_w/\rho}$, and δ is the half-channel height. This gives

$$-\frac{1}{\rho}\frac{\partial}{\partial x_i}\left(U_i P\right) = \frac{u_\tau^2}{\delta}U. \tag{3.6}$$

Moreover, simplification for the given flow yields

$$\nu U_i \frac{\partial^2 U_i}{\partial x_k \partial x_k} = \nu\frac{\partial^2\left(\frac{1}{2}U_i U_i\right)}{\partial x_k \partial x_k} - \nu\frac{\partial U_i}{\partial x_k}\frac{\partial U_i}{\partial x_k} = \nu\frac{d^2}{dy^2}\left(\frac{1}{2}U^2\right) - \nu\frac{dU}{dy}\frac{dU}{dy}, \tag{3.7}$$

and

$$U_i\frac{\partial \tau_{ik}^R}{\partial x_k} = -U\frac{d\left\langle uv\right\rangle}{dy}. \tag{3.8}$$

Combination of the results gives the simplified form of the transport equation for the mean kinetic energy for statistically stationary and fully developed turbulent flow in a

planar channel

$$\frac{u_\tau^2}{\delta}U + \nu\frac{d^2}{dy^2}\left(\frac{1}{2}U^2\right) - \nu\frac{dU}{dy}\frac{dU}{dy} - U\frac{d\left\langle uv\right\rangle}{dy} = 0. \tag{3.9}$$

The terms in Eq. (3.9) are now normalized using u_τ and ν. Following convention, this inner-normalization is denoted by a superscript "+".

$$U^+ = \frac{U}{u_\tau}, \left\langle uv\right\rangle^+ = \frac{\left\langle uv\right\rangle}{u_\tau^2}, y^+ = \frac{yu_\tau}{\nu}. \tag{3.10}$$

Note that δ appears owing to (3.6). Letting $T^+ = -\left\langle uv\right\rangle^+$, subsequent rearrangement yields the inner-normalized equation for the mean kinetic energy in fully-developed turbulent channel flow

$$\frac{d^2}{dy^{+2}}\left(\frac{1}{2}U^{+2}\right) + U^+\frac{dT^+}{dy^+} - \frac{dU^+}{dy^+}\frac{dU^+}{dy^+} + \frac{1}{\delta^+}U^+ = 0. \tag{3.11}$$

The four terms presented in Eq. (3.11) are physically referred to as mean viscous diffusion (MVD), rate of work by net Reynolds stress (WRS), mean dissipation (MD) and mean pressure diffusion (MPD).

3.2.1.2 Zero-Pressure Gradient Turbulent Boundary Layer

Relative to the channel or pipe, the differences in developing the evolution equation for the flat plate boundary layer are associated with mean streamwise advection and a zero

mean pressure gradient. Like the channel/pipe flows, the derivatives with respect to z are zero.

The condition of a steady flow in the mean yields,

$$\frac{\partial}{\partial t}\left(\frac{1}{2}U_iU_i\right)=0, \tag{3.12}$$

While the developing condition in the streamwise direction with the boundary layer approximations and the zero mean pressure gradient give

$$U_k\frac{\partial}{\partial x_k}\left(\frac{1}{2}U_iU_i\right)=U\frac{\partial}{\partial x}\left(\frac{1}{2}U_iU_i\right)+V\frac{\partial}{\partial y}\left(\frac{1}{2}U_iU_i\right)=U\frac{\partial}{\partial x}\left(\frac{1}{2}U^2\right)+V\frac{\partial}{\partial y}\left(\frac{1}{2}U^2\right), \tag{3.13}$$

$$-\frac{1}{\rho}\frac{\partial}{\partial x_i}\left(U_iP\right)=0. \tag{3.14}$$

The other terms are the same as in the turbulent channel flows under the boundary layer approximation that the derivative of the streamwise mean velocity U in the streamwise direction x is much smaller than that in the wall-normal direction y and thus can be neglected, i.e.,

$$\nu U_i\frac{\partial^2U_i}{\partial x_k\partial x_k}=\nu\frac{\partial^2\left(\frac{1}{2}U_iU_i\right)}{\partial x_k\partial x_k}-\nu\frac{\partial U_i}{\partial x_k}\frac{\partial U_i}{\partial x_k}=\nu\frac{\partial^2}{\partial y^2}\left(\frac{1}{2}U^2\right)-\nu\frac{\partial U}{\partial y}\frac{\partial U}{\partial y}, \tag{3.15}$$

$$U_i\frac{\partial\tau_{ik}^R}{\partial x_k}=-U\frac{\partial\left\langle uv\right\rangle}{\partial y}. \tag{3.16}$$

Then, to within the boundary layer approximations, the transport equation for the mean kinetic energy of the 2D steady and zero-pressure gradient turbulent boundary layer is

given by

$$U\frac{\partial}{\partial x}\left(\frac{1}{2}U^2\right)+V\frac{\partial}{\partial y}\left(\frac{1}{2}U^2\right)=\nu\frac{\partial^2}{\partial y^2}\left(\frac{1}{2}U^2\right)-\nu\frac{\partial U}{\partial y}\frac{\partial U}{\partial y}-U\frac{\partial\left\langle uv\right\rangle}{\partial y}. \tag{3.17}$$

Under the same inner-normalization with $V^+ = V/u_\tau$, the inner-normalized equation for the mean kinetic energy in the zero-pressure gradient turbulent boundary layer is thus given by

$$\frac{\partial^2}{\partial y^{+2}}\left(\frac{1}{2}U^{+2}\right)+U^+\frac{\partial T^+}{\partial y^+}-\frac{\partial U^+}{\partial y^+}\frac{\partial U^+}{\partial y^+}+\left[-U^+\frac{\partial}{\partial x^+}\left(\frac{1}{2}U^{+2}\right)-V^+\frac{\partial}{\partial y^+}\left(\frac{1}{2}U^{+2}\right)\right]=0. \tag{3.18}$$

The four physical terms in Eq. (3.18) are respectively denoted as mean viscous diffusion (MVD), rate of work by net Reynolds stress (WRS), mean dissipation (MD), and mean advection (MA).

3.2.1.3 Balance in Mean Kinetic Energy Budgets

As described in the Introduction, the mean momentum equation has a four-layer structure that is revealed by considering the ratio of the viscous force term, $VF = \partial^2 U^+/\partial y^{+2}$, to the turbulent inertia term, $TI = -\partial\left\langle u^+v^+\right\rangle/\partial y^+$, as a function of wall-normal position. The same methodology is now utilized to explore the leading order terms in Eqs. (3.11) and (3.18). In this case the ratio of the sum of the mean viscous diffusion and mean dissipation terms ($MVD + MD$) to the rate of work by net Reynolds stress term (WRS) is

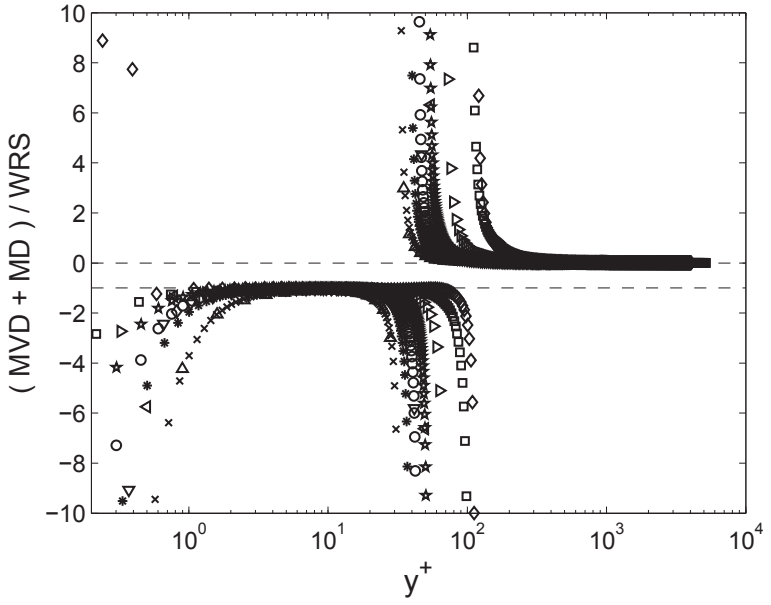

FIGURE 3.1: Ratio of the sum of mean viscous diffusion and mean dissipation terms (MVD+MD) to the rate of work by net Reynolds stress term WRS for fully developed channel/pipe flows, channel DNS data are from Hoyas and Jiménez (2008) :$\triangle, \delta^+ = 186$; $\bigtriangledown, \delta^+ = 547$; $\lhd, \delta^+ = 934$; $\rhd, \delta^+ = 2003$; Bernardini et al. (2014) : $\Diamond, \delta^+ = 4079$; Lee and Moser (2015) : $\square, \delta^+ = 5186$. Pipe DNS data are from: El Khoury et al. (2013) :$\times, \delta^+ = 181$; $\ast$, $\delta^+ = 361$; $\circ, \delta^+ = 550$; $\star$, $\delta^+ = 999$.

under consideration. This ratio profile is shown in Fig. 3.1 and Fig. 3.2 for channels/pipes and boundary layers, respectively.

Here it is noted that these profiles are identical to those of VF/TI. This observation is analytically verified by noting that the MVD term can be written as

$$\frac{\partial^2}{\partial y^{+2}}\left(\frac{1}{2}U^{+2}\right) = U^+\frac{\partial^2 U^+}{\partial y^{+2}} + \frac{\partial U^+}{\partial y^+}\frac{\partial U^+}{\partial y^+}, \tag{3.19}$$

which allows the mean kinetic energy equation to be written as

$$U^+\left(\frac{d^2U^+}{dy^{+2}} + \frac{dT^+}{dy^+} + \frac{1}{\delta^+}\right) = 0, \tag{3.20}$$

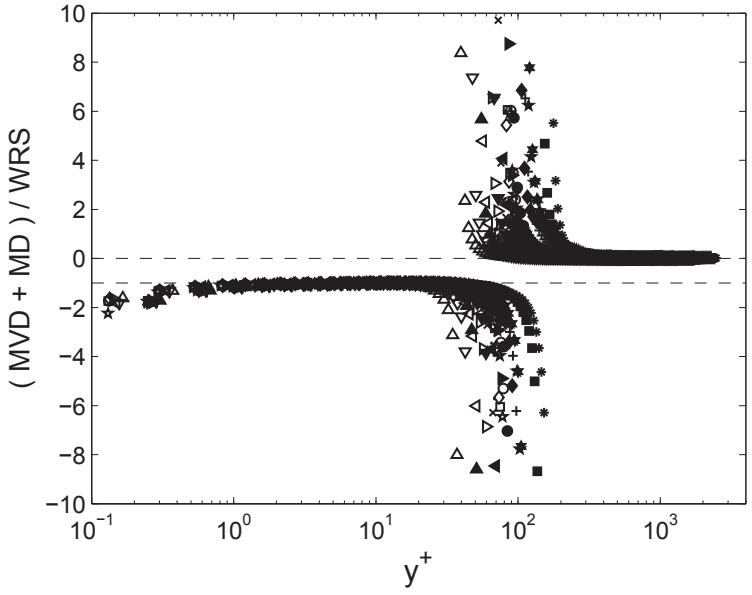

FIGURE 3.2: Ratio of the sum of mean viscous diffusion and mean dissipation terms (MVD+MD) to the rate of work by net Reynolds stress term WRS for Zero pressure gradient turbulent boundary layers, DNS and LES data are from Eitel-Amor et al. (2014) : $\triangle, \delta^+ = 252$; $\triangledown, \delta^+ = 359$; $\blacktriangle, \delta^+ = 458$; $\triangleleft, \delta^+ = 492$; $\triangleright, \delta^+ = 671$; $\blacktriangledown, \delta^+ = 725$; $\times, \delta^+ = 830$; $\blacktriangleleft, \delta^+ = 957$; $\cdot, \delta^+ = 974$; $\Diamond, \delta^+ = 1043$; $\circ, \delta^+ = 1145$; $\blacktriangleright, \delta^+ = 1169$; $\square, \delta^+ = 1244$; $\star, \delta^+ = 1271$; $\bullet, \delta^+ = 1367$; $+, \delta^+ = 1561$; $\blacklozenge, \delta^+ = 1751$; $\bigstar, \delta^+ = 1937$; $\blacksquare, \delta^+ = 2118$; $\bigstar, \delta^+ = 2299$; $\ast, \delta^+ = 2479$.

for channel/pipe flows or

$$U^+ \left(\frac{\partial^2 U^+}{\partial y^{+2}} + \frac{\partial T^+}{\partial y^+} - U^+ \frac{\partial U^+}{\partial x^+} - V^+ \frac{\partial U^+}{\partial y^+} \right) = 0, \tag{3.21}$$

for the boundary layer. The mean kinetic energy transport equation is therefore seen to exhibit the same layer structure as the mean momentum equation.

3.2.2 Turbulence Kinetic Energy Budgets

The budget equation for the component $\langle u_i u_j \rangle$ of the Reynolds stress tensor is written as

$$\begin{aligned} \frac{\partial}{\partial t}\left[\langle u_i u_j \rangle\right] + U_k \frac{\partial}{\partial x_k}\left[\langle u_i u_j \rangle\right] &= -\frac{\partial}{\partial x_k}\left[\langle u_i u_j u_k \rangle - \nu \frac{\partial}{\partial x_k}\langle u_i u_j \rangle\right] - \left[\langle u_i u_j \rangle \frac{\partial U_j}{\partial x_k} + \langle u_j u_k \rangle \frac{\partial U_i}{\partial x_k}\right] \\ &\quad -\frac{1}{\rho}\left[\left\langle u_i \frac{\partial p}{\partial x_j} + u_j \frac{\partial p}{\partial x_i} \right\rangle\right] - 2\nu \left\langle \frac{\partial u_i}{\partial x_k}\frac{\partial u_j}{\partial x_k} \right\rangle . \end{aligned} \tag{3.22}$$

Setting $j = i$ in the above equation, and multiplying by $1/2$ gives

$$\begin{aligned} \frac{\partial}{\partial t}\left[\frac{1}{2}\langle u_i u_i \rangle\right] + U_k \frac{\partial}{\partial x_k}\left[\frac{1}{2}\langle u_i u_i \rangle\right] &= -\frac{\partial}{\partial x_k}\left[\left\langle u_k \frac{1}{2} u_i u_i \right\rangle + \frac{1}{\rho}\langle u_k p \rangle\right] + \nu \frac{\partial^2}{\partial x_k \partial x_k}\left[\frac{1}{2}\langle u_i u_i \rangle\right] \\ &\quad - \langle u_i u_k \rangle \frac{\partial U_i}{\partial x_k} - \nu \left\langle \frac{\partial u_i}{\partial x_k}\frac{\partial u_i}{\partial x_k} \right\rangle . \end{aligned} \tag{3.23}$$

This equation is regarded as the evolution equation for turbulence kinetic energy (tKE), $K = 1/2\,\langle u_i u_i \rangle$.

3.2.2.1 Fully Developed Turbulent Channel and Pipe Flows

For statistically stationary flow

$$\frac{\partial}{\partial t}\left[\frac{1}{2}\langle u_i u_i \rangle\right] = 0. \tag{3.24}$$

Combination of $V = W = 0$ and the fully developed flow condition means that there is zero net advection of the TKE$= 1/2 \langle u_i u_i \rangle$, i.e.,

$$U_k \frac{\partial}{\partial x_k} \left[\frac{1}{2} \langle u_i u_i \rangle \right] = 0. \tag{3.25}$$

Furthermore,

$$- \frac{\partial}{\partial x_k} \left\langle u_k \frac{1}{2} u_i u_i \right\rangle = \underbrace{- \frac{\partial}{\partial x} \left\langle u \frac{1}{2} u_i u_i \right\rangle}_{\frac{\partial}{\partial x}=0} - \frac{\partial}{\partial y} \left\langle v \frac{1}{2} u_i u_i \right\rangle = - \frac{d}{dy} \left\langle v \frac{1}{2} u_i u_i \right\rangle, \tag{3.26}$$

$$- \frac{\partial}{\partial x_k} \frac{1}{\rho} \langle u_k p \rangle = \underbrace{- \frac{\partial}{\partial x} \frac{1}{\rho} \langle up \rangle}_{\frac{\partial}{\partial x}=0} - \frac{\partial}{\partial y} \frac{1}{\rho} \langle vp \rangle = - \frac{d}{dy} \frac{1}{\rho} \langle vp \rangle, \tag{3.27}$$

$$\nu \frac{\partial^2}{\partial x_k \partial x_k} \left[\frac{1}{2} \langle u_i u_i \rangle \right] = \underbrace{\nu \frac{\partial^2}{\partial x^2} \left[\frac{1}{2} \langle u_i u_i \rangle \right]}_{\frac{\partial}{\partial x}=0} + \nu \frac{\partial^2}{\partial y^2} \left[\frac{1}{2} \langle u_i u_i \rangle \right] = \nu \frac{d^2}{dy^2} \left[\frac{1}{2} \langle u_i u_i \rangle \right], \tag{3.28}$$

$$- \langle u_i u_k \rangle \frac{\partial U_i}{\partial x_k} = - \langle uv \rangle \frac{dU}{dy}, \tag{3.29}$$

and

$$- \nu \left\langle \frac{\partial u_i}{\partial x_k} \frac{\partial u_i}{\partial x_k} \right\rangle = d. \tag{3.30}$$

the budget equation for the turbulence kinetic energy in fully developed channel/pipe flow is given by

$$- \frac{d}{dy} \left\langle v \frac{1}{2} u_i u_i \right\rangle - \frac{d}{dy} \frac{1}{\rho} \langle vp \rangle + \nu \frac{d^2}{dy^2} \left[\frac{1}{2} \langle u_i u_i \rangle \right] - \langle uv \rangle \frac{dU}{dy} + d = 0. \tag{3.31}$$

All terms in Eq. (3.31) are now normalized by inner variables, u_τ and ν. but with

$$p^+ = \frac{\delta p}{\rho u_\tau \nu}. \tag{3.32}$$

Here, the pressure fluctuation is normalized with $\rho u_\tau \nu/\delta$ rather than by ρu_τ^2. This follows from the analogous scaling of the mean pressure gradient in terms of the friction velocity and the half-channel height. Physically, this seems appropriate because the fluctuating pressure is a non-local quantity, with the pressure at a point found by integrating over the domain. The analysis of Appendix A empirically evidences that the use of this normalization does not alter conclusions regarding the resulting layer structure.

With $K^+ = 1/2 \left\langle u_i^+ u_i^+ \right\rangle$, $T^+ = -\left\langle u^+ v^+ \right\rangle$, and by collecting terms, the inner-normalized budget equation for the turbulence kinetic energy in channel flow becomes

$$\frac{d^2}{dy^{+2}}\left(K^+\right) \quad + \left[T^+ \frac{dU^+}{dy^+} - \frac{d}{dy^+}\left\langle v^+ K^+ \right\rangle\right] + d^+ + \frac{1}{\delta^+}\left[-\frac{d}{dy^+}\left\langle p^+ v^+ \right\rangle\right] = 0. \tag{3.33}$$

Four grouped terms in Eq. (3.33) are referred to as turbulent viscous diffusion (TVD), production/turbulent diffusion (PTD), turbulent dissipation (TD) and turbulent pressure diffusion (TPD). The inner-normalized form of the turbulence kinetic energy budget for fully developed turbulent pipe flow has a form that is identical to that for channel flow when expressed in terms of the wall-normal variable, $y^+ = \delta^+ - r^+$.

3.2.2.2 Zero-Pressure Gradient Turbulent Boundary Layer

For statistically stationary flow

$$\frac{\partial}{\partial t}\left[\frac{1}{2}\left\langle u_i u_i\right\rangle\right] = 0. \tag{3.34}$$

It is similar to the mean kinetic energy transport equation, the advection of the tKE turns into

$$U_k \frac{\partial}{\partial x_k}\left[\frac{1}{2}\left\langle u_i u_i\right\rangle\right] = U\frac{\partial}{\partial x}\left[\frac{1}{2}\left\langle u_i u_i\right\rangle\right] + V\frac{\partial}{\partial y}\left[\frac{1}{2}\left\langle u_i u_i\right\rangle\right]. \tag{3.35}$$

Furthermore, the derivatives in the streamwise direction in all the remaining terms are zero under the boundary layer approximations and then they all take on the same forms as the turbulent channel flows, i.e.,

$$-\frac{\partial}{\partial x_k}\left\langle u_k \frac{1}{2} u_i u_i\right\rangle = \underbrace{-\frac{\partial}{\partial x}\left\langle u \frac{1}{2} u_i u_i\right\rangle}_{\frac{\partial}{\partial x}=0} - \frac{\partial}{\partial y}\left\langle v \frac{1}{2} u_i u_i\right\rangle = -\frac{\partial}{\partial y}\left\langle v \frac{1}{2} u_i u_i\right\rangle, \tag{3.36}$$

$$-\frac{\partial}{\partial x_k}\frac{1}{\rho}\left\langle u_k p\right\rangle = \underbrace{-\frac{\partial}{\partial x}\frac{1}{\rho}\left\langle up\right\rangle}_{\frac{\partial}{\partial x}=0} - \frac{\partial}{\partial y}\frac{1}{\rho}\left\langle vp\right\rangle = -\frac{\partial}{\partial y}\frac{1}{\rho}\left\langle vp\right\rangle, \tag{3.37}$$

$$\nu\frac{\partial^2}{\partial x_k \partial x_k}\left[\frac{1}{2}\left\langle u_i u_i\right\rangle\right] = \underbrace{\nu\frac{\partial^2}{\partial x^2}\left[\frac{1}{2}\left\langle u_i u_i\right\rangle\right]}_{\frac{\partial}{\partial x}=0} + \nu\frac{\partial^2}{\partial y^2}\left[\frac{1}{2}\left\langle u_i u_i\right\rangle\right] = \nu\frac{\partial^2}{\partial y^2}\left[\frac{1}{2}\left\langle u_i u_i\right\rangle\right], \tag{3.38}$$

$$-\left\langle u_i u_k\right\rangle \frac{\partial U_i}{\partial x_k} = -\left\langle uv\right\rangle \frac{\partial U}{\partial y}, \tag{3.39}$$

and

$$-\nu\left\langle\frac{\partial u_i}{\partial x_k}\frac{\partial u_i}{\partial x_k}\right\rangle = d. \tag{3.40}$$

Therefore, the leading order transport equation for the turbulent kinetic energy of the 2D steady and zero-pressure gradient turbulent boundary layer is given by

$$\begin{aligned} U\frac{\partial}{\partial x}\left[\frac{1}{2}\langle u_i u_i\rangle\right] \quad & +V\frac{\partial}{\partial y}\left[\frac{1}{2}\langle u_i u_i\rangle\right] = -\frac{\partial}{\partial y}\left\langle v\frac{1}{2}u_i u_i\right\rangle - \frac{\partial}{\partial y}\frac{1}{\rho}\langle vp\rangle \\ & +\nu\frac{\partial^2}{\partial y^2}\left[\frac{1}{2}\langle u_i u_i\rangle\right] - \langle uv\rangle\frac{\partial U}{\partial y} + d. \end{aligned} \tag{3.41}$$

The same inner variables are used to normalize Eq. (3.41), and the inner-normalized equation for the turbulent boundary layer then becomes

$$\begin{aligned} & \frac{\partial^2}{\partial y^{+2}}\left(K^+\right) + \left[T^+\frac{\partial U^+}{\partial y^+} - \frac{\partial}{\partial y^+}\left\langle v^+K^+\right\rangle\right] + d^+ + \\ & \left[-U^+\frac{\partial}{\partial x^+}K^+ - V^+\frac{\partial}{\partial y^+}K^+ - \frac{1}{\delta^+}\frac{\partial}{\partial y^+}\left\langle p^+v^+\right\rangle\right] = 0. \end{aligned} \tag{3.42}$$

The first three grouped terms in Eq. (3.42) are the same as in Eq. (3.33). The fourth one is referred to as turbulent advection/pressure diffusion (TAPD).

The leading balances for the turbulence kinetic energy (Eqs. (3.33) and (3.42)) are considered, as these are useful for understanding the total budget structure. Here the results of the mean kinetic energy balance motivate examining the ratio of the sum of turbulent viscous diffusion and turbulent dissipation terms (TVD + TD) to the production/turbulent diffusion term (PTD). Because the pipe flow results are essentially indistinguishable from the channel results, Fig. 3.3 and Fig. 3.4 show these ratio profiles

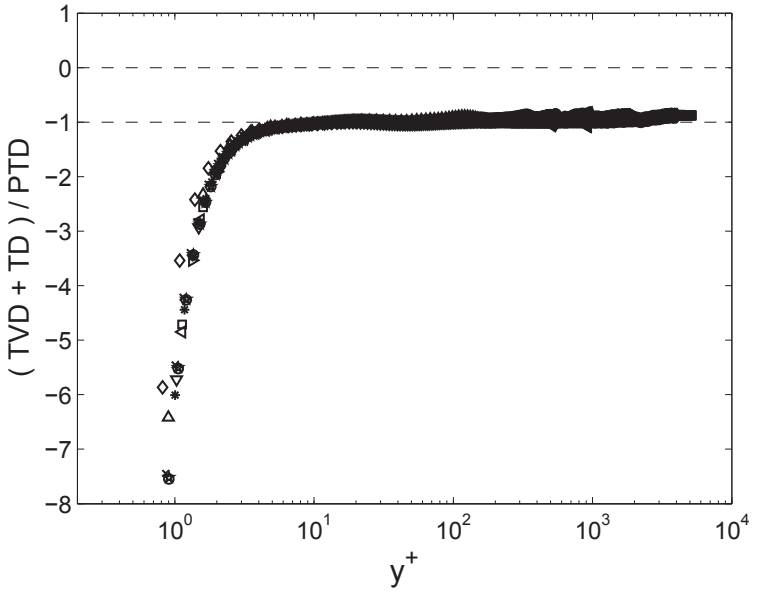

FIGURE 3.3: Ratio of the sum of turbulent viscous diffusion and turbulent dissipation terms (MVD + MD) to the production/turbulent diffusion term (PTD) for channel/pipe flows. Symbols are the same as in Fig. 3.1.

for the channel/pipe and boundary layer. In contrast to the ratio profiles of the mean kinetic energy terms in Fig. 3.1 and Fig. 3.2, there is no apparent change of balance indicated in Fig. 3.3 and Fig. 3.4. The profile curves start from large negative values near the wall. Here Eqs. 3.33 and 3.42 indicate that the diffusion of TKE identically balances turbulent dissipation at the wall, and thus to leading order a small distance from the wall. Beyond this region, the ratio closely approximates -1. Detailed examination (not shown) indicates that this balance is comprised of one of the PTD terms and the TVD and TD terms. Along the -1 dashed line, the TVD term gradually gets closer to 0, which results in the change in balance from three terms to two terms; namely the TD and PTD terms. This two-term balance is continuously sustained throughout the remainder of the channel. Unlike the channel, the boundary layer profiles deviate from -1 and approach zero as $y \to \delta$. In this region, the TAPD term increases in relative importance and forms

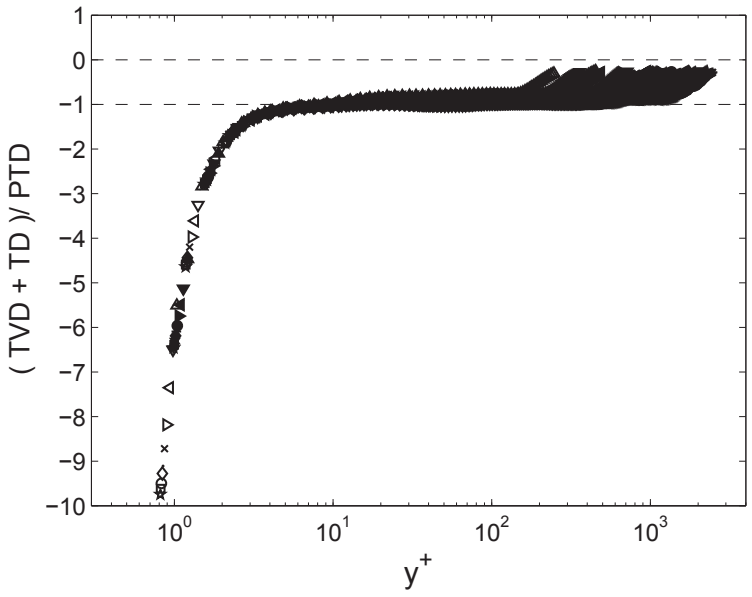

FIGURE 3.4: Ratio of the sum of turbulent viscous diffusion and turbulent dissipation terms (MVD + MD) to the production/turbulent diffusion term (PTD) for boundary layer. Symbols are the same as in Fig. 3.2.

a new balance with the TD and PTD terms. Thus, the turbulence kinetic energy budget exhibits three layers but four distinct balances in the boundary layer.

3.2.3 Total Kinetic Energy Budgets

The combination of Eq. (3.11) and Eq. (3.33) gives rise to the inner-normalized budget equation for the total kinetic energy in channel/pipe flow

$$\frac{d^2}{dy^{+2}}\left(\frac{1}{2}U^{+2}+K^{+}\right)+\frac{d}{dy^{+}}\left[U^{+}T^{+}-\left\langle v^{+}K^{+}\right\rangle\right]+D^{+}+\frac{1}{\delta^{+}}\left[U^{+}-\frac{d}{dy^{+}}\left\langle p^{+}v^{+}\right\rangle\right]=0, \tag{3.43}$$

where $D^+ = -\left[d^+ + (\partial U^+/\partial y^+)^2\right]$. Four physical mechanisms are present in Eq. (3.43). These are viscous diffusion (VD), production/turbulent diffusion (PT), dissipation (D) and total pressure diffusion (PD).

The combination of Eq. (3.18) and Eq. (3.42) gives rise to the inner-normalized budget equation for the total kinetic energy in the boundary layer,

$$\frac{\partial^2}{\partial y^{+2}}\left(\frac{1}{2}U^{+2}+K^+\right)+\frac{\partial}{\partial y^+}\left[U^+T^+-\left\langle v^+K^+\right\rangle\right]+D^+ + \left[-U^+\frac{\partial}{\partial x^+}\left(\frac{1}{2}U^{+2}+K^+\right)-V^+\frac{\partial}{\partial y^+}\left(\frac{1}{2}U^{+2}+K^+\right)-\frac{1}{\delta^+}\frac{\partial}{\partial y^+}\left\langle p^+v^+\right\rangle\right]=0. \tag{3.44}$$

The different terms of Eq. (3.44) are referred to as viscous diffusion (VD), production/turbulent diffusion (PT), dissipation (D) and advection/turbulent pressure diffusion (APD).

3.2.4 Terms in Total Kinetic Energy Budgets

Analysis begins by individually considering the behaviors of the four grouped terms in Eqs. (3.43) and (3.44). Figs. 3.5 (a)-(l) show profiles of the terms. The first three terms for the channel, pipe, and boundary layer exhibit nearly the same behavior. The profiles of the VD and D terms convincingly merge for all Reynolds numbers plotted, except immediately adjacent to the wall in the channel and pipe. Here the VD term appears to consistently increase with Reynolds number below $y^+ \simeq 3$, and the D term decreases with Reynolds number below $y^+ \simeq 7$. Hoyas and Jiménez (2008) attribute these

behaviors to the effect of the large scale inactive motions that exist in the logarithmic layer. Existing evidence indicates that this is a weak but persistent Reynolds number dependence (Klewicki, 2010). The VD term has a value of about 1.2 close to the wall. Starting near $y^+ = 2$ this profile decreases rapidly and crosses zero at $y^+ \simeq 7.5$ and 7.75 in the channel and pipe, respectively, and at $y^+ \simeq 7.3$ for the boundary layer. The VD profiles reach their minimum values near $y^+ = 15$, but increase thereafter to approach zero from below. Opposite to the VD term, the D term begins at a value of about -1.2 close to the wall but increases more gradually as it approaches zero from below. The VD and D terms identically balance at the wall.

The PT term profiles in Figs. 3.5 start with a zero value at the wall, and rapidly ascend. The peaks in all the profiles attain values of about 0.70 near $y^+ = 9.0$. Beyond the peak, the PT term descends to cross zero from positive to negative. The negative portion of this profile is concave-upward, and this characteristic is more evident for the boundary layer. The position of the zero-crossing in the PT term moves to greater y^+ values with increasing δ^+.

The PD and APD terms in Figs. 3.5 (g) and (h) are both zero at the wall, and become larger with increasing distance from the wall. The maximum values of these profiles are Reynolds number dependent. Moreover, there is an obvious peak in the APD profile, and this term decreases towards zero in the outer region. This is qualitatively distinct from the PD profiles in the channel and pipe, which exhibit highly similar profile shapes, but small quantitative differences. In the overall balance, the behavior of the APD profile has been verified to compensate for the concave-upward trend of the PT term near the edge

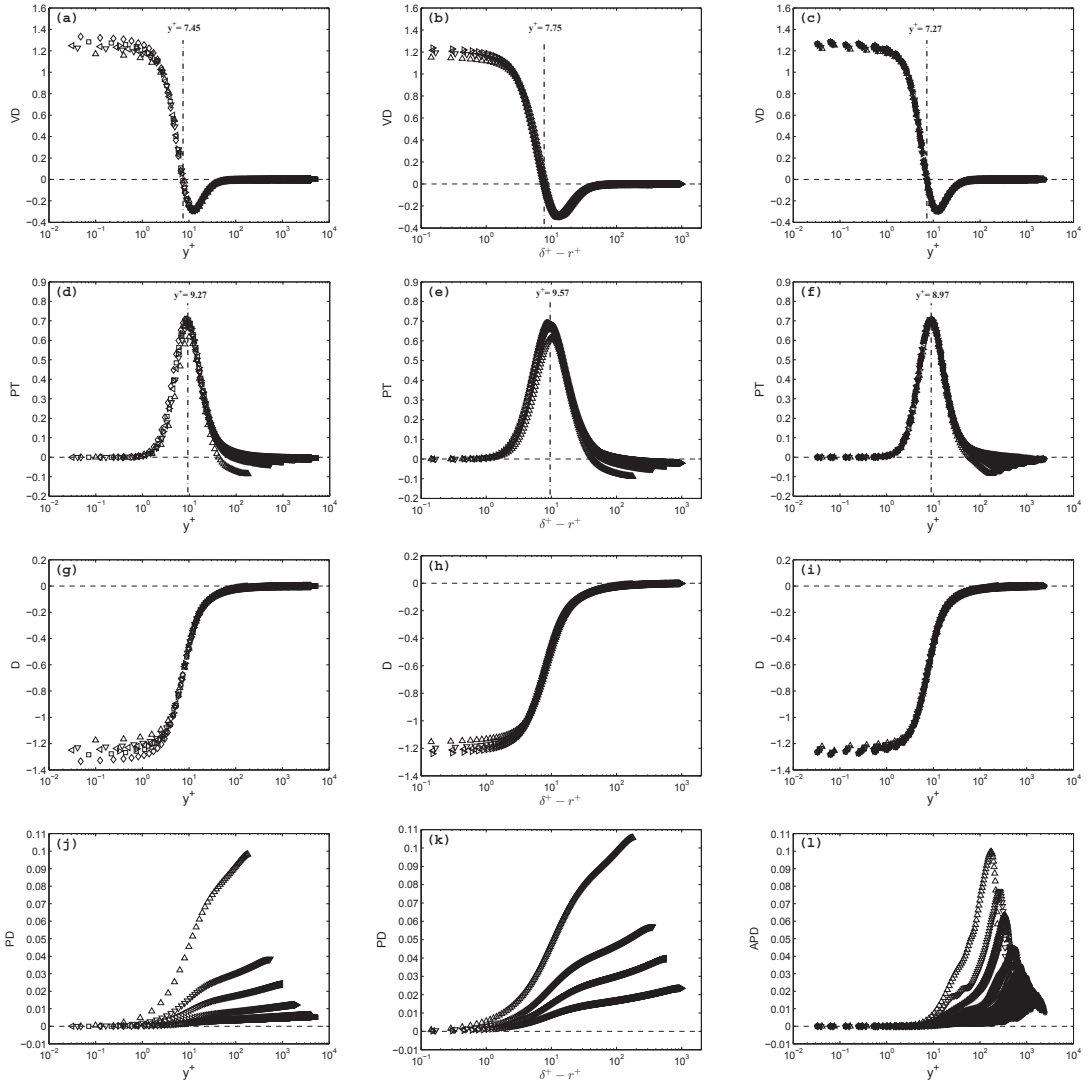

FIGURE 3.5: Profiles of the individual terms in the total kinetic energy transport equation. Panels (a), (d), (g) and (j) respectively represent the VD, PT, D, and PD terms for turbulent channel flow, (b), (e), (h), (k) respectively represent the VD, PT, D, and PD terms for turbulent pipe flows, and (c), (f), (i) and (l) respectively represent the VD, PT, D and APD terms for turbulent boundary layer flows. The vertical dashed-dotted line in (a) - (c) denotes the wall-normal position where the VD crosses zero from positive to negative. The vertical dashed-dotted line in (d) - (f) denotes the wall-normal position where the PTD achieves its maximal value.

of the boundary layer. In the region near the wall, the PD term in the channel and pipe and the APD term in the boundary layer are much smaller than the other three terms, but both rise to leading order in the outer region.

3.3 Structure of Total Kinetic Energy Balance

3.3.1 Balance Ratios of Grouped Terms

The analysis of section 3.2.1 reveals a mean kinetic energy layer structure that is the same as for the mean momentum balance. This finding motivates examining the analogous ratio in the total kinetic energy equation: the ratio of the sum of the viscous diffusion and the dissipation terms (VD+D) to the production/turbulent diffusion term (PT). Here it is noted that if the ratio is

$$|(VD + D)/PT| \ll 1, \tag{3.45}$$

then both the VD and D terms are small, and the PT and the PD terms are nominally in balance. If

$$|(VD + D)/PT| \cong 1, \tag{3.46}$$

their effects are in balance, and the PD term is either of the same order of magnitude or much smaller. Else, if

$$|(VD + D)/PT| \gg 1, \tag{3.47}$$

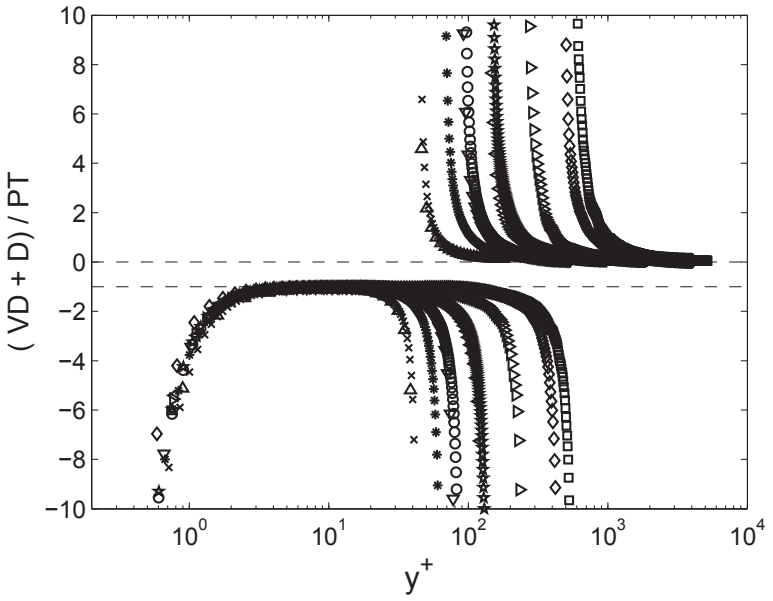

FIGURE 3.6: Ratio of the sum of the viscous diffusion (VD) and the dissipation (D) terms to the production/turbulent diffusion (PT) term versus y^+ for channel and pipe flows. Symbols are the same as in Fig. 3.1.

the PT term is very small, and either the VD term is balanced with the D term or the PD term is of the same order of magnitude as these two terms.

Fig. 3.6 and Fig. 3.7 show (VD+D)/PT for the channel/pipe and boundary layer, respectively, These data indicate a four-layer structure. This structure is, however, distinct from the layer structure identified by Wei et al. (2005a) for the mean momentum equation, which, as shown herein, also corresponds with the mean kinetic energy structure. To avoid confusion with the layers associated with the mean momentum equation, in what follows the layers evident in Fig. 3.6 and Fig. 3.7 are denoted with lower case i-iv. The analysis now proceeds by describing how the contributing terms in Eqs. (3.43) and (3.44) conspire to produce the layer structure evident in Fig. 3.5 and Fig. 3.6.

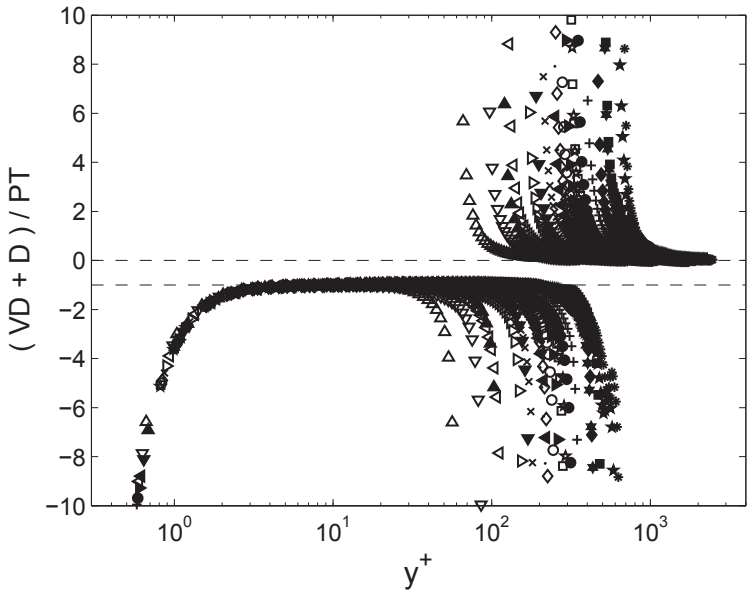

FIGURE 3.7: Ratio of the sum of the viscous diffusion (VD) and the dissipation (D) terms to the production/turbulent diffusion (PT) term versus y^+ for boundary layer flows. Symbols are the same as in Fig. 3.2.

3.3.2 Layers i and ii

Layer i lies very close to the wall, $y^+ \lesssim 1.5$. The ending value cited is based on the criterion that the ratio becomes less than -2 (Wei et al., 2005a). In this domain, the leading balance is between the viscous diffusion and dissipation term, as exemplified in Fig. 3.8 for the channel/pipe and Fig. 3.9 boundary layer. Here the ratio VD/D deviates from -1 by less than 4%. Outside this thin layer exists a region (layer ii) that is characterized by a nearly exact balance between the sum of the VD and D terms and the PT term. At the onset of this region the viscous diffusion term is positive, but with increasing y^+ goes to zero faster than the dissipation term. It subsequently crosses zero, reaches a minimum, and then asymptotes to zero. Beyond where the VD term crosses zero, its magnitude contribution to the sum of the VD and D terms increases gradually

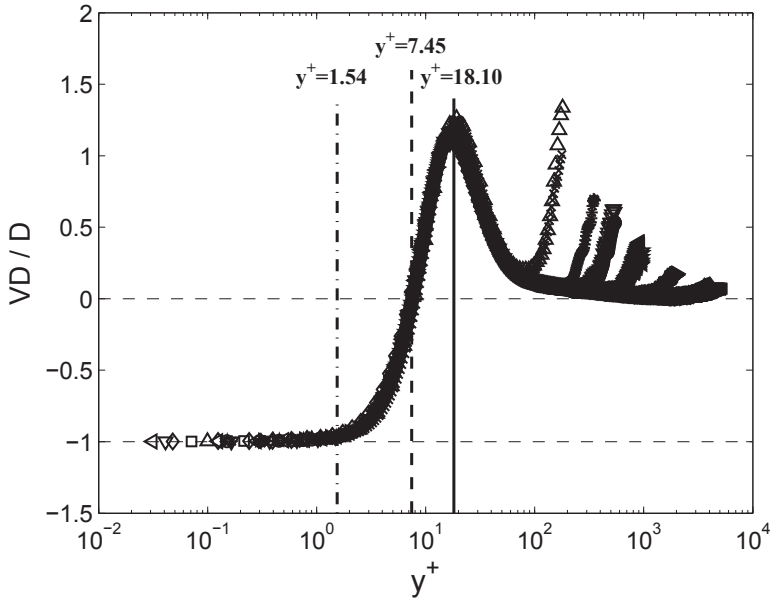

FIGURE 3.8: Ratio of viscous diffusion (VD) to dissipation (D) for Channel and pipe flows. The vertical dashed-dotted line denotes the external bound of layer i. The vertical dashed line denotes the position where the viscous diffusion crosses zero. The vertical solid line denotes the position where the ratio peaks. Symbols are the same as in Fig. 3.1.

and attains a maximum. This maximum is slightly greater than half the contribution to the sum (about 54%), and is located near $y^+ \simeq 18$.

For greater distances from the wall, but still within layer ii, the contribution from the VD term decreases and becomes negligible compared to the D term. This occurs near the outer edge of layer ii. Fig. 3.5 shows that near the start of layer ii, the PT term increases to balance the VD and D terms; achieving peak values of about 0.70 near $y^+ = 9.0$. The extent of layer ii exhibits a Reynolds number dependence, with its external boundary extending into the inertial/advection balance layer (layer IV) of the mean momentum equation.

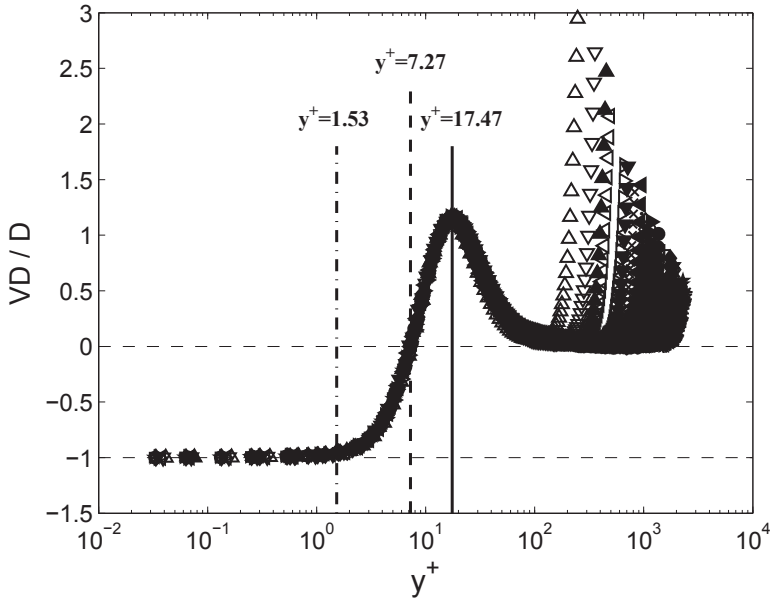

FIGURE 3.9: Ratio of viscous diffusion (VD) to dissipation (D) for boundary layers. The vertical dashed-dotted line denotes the external bound of layer i. The vertical dashed line denotes the position where the viscous diffusion crosses zero. The vertical solid line denotes the position where the ratio peaks. Symbols are the same as in Fig. 3.2.

3.3.3 External Bounds of Layers ii and iii

Per the criterion developed by Wei et al. (2005a), the start of layer iii is where (VD+D)/PT drops below -2. Consistently, the end of layer iii is where this ratio falls below 0.5. Fig. 3.10 and Fig. 3.11 show the normalized width of layer iii (Δy^+_{iii}) versus δ^+ for channel, pipe, and, boundary layer flows as determined by these criteria. Per the scaling analysis , Δy^+_{iii} is normalized by $(\delta^+ - \sqrt{\delta^+})$, as this is reasoned to constitute a finite Reynolds number correction to outer normalization. To within their scatter, the boundary layer data of Fig. 3.11 seem to remain constant over their entire Reynolds number range. Conversely, the channel data seem to decay toward a constant value with increasing δ^+. The pipe flow data show a similar trend as the channel data, but only extend to

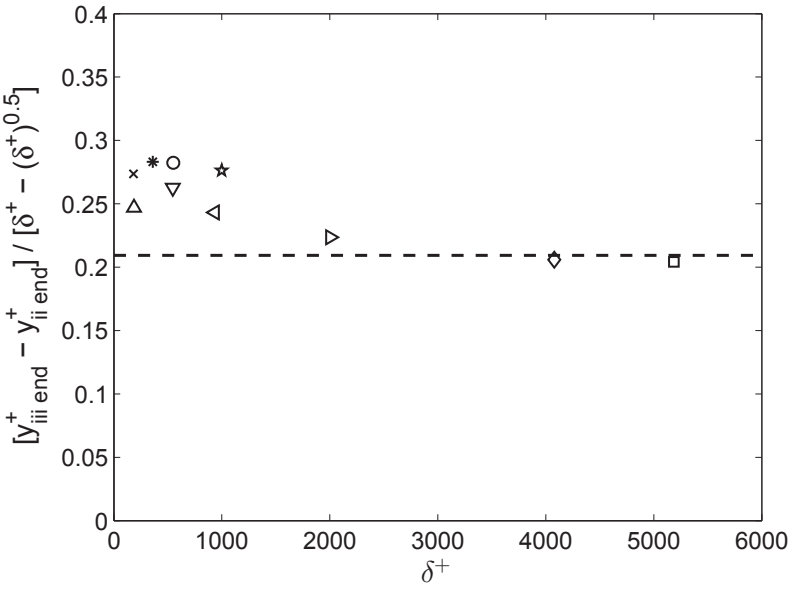

FIGURE 3.10: Width of layer iii normalized by $(\delta^+ - \sqrt{\delta^+})$ and plotted versus δ^+ for channel and pipe flows. Horizontal line is at 0.2093. Symbols are the same as in Fig. 3.1.

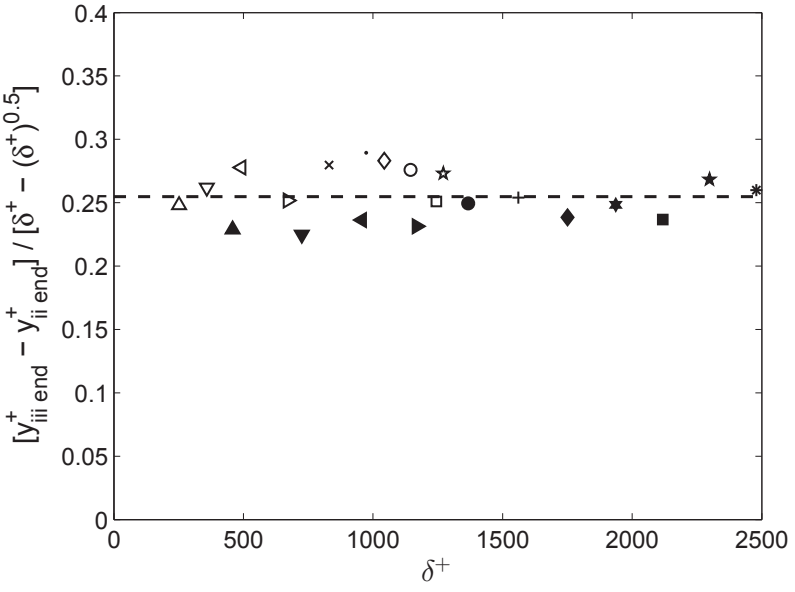

FIGURE 3.11: Width of layer iii normalized by $(\delta^+ - \sqrt{\delta^+})$ and plotted versus δ^+ for boundary layers. Horizontal line is at 0.2549. Symbols are the same as in Fig. 3.2.

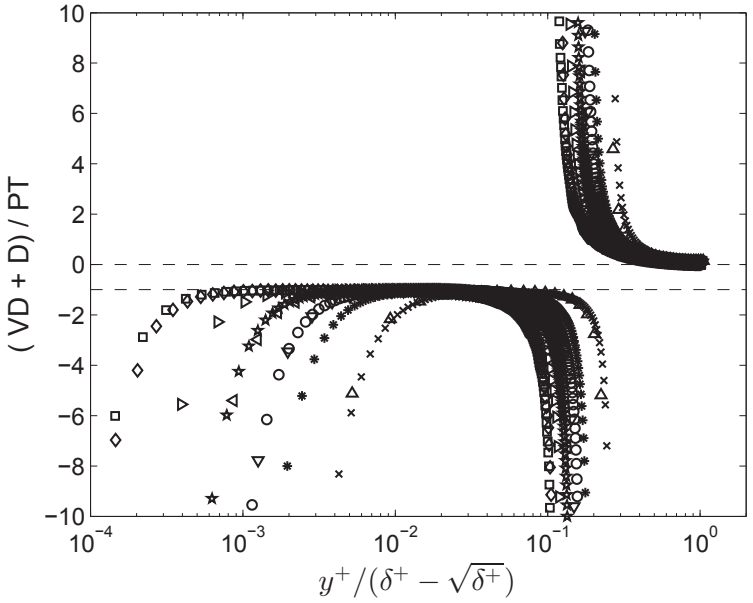

FIGURE 3.12: Profiles of Fig. 3.6 for channel/pipe plotted versus $y^+/(\delta^+ - \sqrt{\delta^+})$. Symbols are the same as in Fig. 3.1.

$\delta^+ \simeq 1000$.

While the analysis indicates that Δy^+_{iii} should scale with $(\delta^+ - \sqrt{\delta^+})$ at finite δ^+, this analysis does not require that the beginning and end points of layer iii individually adhere to this scaling. This rather subtle point is clarified in Fig. 3.12 and Fig. 3.13, which replots the data of Fig. 3.6 and Fig. 3.7 versus $y^+/(\delta^+ - \sqrt{\delta^+})$. The data of Fig. 3.13 suggest invariance under this normalization, and thus the end points of layers ii and iii in the boundary layer seem to scale with $(\delta^+ - \sqrt{\delta^+})$. On the other hand, examination of the channel and pipe data reveals that the end points of both layers ii and iii deviate from this scaling over the given δ^+ range. As exemplified in Fig. 3.12, both the channel data at $\delta^+ = 186$ and pipe data at $\delta^+ = 186$ show a considerable deviation from those at higher δ^+. With increasing δ^+, however, the profile-to-profile deviation diminishes. The deviation of the $\delta^+ = 186$ profile in Fig. 3.12 is not especially surprising, since this

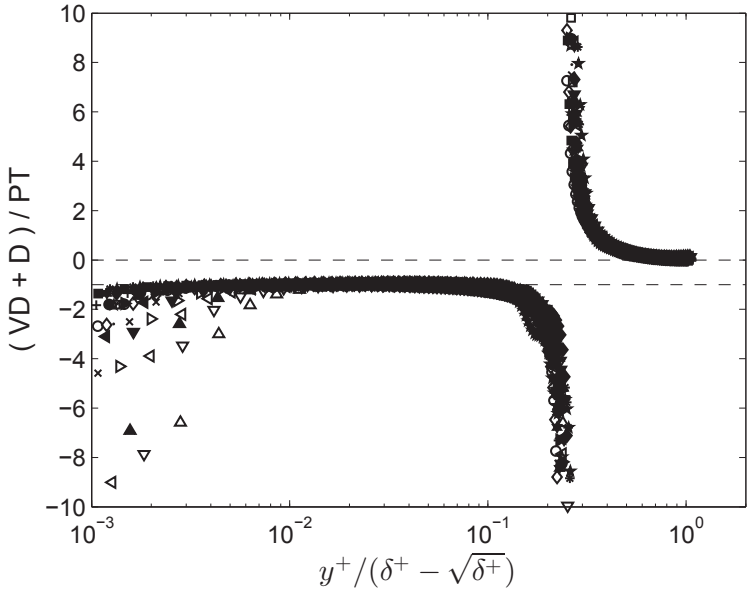

FIGURE 3.13: Profiles of Fig. 3.7 for boundary layer plotted versus $y^+/(\delta^+ - \sqrt{\delta^+})$ Symbols are the same as in Fig. 3.2.

profile is just barely within regime where the mean momentum equation exhibits its four layer structure (Elsnab et al., 2011). Additionally, it has been verified that both the channel and pipe profiles exhibit the same qualitative behavior when plotted versus y/δ. Determining whether the beginning and end points of layer iii for the channel and pipe eventually align under the normalization of Fig. 3.12 and Fig. 3.13 awaits higher Reynolds number data.

3.3.4 Layers iii and iv

Across layer iii there is an exchange in the balance of terms in the total kinetic energy budget equations. This exchange occurs around the location of maximum $[U^+T^+ - \langle v^+K^+\rangle]$.

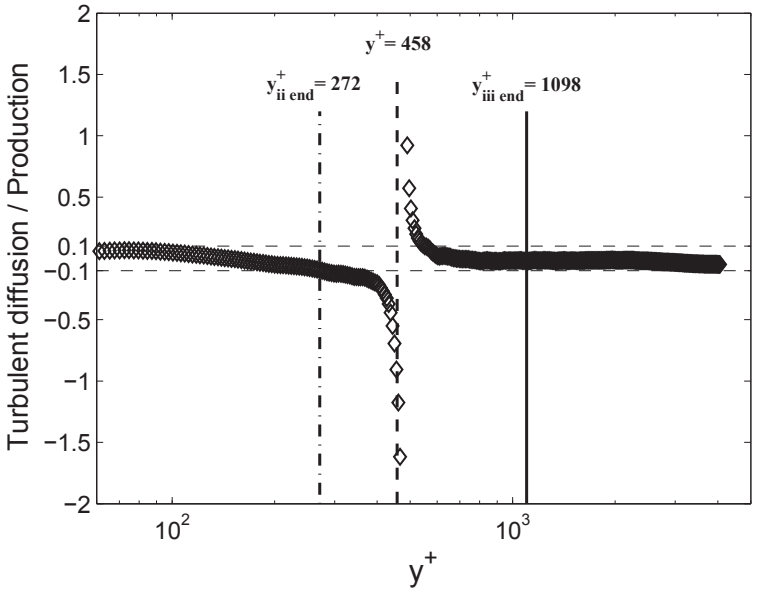

FIGURE 3.14: Ratio of turbulent diffusion to production for Channel flow at $\delta^+ = 4079$. The vertical dashed-dotted line denotes the external bound of layer ii. The vertical dashed line denotes where the PT term crosses zero. The vertical solid line denotes the external bound of layer iii.

In this region the dissipation (D) term and the total pressure diffusion (PD) term in channel/pipe flows (or the advection/turbulent pressure diffusion (APD) term in boundary layers) nearly balance. Before and beyond the peak in $[U^+T^+ - \langle v^+K^+\rangle]$, the PT term is in leading order balance with the sum of the D and PD terms in channel and pipe flows, and balances the D + APD terms in boundary layers. The VD term in this layer is less than a tenth of the D term. Thus, within layer iii, there are three terms of significant magnitude, with the VD term being much smaller.

Close examination also indicates that across layer iii the PT term changes its sign, and the contribution from turbulent diffusion is much smaller when compared to the contribution from the production term. This characteristic is reflected in the results of Fig. 3.14 and Fig. 3.15. Accordingly, the wall-normal position where the production term

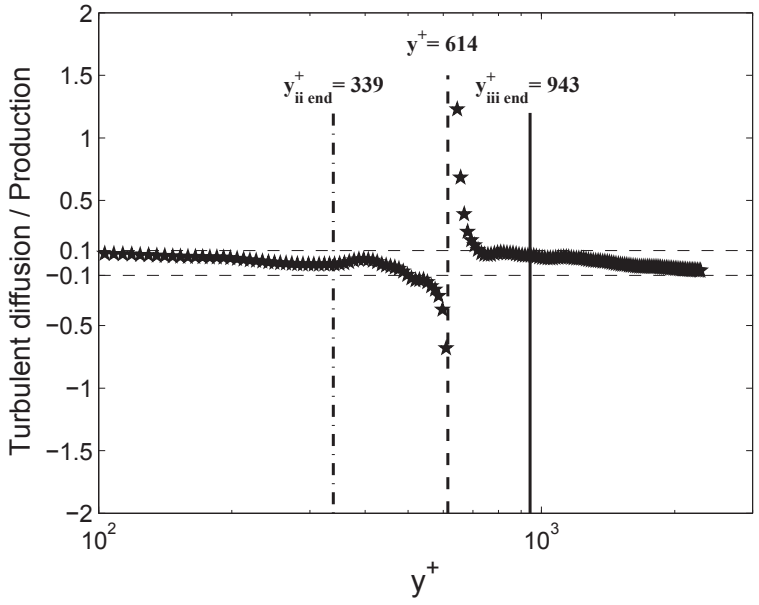

FIGURE 3.15: Ratio of turbulent diffusion to production for boundary layer at $\delta^+ = 2299$. The vertical dashed-dotted line denotes the external bound of layer ii. The vertical dashed line denotes where the PT term crosses zero. The vertical solid line denotes the external bound of layer iii.

crosses zero is very close to where the PT term crosses zero. These findings substantiate that the turbulent diffusion term over layer iii is quite small. Therefore, the turbulent diffusion term is small but non-negligible in layer ii, but attains negligible values in layer iii.

The dissipation term is dominated by its turbulence contribution in layer iii. This is demonstrated in Fig. 3.16 and Fig. 3.17, which show the ratios of the mean to turbulent dissipation. In these figures, the abscissa starts near the outer edge of layer ii at $\delta^+ = 180$ and 252 for the turbulent channels and boundary layers, respectively. Beyond the start of layer iii the mean dissipation is at least 10 times smaller than the turbulent dissipation, and its effect over layer iii diminishes with increasing δ^+. These findings are similar to previous observations that the fluctuating enstrophy dominates the mean enstrophy in

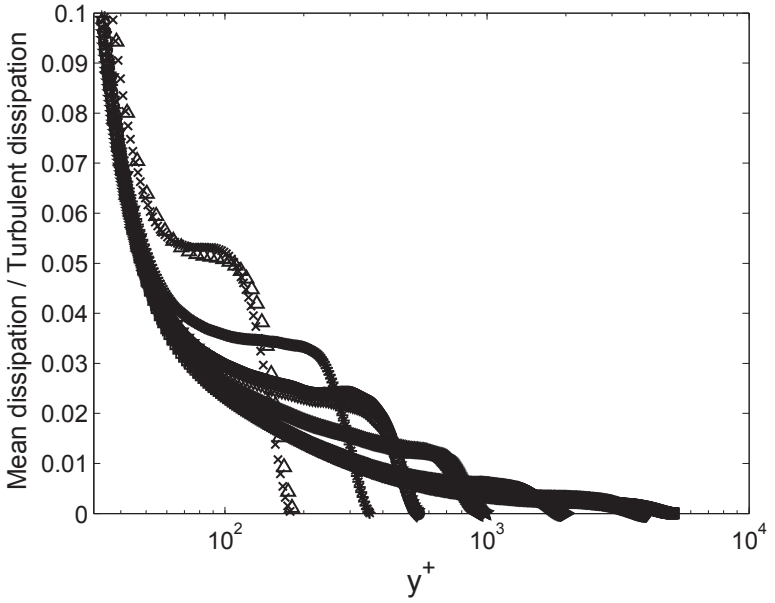

FIGURE 3.16: Ratio of the mean dissipation to the turbulent dissipation for channel and pipe flows. Symbols are the same as in Fig. 3.1.

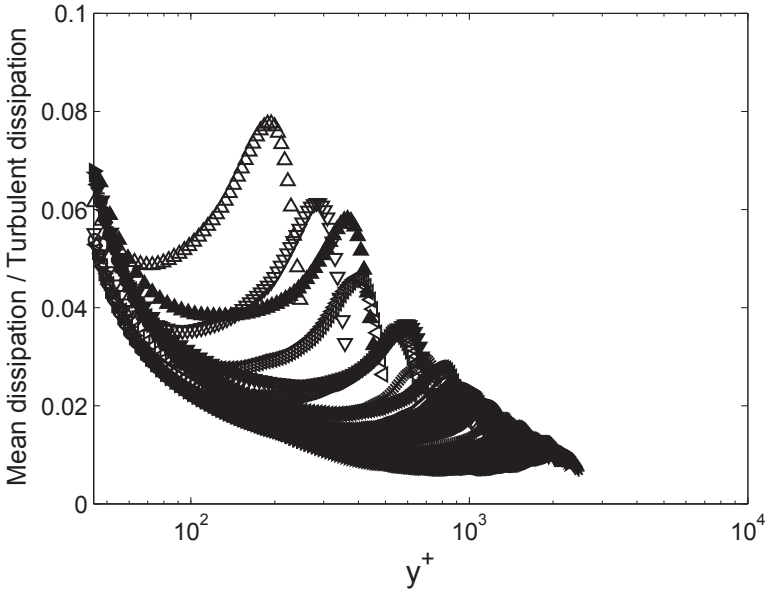

FIGURE 3.17: Ratio of the mean dissipation to the turbulent dissipation for boundary layers. Symbols are the same as in Fig. 3.2.

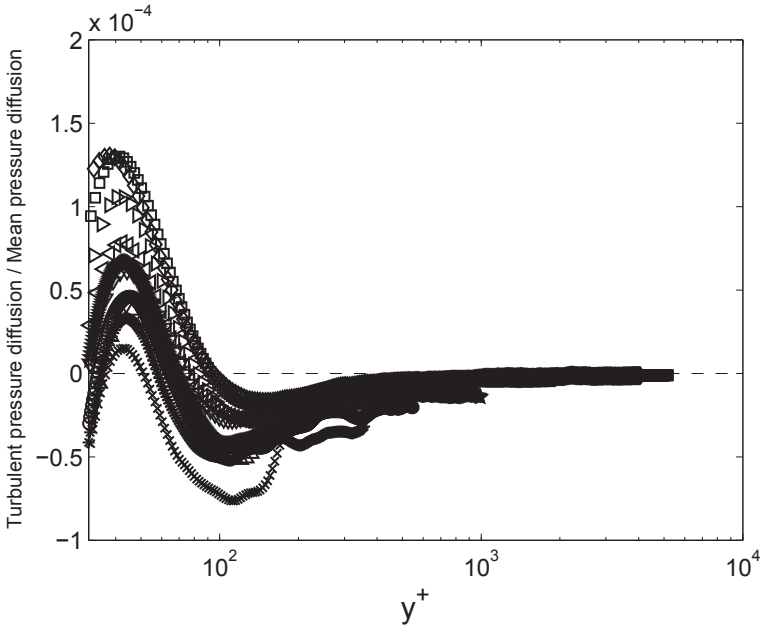

FIGURE 3.18: Ratio of turbulent pressure diffusion to mean pressure diffusion in channel and pipe flows. Symbols are the same as in Fig. 3.1.

layer IV of the mean momentum equation (Klewicki, 2013a).

The ratio of the turbulent pressure diffusion to the mean pressure diffusion is exemplified for the channel in Fig. 3.18, while the ratio of turbulent pressure diffusion to advection in the boundary layer is given in Fig. 3.19. The fact that these ratios are both less than 10^{-3} beyond layer ii indicates that the turbulent pressure diffusion is justifiably absent from the leading balance in layer iii. The layer iii balance in the channel/pipe therefore simplifies to

$$\frac{d}{dy^+}\left[U^+T^+\right] + d^+ + \epsilon^2 U^+ = 0, \tag{3.48}$$

where $\epsilon^2 = 1/\delta^+$, and for the boundary layer is

$$\frac{\partial}{\partial y^+}\left[U^+T^+\right] + d^+ + \left[-U^+\frac{\partial}{\partial x^+}\left(\frac{1}{2}U^{+2} + K^+\right) - V^+\frac{\partial}{\partial y^+}\left(\frac{1}{2}U^{+2} + K^+\right)\right] = 0. \tag{3.49}$$

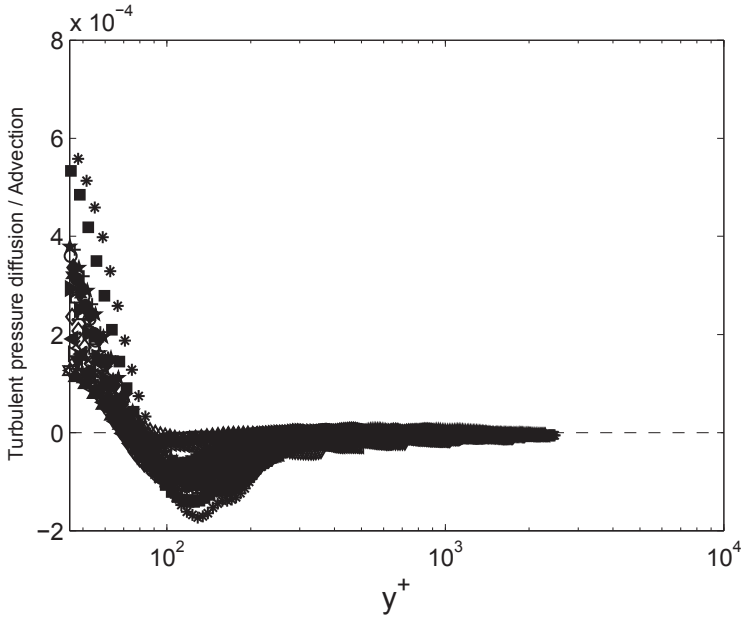

FIGURE 3.19: Ratio of turbulent pressure diffusion to advection in boundary layers. Symbols are the same as in Fig. 3.2.

Beyond layer iii, the magnitude of both the VD and D terms gradually become smaller than either the PT or PD terms in the channel/pipe flows, or the APD term in the boundary layer. Similarly, both the turbulent diffusion and the turbulent pressure diffusion are much smaller than their mean contributions. Thus, the balance is established between the production and mean pressure diffusion for channel/pipe flows

$$\frac{d}{dy^+}\left[U^+T^+\right] + \frac{1}{\delta^+}U^+ = 0, \tag{3.50}$$

and between the production and the advection for boundary layers, i.e.,

$$\frac{\partial}{\partial y^+}\left[U^+T^+\right] + \left[-U^+\frac{\partial}{\partial x^+}\left(\frac{1}{2}U^{+2} + K^+\right) - V^+\frac{\partial}{\partial y^+}\left(\frac{1}{2}U^{+2} + K^+\right)\right] = 0. \tag{3.51}$$

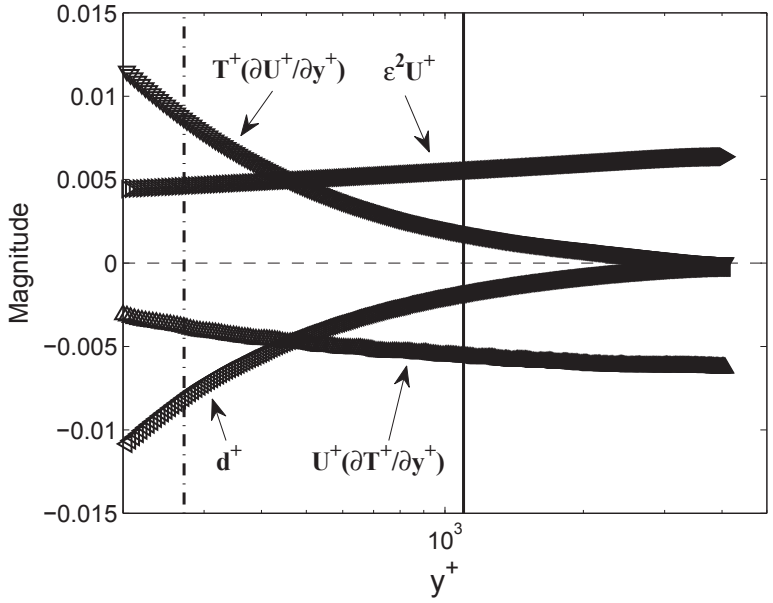

FIGURE 3.20: Profiles of terms in Eq. (3.20) across layer iii and iv at $\delta^+ = 4079$. $\triangle, U^+(\partial T^+/\partial y^+)$; $\bigtriangledown, T^+(\partial U^+/\partial y^+)$; $\lhd$, turbulent dissipation d^+; $\rhd, \epsilon^2 U^+$. The vertical dashed-dotted line denotes the external bound of layer ii. The vertical solid line denotes the external bound of layer iii.

Eqs. (3.48) and (3.50) respectively give the leading balances in layers iii and iv for the channels and pipes, and Eqs. (3.49) and (3.51) give the same for the boundary layers.

Since

$$\frac{\partial\left(U^+T^+\right)}{\partial y^+} = U^+\left(\frac{\partial T^+}{\partial y^+}\right) + T^+\left(\frac{\partial U^+}{\partial y^+}\right), \tag{3.52}$$

the individual behaviors of the two contributions on the right are of interest. For consistency, here partial differential is used for both channel/pipe and boundary layer analyses. Fig. 3.20 and Fig. 3.21 respectively show profiles of the terms in Eqs. (3.48) and (3.49) across layers iii and iv. These representative profiles are shown at a single δ^+ for the channel and boundary layer. Within layer iii, the four relevant terms are of the same order of magnitude but have different trends. The turbulent dissipation profile gradually moves

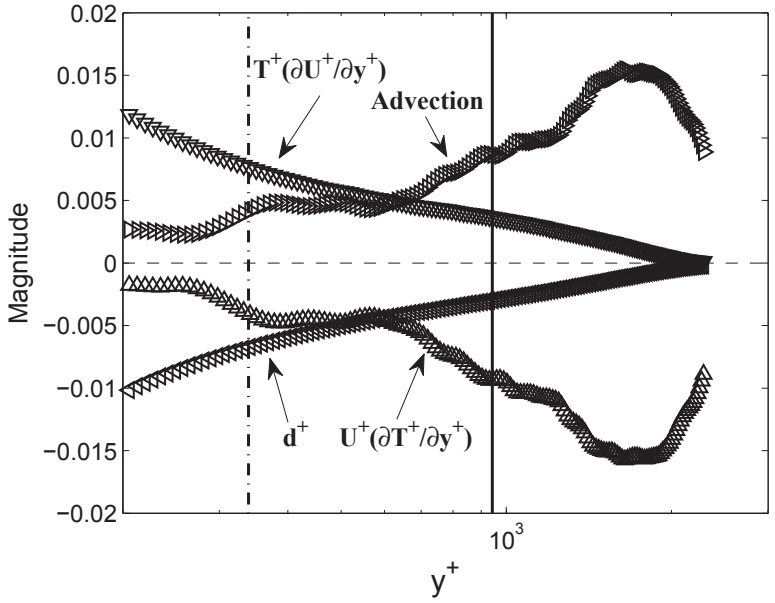

FIGURE 3.21: Profiles of terms in Eq. (3.21) across layer iii and iv at $\delta^+ = 2299$. $\triangle, U^+\,(\partial T^+/\partial y^+)$; $\bigtriangledown, T^+\,(\partial U^+/\partial y^+)$; $\lhd$, turbulent dissipation d^+; $\rhd$, advection. The vertical dashed-dotted line denotes the external bound of layer ii. The vertical solid line denotes the external bound of layer iii.

towards zero from below and crosses the $U^+\,(\partial T^+/\partial y^+)$ profile, which passed through zero to negative values in layer ii. Above the zero axis, the $T^+\,(\partial U^+/\partial y^+)$ and $\epsilon^2 U^+$ profiles exhibit a similar crossing. These crossing points exhibit a Reynolds dependence that is consistent with its position residing within layer iii for all δ^+. The two crossing positions for channels and boundary layers are respectively plotted versus $(\delta^+ - \sqrt{\delta^+})$ in Figs. 3.22 (a) and (b), while it has been confirmed that the pipe exhibits behaviors very similar to those in the channel. These data indicate that the $T^+\,(\partial U^+/\partial y^+)$ and $\epsilon^2 U^+$ (or advection) terms cross slightly closer to wall than the $U^+\,(\partial T^+/\partial y^+)$ and d^+ terms at lower Reynolds numbers, but these positions essentially coincide at higher δ^+. Similar to the phenomena illustrated in Fig. 3.12 and Fig. 3.13, the channel data gradually approach the indicated curve-fit line with increasing Reynolds number, while the boundary layer data

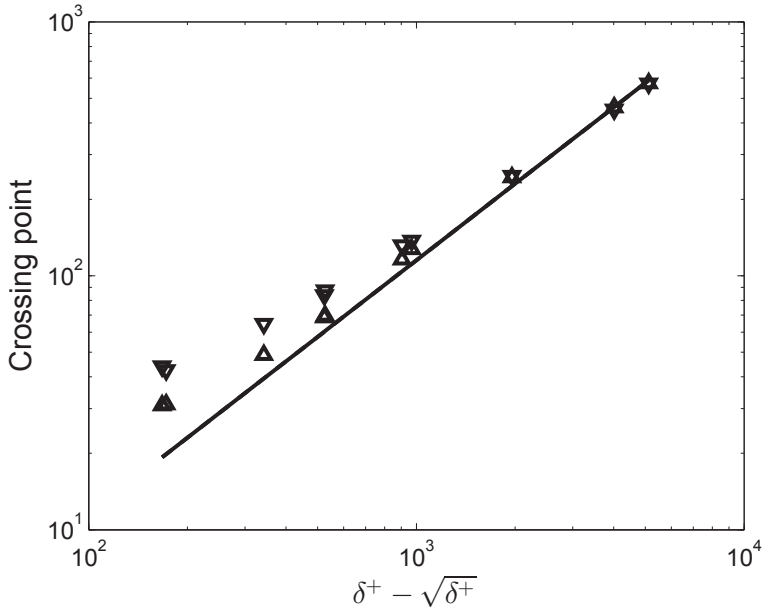

FIGURE 3.22: Reynolds number dependence of the two crossing points in Fig. 3.20 for channel and pipe flows. $\triangle$, crossing point between $T^+ (\partial U^+/\partial y^+)$ and $\epsilon^2 U^+$, curve fit is given by dashed line which is $0.1151(\delta^+ - \sqrt{\delta^+})$; $\triangledown$, crossing point between $U^+ (\partial T^+/\partial y^+)$ and turbulent dissipation d^+, curve fit is given by solid line which is $0.1150(\delta^+ - \sqrt{\delta^+})$.

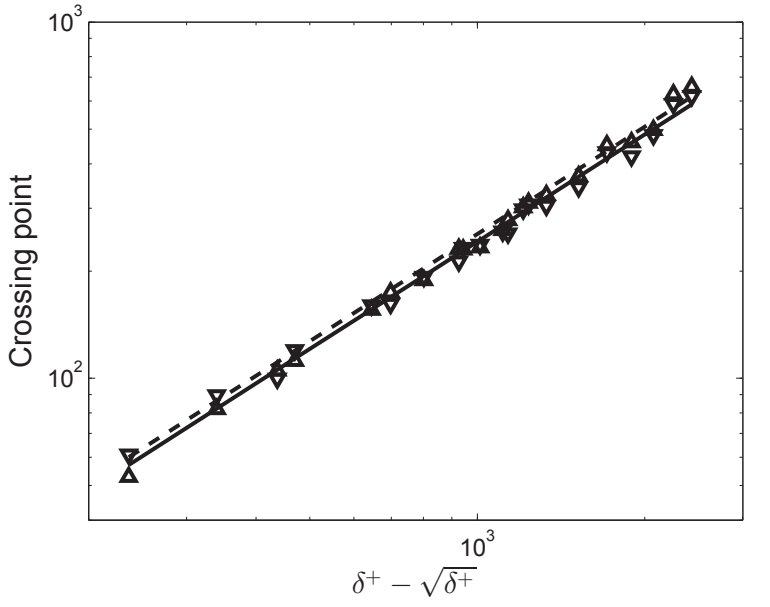

FIGURE 3.23: Reynolds number dependence of the two crossing points in Fig. 3.21 for boundary layers. $\triangle$, crossing point between $T^+ (\partial U^+/\partial y^+)$ and advection term, curve fit is given by dashed line which is $0.2542(\delta^+ - \sqrt{\delta^+})$; $\triangledown$, crossing point between $U^+ (\partial T^+/\partial y^+)$ and turbulent dissipation d^+, curve fit is given by solid line which is $0.2419(\delta^+ - \sqrt{\delta^+})$.

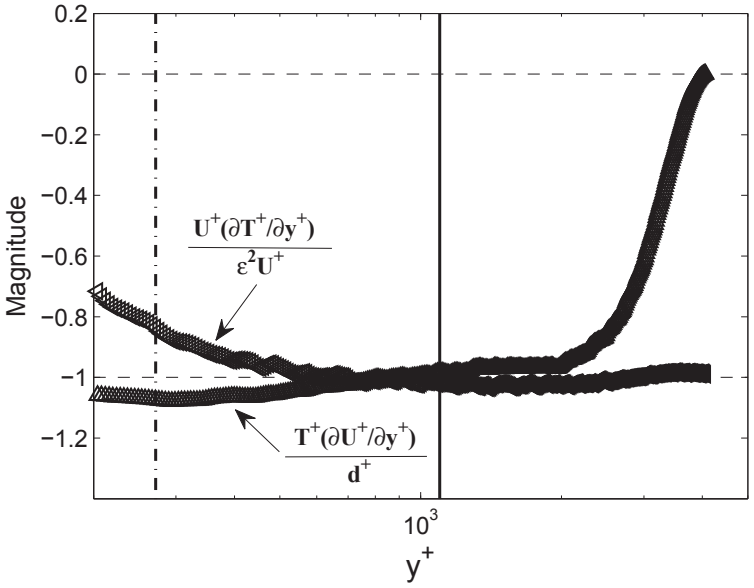

FIGURE 3.24: Ratios of $(\lhd)\, U^+ (\partial T^+/\partial y^+)$ to $\epsilon^2 U^+$ and $(\triangle)\, T^+ (\partial U^+/\partial y^+)$ to turbulent dissipation d^+ for turbulent channel flow at $\delta^+ = 4079$.

convincingly follow the linear curve-fit for all δ^+. For all three flows the profile-crossings occur slightly closer to $y^+_{ii\,end}$ than $y^+_{iii\,end}$.

Both the $T^+ (\partial U^+/\partial y^+)$ and the d^+ terms lose leading order in layer iv, becoming negligible compared to the $U^+ (\partial T^+/\partial y^+)$ and $\epsilon^2 U^+$ terms, or similarly the advection term in the boundary layer. Fig. 3.24 and Fig. 3.25 respectively show profiles of the ratio of $U^+ (\partial T^+/\partial y^+)$ to $\epsilon^2 U^+$ (or advection term), and the ratio of $T^+ (\partial U^+/\partial y^+)$ to d^+. As might be expected, although both the $T^+ (\partial U^+/\partial y^+)$ and d^+ terms are much smaller than the other two terms (and thus are not leading order), their ratio is nearly -1. This ratio then approaches zero at the edge of layer iv. Beyond the outer edge of layer ii the traditional production term, $T^+ (\partial U^+/\partial y^+)$, is initially balanced with the turbulent dissipation term, d^+, but with the traditional production term approaching zero more rapidly as $y^+ \to \delta^+$.

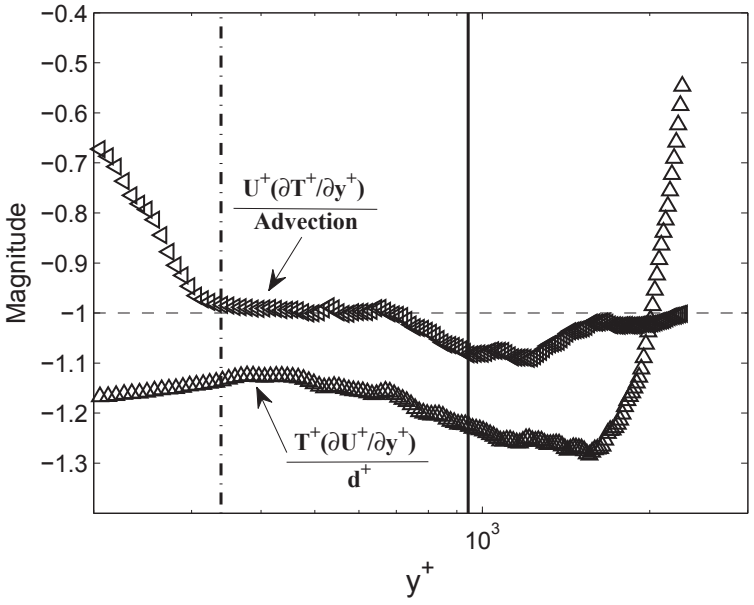

FIGURE 3.25: Ratios of ($\triangleleft$) $U^+ (\partial T^+/\partial y^+)$ to advection term and ($\triangle$) $T^+ (\partial U^+/\partial y^+)$ to turbulent dissipation d^+ for turbulent boundary layer at $\delta^+ = 2299$.

The ratio of the other two leading order terms is also approximately -1 throughout layer iv. This balance begins near the middle of layer iii for the channel/pipe, and near the outer edge of layer ii for the boundary layer. It is thus concluded that beyond layer ii, the $U^+ (\partial T^+/\partial y^+)$ term balances with the $\epsilon^2 U^+$ term for the channel/pipe, and similarly with the advection term for the boundary layer. Notably, the two separate balances in Fig. 3.20 and Fig. 3.21 reflect the individual balances of the mean and turbulence kinetic energy equations.

3.4 Basis for the Characteristic Length Scale of Layer iii

3.4.1 Channel and Pipe Flows

The empirical data analysis in Section 3.3.3 reveals that the inner-normalized width of layer iii of the total kinetic energy balance for channel and pipe flows scales with $\delta^+ - \sqrt{\delta^+}$ at finite Reynolds number. And the leading coefficient that is 0.2093 indicates that this layer iii is located in the inertial sublayer associated with the self-similarity admitted by the mean momentum equation (Klewicki, 2013b). The leading order balance equation across this layer is reflected by Eq. (3.48) in Section 3.3.4.

The mean momentum equation asymptotically admits an invariant form across a scaling layer hierarchy. This hierarchy resides between the inner and outer peak positions of the turbulent inertia (TI) term, where the TI term decreases slowly with increasing distance from the wall. The rescaled derivative of the turbulent inertial term in each scaling layer is written as

$$A = -\frac{d^2T^+}{dy^{+2}}\beta^{-\frac{3}{2}} = -\frac{d^2T^+}{dy^{+2}}\left(\frac{dT^+}{dy^+} + \frac{1}{\delta^+}\right)^{-\frac{3}{2}}. \tag{3.53}$$

Recall that β is a small and constant parameter, and the T^+ is transformed into T^+_β by $T^+_\beta = T^+ + y^+/\delta^+ - \beta y^+$.

On each scaling layer,

$$\frac{dT_\beta^+}{dy^+}\left(y_{\beta m}^+\right) = \frac{dT^+}{dy^+}\left(y_{\beta m}^+\right) + \frac{1}{\delta^+} - \beta = 0. \tag{3.54}$$

Here, $y_{\beta m}^+$ is where T_β^+ attains its maximum value in each scaling layer. Differentiation of Eq. (3.53) with respect to β gives

$$\frac{d^2T^+}{dy^{+2}}\frac{dy_{\beta m}^+}{d\beta} - 1 = 0. \tag{3.55}$$

Combination of Eq. (3.53) and Eq. (3.55) yields

$$\frac{dy_{\beta m}^+}{d\beta} = -A^{-1}\beta^{-\frac{3}{2}}. \tag{3.56}$$

A asymptotically approaches a constant on the inertial sublayer where the viscous force term loses its leading order, as $\delta^+ \to \infty$. Recall that $A \to \textit{constant}$ physically indicates a constant flux of turbulent force from one layer to the next on the hierarchy. It also describes that W^+ approaches a direct proportionality with y^+ as $\delta^+ \to \infty$. It is where the self-similarity emerges on an interior domain that is sufficiently remote from the overall flow boundaries as $\delta^+ \to \infty$. Eq. (3.56) is integrated to obtain

$$y_{\beta m}^+ = 2A^{-1}\beta^{-\frac{1}{2}} + C, \tag{3.57}$$

where C is the integration constant. Generally, $y^+_{\beta m}$ uniquely corresponds to y^+ on the hierarchy, replacing $y^+_{\beta m}$ by y^+ and rewriting the β in terms of dT^+/dy^+ yields

$$\frac{dT^+}{dy^+} = \left(\frac{2}{A}\right)^2 \left[\frac{1}{(y^+ - C)^2} - \frac{1}{(y^+_m - C)^2}\right] = \frac{\phi^2}{(y^+ - C)^2} - \frac{\phi^2}{(y^+_m - C)^2}, \tag{3.58}$$

where $\phi^2/(y^+_m - C)^2$ substitutes $1/\delta^+$, $\phi = 2/A$, C is a constant, and T^+ attains its maximum value, T^+_m, at the position y^+_m. Also, $\phi = dy/dW$, which is physically the stretching of the y coordinate required to produce an invariant representation of the flux of turbulent force generated by the momentum transport of W sized eddy. Integration of Eq. (3.58) gives

$$T^+ = C' - \frac{\phi^2}{y^+ - C} - \frac{y^+\phi^2}{(y^+_m - C)^2}. \tag{3.59}$$

The position of T^+_m is empirically and asymptotically verified to be $y^+_m = \lambda_m\sqrt{\delta^+}$, (Long and Chen, 1981; Afzal, 1982; Klewicki et al., 2014) where $\lambda_m \to$ constant as $\delta^+ \to \infty$. Neglecting C for large δ^+ and using $y^+_m = \lambda_m\sqrt{\delta^+}$ gives

$$\frac{dT^+}{dy^+} = \frac{\phi^2}{y^{+2}} - \frac{\phi^2}{\lambda^2_m\delta^+}, \tag{3.60}$$

and

$$T^+ = C' - \frac{\phi^2}{y^+} - \frac{y^+\phi^2}{\lambda^2_m\delta^+}. \tag{3.61}$$

Noting that $T^+(\delta^+) = 0$, evaluation of Eq. (3.61) as $\delta^+ \to \infty$ yields

$$C' = \frac{\phi^2_c}{\lambda^2_m}., \tag{3.62}$$

where $\phi \to \phi_c$ as $\delta^+ \to \infty$. Evaluation of of Eq. (3.61 as $\delta^+ \to \infty$ at y_m^+ where $T_m^+ \to 1$ gives

$$1 = \frac{\phi_c^2}{\lambda_m^2} - \frac{\phi_c^2}{\lambda_m \sqrt{\delta^+}} - \frac{\phi^2 \sqrt{\delta^+}}{\lambda \delta^+}. \tag{3.63}$$

Thus $\lambda_m \to \phi_c$ and $C' \to 1$ as $\delta^+ \to \infty$.

The first term in Eq. (3.48) is comprised of two parts, i.e., $U^+ \left(dT^+/dy^+\right)$ and $T^+ \left(dU^+/dy^+\right)$. Each of these two terms is of the same order of magnitude as the last term, $\epsilon^2 U^+$. Letting $U^+ \left(dT^+/dy^+\right) \sim \epsilon^2 U^+$('$\sim$' denoting same order of magnitude) gives

$$\frac{dT^+}{dy^+} = O\left(\epsilon^2\right). \tag{3.64}$$

This derivative magnitude is consistent with classical outer scaling arguments (Tennekes and Lumley, 1972), and the momentum equation analyses of Wei et al. (2005a). Specifically, dT^+/dy^+ becomes $O\left(\epsilon^2\right)$ at the beginning of layer III and retains this order of magnitude throughout both layers III and IV of the momentum balance. From Eq. (3.60),

$$\frac{\phi^2}{y^{+2}} - \frac{\phi^2}{\lambda_m^2 \delta^+} = O\left(\epsilon^2\right). \tag{3.65}$$

As $\delta^+ \to \infty$, $\phi \to \phi_c$ and $\lambda_m \to \phi_c$, where ϕ_c is a constant. Thus ϕ^2/λ_m^2 is $O\left(1\right)$, and ϕ_c^2 itself is an $O\left(1\right)$ constant. Under these conditions, Eq. (3.65) is only valid when $y^+ \geqslant O\left(1/\epsilon\right)$. Requiring $y^+ \geqslant O\left(1/\epsilon\right)$ in Eq. (3.61) and noting that $C' \to 1$ as $\delta^+ \to \infty$ yields

$$T^+ = O\left(1 - \epsilon\right). \tag{3.66}$$

This order of magnitude is corroborated by the relevant region residing beyond the peak of T^+, where the maximum value T_m^+ is $1 - O(\epsilon)$ at y_m^+ (Klewicki et al., 2014).

Within layer iii, a rescaling of Eq. (3.60) is now applied such that all terms reflect the actual orders of magnitude. The present analysis only requires considering the leading order balance between $d\left[U^+T^+\right]/dy^+$ and $\epsilon^2 U^+$. Rescaling begins by setting

$$U^+ = \alpha \bar{U}, \quad T^+ = \beta \bar{T}, \quad y^+ = y_0^+ + \gamma \bar{y}, \tag{3.67}$$

where $\bar{U}$, $\bar{T}$ and $\bar{y}$ are all $O(1)$ as $\delta^+ \to \infty$. Analogous to y_m^+ relative to layer III, y_0^+ is the position where the $d\left[U^+T^+ - \langle v^+K^+\rangle\right]/dy^+$ term changes sign in layer iii. The indicated transformations give

$$\frac{d}{dy^+}\left[U^+T^+\right] = \frac{\alpha\beta}{\gamma}\frac{d}{d\bar{y}}\left[\bar{U}\bar{T}\right], \quad \epsilon^2 U^+ = \epsilon^2 \alpha \bar{U}. \tag{3.68}$$

By the requirement, the order of magnitude of both terms on the right must match with each other. Rendering all terms $O(1)$ requires that

$$\frac{\alpha\beta}{\gamma} = \epsilon^2 \alpha, \tag{3.69}$$

or

$$\gamma = \frac{1}{\epsilon^2}\beta. \tag{3.70}$$

From Eqs. (3.66) and (3.67) $\beta = 1 - \epsilon$ in layer iii, and with this γ is determined by

$$\begin{aligned} \gamma &= \frac{1}{\epsilon^2}(1-\epsilon) \\ &= \frac{1}{\epsilon^2} - \frac{1}{\epsilon}, \end{aligned} \tag{3.71}$$

or

$$\begin{aligned} y^+ &= y_0^+ + \left(\frac{1}{\epsilon^2} - \frac{1}{\epsilon}\right)\bar{y} \\ &= y_0^+ + (\delta^+ - \sqrt{\delta^+})\bar{y}. \end{aligned} \tag{3.72}$$

By definition, $\bar{y}$ is $O(1)$ in layer iii, and thus it follows that the inner-normalized width of this layer for channel/pipe is $O(\delta^+ - \sqrt{\delta^+})$. This scaling is interpreted as a finite Reynolds number correction to traditional outer scaling, since it is apparent that $(\delta^+ - \sqrt{\delta^+}) \to \delta^+$ as $\delta^+ \to \infty$.

3.4.2 Boundary layer

The leading balance in layer iii for boundary layer is presented in Eq. (3.49). As evident in Fig. 3.20 and Fig. 3.21, different from either the MPD, i.e., $\epsilon^2 U^+$, or the WRS, i.e., $U^+(\partial T^+/\partial y^+)$, terms for channel/pipe which monotonically increases or decreases across layer iii and iv, both the Advection and WRS terms for boundary layer firstly go to attain their peak values and then tend to approach zero near the edge. Fig. 3.26 shows the ratio of the turbulent advection to the mean advection across layer iii and iv. Turbulent

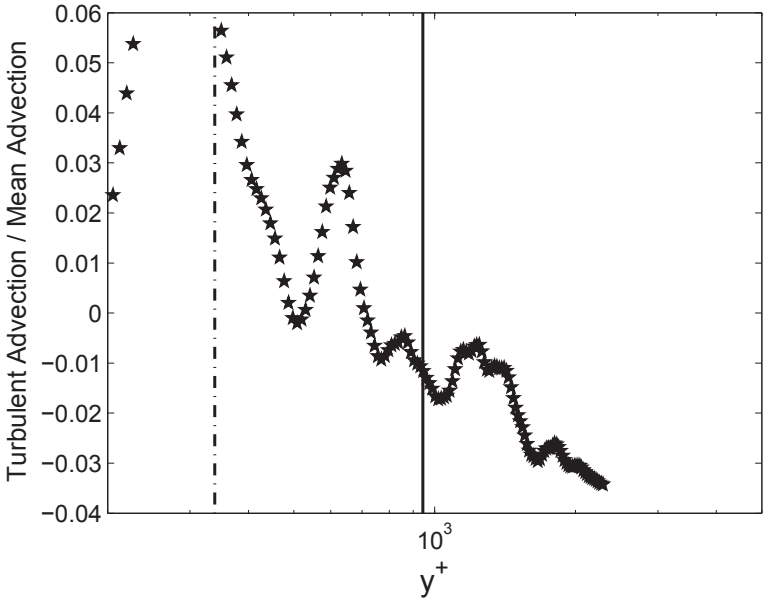

FIGURE 3.26: Ratios of turbulent advection to mean advection for turbulent boundary layer at $\delta^+ = 2299$. The vertical dashed-dotted line denotes the external bound of layer ii. The vertical solid line denotes the external bound of layer iii.

advection is negligible compared to the mean advection, and the leading balance equation is reduced into

$$U^+\left(\frac{\partial T^+}{\partial y^+}\right)+\left[-U^+\frac{\partial}{\partial x^+}\left(\frac{1}{2}U^{+2}\right)-V^+\frac{\partial}{\partial y^+}\left(\frac{1}{2}U^{+2}\right)\right]+T^+\left(\frac{\partial U^+}{\partial y^+}\right)+d^+=0. \quad (3.73)$$

A desirable transformation is applied to the mean advection term based on the analysis of Morrill-Winter et al. (2017) in order to modify the curve profiles into shapes similar to the channel/pipe.

Transformation of the mean inertia term gives

$$\begin{aligned} -U^+\frac{\partial}{\partial x^+}\left(\frac{1}{2}U^{+2}\right) - V^+\frac{\partial}{\partial y^+}\left(\frac{1}{2}U^{+2}\right) &= -U^+\left(U^+\frac{\partial U^+}{\partial x^+} + V^+\frac{\partial U^+}{\partial y^+}\right) \\ &= U^+\psi(x^+, y^+)M_p^+, \end{aligned} \tag{3.74}$$

where ψ is a fraction evaluated between 0 and 1, and M_p^+ is the peak magnitude of the mean inertia, i.e., $-\left[U^+\left(\partial U^+/\partial x^+\right) + V^+\left(\partial U^+/\partial y^+\right)\right]$. Subsequently, an invariance of ψ is defined as

$$\bar{\psi} = \frac{1}{\delta^+}\int_0^{\delta^+} \psi\left(x^+, y^+\right) dy^+, \tag{3.75}$$

since the mean inertia is an outer scale phenomenon. $\bar{\psi}$ was experimentally determined to be a constant, 0.57 ± 0.047, based on the available data (Morrill-Winter et al., 2017). Now ψ can be normalized by $\bar{\psi}$ such that $\underline{\psi}(x^+, y^+) = \psi/\bar{\psi}$. Thus

$$U^+\psi(x^+, y^+)M_p^+ = U^+\bar{\psi}\left(\delta^+\right)M_p^+\underline{\psi}\left(x^+, y^+\right). \tag{3.76}$$

Since $\bar{\psi}\left(\delta^+\right)M_p^+$ is proved to be $1/\delta^+$ (Morrill-Winter et al., 2017), the mean advection becomes

$$-U^+\frac{\partial}{\partial x^+}\left(\frac{1}{2}U^{+2}\right) - V^+\frac{\partial}{\partial y^+}\left(\frac{1}{2}U^{+2}\right) = U^+\frac{1}{\delta^+}\underline{\psi}\left(y^+, \delta^+\right). \tag{3.77}$$

Here $\underline{\psi}$ is a function of y^+ and δ^+. The mean advection term is presented in a form that explicitly contains the $1/\delta^+$ found in the mean pressure diffusion term in channel/pipe. The primary goal is to modify both the MA and WRS profiles that they correspondingly varies similarly to the MPD and WRS in channel/pipe. The Reynolds stress is modified

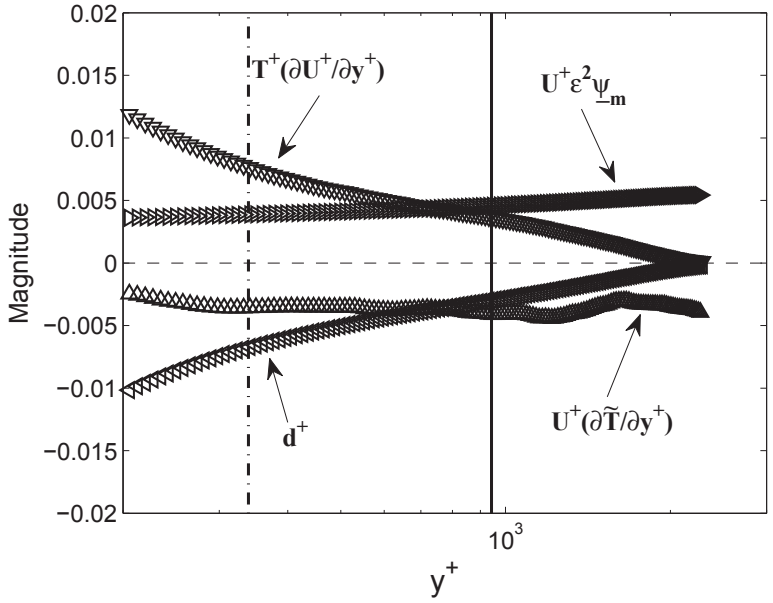

FIGURE 3.27: Profiles of terms in Eq. (3.79) for turbulent boundary layer at $\delta^+ = 2299$. The vertical dashed-dotted line denotes the external bound of layer ii. The vertical solid line denotes the external bound of layer iii.

as

$$\tilde{T} = T^+ + \frac{1}{\delta^+}\int_0^{y^+} \Gamma\left(y^+, \delta^+\right) dy^+, \tag{3.78}$$

where $\Gamma(y^+, \delta^+) = \underline{\psi}(y^+, \delta^+) - \underline{\psi}_m(\delta^+)$, $\underline{\psi}_m(\delta^+) = \underline{\psi}(y_m^+, \delta^+)$, and y_m^+ is where the the turbulent inertia term crosses zero from above. Note that $d\tilde{T}/dy^+ = 0$ at y_m^+ is preserved under this transformation. The leading balance equation across layer iii becomes

$$U^+\left(\frac{\partial \tilde{T}}{\partial y^+}\right) + U^+\frac{1}{\delta^+}\underline{\psi}_m + T^+\left(\frac{\partial U^+}{\partial y^+}\right) + d^+ = 0. \tag{3.79}$$

Fig. 3.27 shows the representative profiles of terms in Eq. (3.79) across layer iii and iv. Here, that $M_p^+ = 1.76/\delta^+$ and $\underline{\psi}_m = 0.46$ are used in the calculation (Morrill-Winter et al., 2017). The profiles of $U^+\epsilon^2\underline{\psi}_m$ and $U^+(\partial\tilde{T}/y^+)$ are respectively analogous to the

$\epsilon^2 U^+$ and $U^+(\partial T^+/\partial y^+)$ for channel in Fig. 3.20. Thus the partial symbol, ∂, can be written as the differential symbol, d. The first two terms are approximately in balance within the layer iii, i.e.,

$$O\left(\frac{\partial \tilde{T}}{\partial y^+}\right) = O\left(\epsilon^2 \underline{\psi}_m\right). \tag{3.80}$$

Here, the U^+ is cancelled out on both sides.

Following the previous study of the channel, a transformation is employed that

$$\tilde{T}_\chi = \tilde{T} + \frac{1}{\delta^+}\underline{\psi}_m y^+ - \chi y^+, \tag{3.81}$$

where χ is small positive parameter that is bounded as $0 \leqslant \chi \leqslant (d\tilde{T}/dy^+)_{peak}$. This transformation leads to a scaling layer hierarchy similar to the channel (Klewicki et al., 2014). This scaling layer width, W^+, is evaluated as $W^+ = (-d^2U^+/dy^{+2})^{-1/2}$. The onset of the linear behavior of W^+ is found to scale with $\sqrt{\delta^+}$, i.e., $y^+ = 3.6\sqrt{\delta^+}$ (Morrill-Winter et al., 2017). So this layer iii is also located in the inertial region of the mean momentum transport for the boundary layer. Following the same analysis in previous Section (3.4.1) from Eq. (3.53) to Eq. (3.66), the order of magnitude of $\tilde{T}$ in layer iii is verified that

$$\tilde{T} = O\left(1 - \epsilon\right). \tag{3.82}$$

The balance in (3.80) is under consideration. The corresponding rescalings are given by

$$\tilde{T} = P\bar{\tilde{T}}, \quad y^+ = y_0^+ + Q\bar{y}, \tag{3.83}$$

where $\bar{\tilde{T}}$ and $\bar{y}$ are both $O(1)$ as $\delta^+ \to \infty$. Like the channel, y_0^+ is the position where the $d\left[U^+T^+ - \langle v^+K^+\rangle\right]/dy^+$ term changes sign in layer iii. The rescaling transformations give

$$\frac{dT}{dy^+} = \frac{P}{Q}\frac{d\bar{\tilde{T}}}{d\bar{y}}. \tag{3.84}$$

Note that $\underline{\psi}_m$ is $O(1)$, and rendering both terms $O(1)$ requires that

$$\frac{P}{Q} = \epsilon^2, \tag{3.85}$$

or

$$Q = \frac{1}{\epsilon^2}P. \tag{3.86}$$

P is the order of magnitude of $\tilde{T}$ in layer iii, i.e., $P = 1 - \epsilon$. Thus Q is determined by

$$\begin{aligned} Q &= \frac{1}{\epsilon^2}(1-\epsilon) \\ &= \frac{1}{\epsilon^2} - \frac{1}{\epsilon}, \end{aligned} \tag{3.87}$$

or

$$\begin{aligned} y^+ &= y_0^+ + \left(\frac{1}{\epsilon^2} - \frac{1}{\epsilon}\right)\bar{y} \\ &= y_0^+ + (\delta^+ - \sqrt{\delta^+})\bar{y}. \end{aligned} \tag{3.88}$$

By definition, $\bar{y}$ is $O(1)$ in layer iii, and thus it follows that the inner-normalized width of this layer for boundary layer is $O(\delta^+ - \sqrt{\delta^+})$. This scaling is interpreted as a finite

TABLE 3.1: Magnitude ordering and approximate scaling behaviors associated with the four layer structure of the total kinetic energy equations for channel/pipe and boundary layer. VD, D, PT, and PD respectively refer to the viscous diffusion, dissipation, production/turbulent diffusion and total pressure diffusion terms in Eq. (3.43). Note that $\left(\delta - \sqrt{\nu\delta/u_\tau}\right)$ approaches δ as $\delta^+ \to \infty$.

Channel/Pipe flow		
Layer	Magnitude ordering	Δy increment
i	$\lvert VD\rvert \cong \lvert D\rvert$	$O\left(\nu/u_\tau\right) (\simeq 1.5)$
ii	$\lvert VD\rvert \cong \lvert D\rvert \cong \lvert PT\rvert$	$O\left(\delta - \sqrt{\nu\delta/u_\tau}\right) (\simeq 0.07)$
iii	$\lvert D\rvert \cong \lvert PT\rvert \cong \lvert PD\rvert$	$O\left(\delta - \sqrt{\nu\delta/u_\tau}\right) (\simeq 0.21)$
iv	$\lvert PT\rvert \cong \lvert PD\rvert$	$O\left(\delta\right) (\simeq 0.68)$

TABLE 3.2: Magnitude ordering and approximate scaling behaviors associated with the four layer structure of the total kinetic energy equations for channel/pipe and boundary layer. VD, D, PT and APD respectively refer to the viscous diffusion, dissipation, production/turbulent diffusion and advection/turbulent pressure diffusion terms in Eq. (3.44). Note that $\left(\delta - \sqrt{\nu\delta/u_\tau}\right)$ approaches δ as $\delta^+ \to \infty$.

Boundary layer flow		
Layer	Magnitude ordering	Δy increment
i	$\lvert VD\rvert \cong \lvert D\rvert$	$O\left(\nu/u_\tau\right) (\simeq 1.5)$
ii	$\lvert VD\rvert \cong \lvert D\rvert \cong \lvert PT\rvert$	$O\left(\delta - \sqrt{\nu\delta/u_\tau}\right) (\simeq 0.17)$
iii	$\lvert D\rvert \cong \lvert PT\rvert \cong \lvert APD\rvert$	$O\left(\delta - \sqrt{\nu\delta/u_\tau}\right) (\simeq 0.25)$
iv	$\lvert PT\rvert \cong \lvert APD\rvert$	$O\left(\delta\right) (\simeq 0.58)$

Reynolds number correction to traditional outer scaling, since it is apparent that $(\delta^+ - \sqrt{\delta^+}) \to \delta^+$ as $\delta^+ \to \infty$.

3.5 Summary

Properties of the layer structure associated with the total kinetic energy equation are summarized in Table 3.1 and Table 3.2. From this table, it is evident that channel, pipe, and boundary layer flows qualitatively exhibit the same behaviors to within the

differences between the mean pressure and mean advection effects. Quantitatively, the layer thicknesses are shown herein to exhibit distinct Reynolds number dependencies. As is evident, layer i adheres to inner scaling. And the width of layer ii grows at a rate proportional to $\left(\delta - \sqrt{\nu\delta/u_\tau}\right)$. But the increment for the channel/pipe is less than that for the boundary layer. This difference is compensated by the thickness of layer iv, where the advection term is present in the leading balance of layer iv for the boundary layer. The underlying physical mechanism for the different layer ii thickness is unknown. The analysis in section 3.4 leads to surmise that the inner-normalized layer iii width follows a $(\delta^+ - \sqrt{\delta^+})$ dependence at finite Reynolds numbers. This result appears to hold in the boundary layer for all observed δ^+, and also seems to hold for the individual upper boundaries of layers ii and iii. In the channel the present estimates suggest that the layer iii width scales with this length for $\delta^+ > 1000$. The layer scaling behaviors associated with the total kinetic energy differ substantially from those of the mean momentum balance. It is significant to note, however, that the layer structure of the mean kinetic energy equation, which is identical to that of the mean momentum equation, is embedded within this structure.

The present results indicate that the major portions of layers ii and all of layer iii and iv reside in the inertial/advection balance layer (layer IV) of the mean momentum balance. Here the Reynolds stress gradient balances the pressure force in channel flow or the mean advection in the boundary layer flow, while the viscous force is negligible. For the total kinetic energy balance the viscous diffusion term gradually becomes negligible near the external bound of layer ii, and the dissipation term loses leading order in layer

iv. The leading order balance is inviscid in the outer 68% of the channel/pipe, and outer 58% of the boundary layer.

Lastly, it is noted that the leading order balances associated with the total kinetic energy budget exhibit an intriguing and potentially telling set of behaviors. Recalling that the total budget is the sum of the mean and turbulence budgets, the relevant behaviors are that mean budget contributions dominate the leading terms near the wall, the turbulence equation contributions become leading order over an interior region, and then in the outermost portion mean equation terms return to dominance. This spatial inter-weaving of the leading order contributions suggests that care should be taken when using traditional Reynolds averaging to discern properties associated with the energetic motions within the flow.

CHAPTER 4

SCALING PROPERTIES OF SCALAR TRANSPORT IN TURBULENT CHANNEL FLOW

4.1 Background

Wall-bounded turbulent flows pervade industrial applications. This fact broadly motivates the numerous and on-going efforts to investigate the properties of wall-flows. In this regard, the associated transport of heat and mass are of particular technological importance in applications pertaining to energy efficiency, environmental concerns, and manufacturing processes. For example, thermal processing seeks to force a temperature change in a system that enables or disables some material transformation, while the purpose of thermal control seeks to regulate within desired bounds, or to control in time within a certain margin, the temperature of a system to ensure an application-specific optimal condition.

Prediction across parameter variations is important to such aims, and thus there has been considerable effort directed toward quantifying scaling behaviors. Scaling analyses

involving the application multiple-scale approaches are often used to explore parameter dependent scaling properties of statistical profiles (Yaglom, 1979; Klewicki, 2010; Marusic et al., 2010; Smits et al., 2011a). An especially prominent scaling framework is based upon the notion of an overlap layer. Here it is postulated that there exists a region where respective functions of inner and outer normalized distance from the wall are simultaneously valid (Izakson, 1937; Millikan, 1938). An alternative approach that more directly invokes the idea of distance-from-the-wall scaling can be deduced from dimensional analysis (Landau and Lifshitz, 2013). Under this assumption, the attached eddy phenomenology is inherently consistent with the existence of a logarithmic mean velocity profile (Townsend, 1980; Perry and Chong, 1982; Perry and Marusic, 1995). More recent studies reveal that subsumed within the domain where the mean exhibits a logarithmic increase the variance of the streamwise velocity fluctuations as well as their higher order even moments also vary logarithmically (Meneveau and Marusic, 2013; Klewicki et al., 2015; Zhou and Klewicki, 2015). Within this region the mean dynamics are dominated by the inertia, and the mean momentum equation admits a self-similar structure (Klewicki, 2013b).

Kader (1991) described the law of the wall for temperature in a manner similar to the inner function in the overlap framework for velocity. This formulation follows from the assumption that, in the near wall region, the mean temperature, Θ, depends only on the shear stress at the wall, τ_w, the heat flux at the wall, q_w, the distance from the wall, the mass density, ρ, dynamic viscosity, μ, specific heat, C_p, and thermal conductivity, k. Consistent with the analogy between heat and momentum, a logarithmic profile for

temperature is observed for inner-normalized distances from the wall greater than about 30 and Prandtl number less than 1 (Kader and Yaglom, 1972). As such, the overlap layer approach has been used to reason the logarithmic structure of the thermal boundary layer (Gowen and Smith, 1967; Kader, 1981). Based on the overall mean temperature profile structure, the inner region close to the solid wall is seen to be composed of a molecular sublayer and a thermal buffer layer, while logarithmic and wake layers comprise an outer region that extends to the centerline of the channel/pipe. Like for velocity, some divide the logarithmic (overlap) layer into two sublayers (George and Castillo, 1997; Castillo and George, 2001). The convective sublayer is characterized by negligible conductive effect, while heat transfer is under a detectable influence of conduction in the thermal mesolayer.

Based upon his review of available data, Kader (1981) estimated the thermal Kármán constant, k_θ, for the logarithmic mean temperature profile to be about 0.47. This constant value for a fully developed turbulent channel flow with uniform heating from both walls was found by Kawamura et al. (1999) to be roughly independent of Reynolds number and closer to the Kármán constant for velocity, i.e., $0.40 \lesssim k_\theta \lesssim 0.42$. It is relevant to note, however, that the law of the wall for temperature apparently breaks down in flows where the law of the wall for velocity is still valid. It is especially observed that the logarithmic increase of mean temperature is significantly more affected by pressure gradients than the mean velocity (Bradshaw and Huang, 1995).

Interest in statistical behaviors in wall turbulent flows has motivated approaches that more directly incorporate the mean equations to discern scaling behaviors. Based on the relative magnitude of terms in the mean momentum equation, following Wosnik et al.

(2000), Wei et al. (2005a) revealed a four layer structure distinct from the traditional description. As expected, layer I and layer IV (the innermost and outermost layers) respectively comply with inner and outer scaling. However, an intermediate length scale, $\sqrt{\nu\delta/u_\tau}$, is both empirically observed and analytically shown to characterize the other two layers. Similarly, Afzal and coworkers (Afzal, 1982, 1984; Seena and Afzal, 2008) deduced an intermediate scaling for the thermal meso-layer of fully-developed turbulent channel flow and transitionally rough channel flow. Their analysis incorporates an intermediate layer that has its own characteristic scaling, and that lies between the traditional inner and outer layers. Their formulation also employs a matching procedure that incorporates three layers and two overlapping regions over which two adjacent logarithmic regions for the mean temperature profile are shown to asymptotically form. The thermal meso-length scale they employ constitutes the geometric mean of the inner, α/u_τ, and outer, δ, thermal length scales, and is given by $\delta/\sqrt{Pr\delta^+}$. Here, α is the thermal diffusivity, δ is the half channel height, u_τ is the friction velocity and Pr is the Prandtl number. Afzal's analysis similarly employs an intermediate scaled temperature $T_m = (\Theta_w + \Theta_c)/2$, where Θ_w and Θ_c are the temperature at the wall and the channel centerline, respectively.

Using an analysis that also incorporates an intermediate scale, Wei et al. (2005b) examined fully developed thermal transport in channels with constant wall heat flux. They introduced a new inner variable, $y_\sigma = \eta/\sigma^2$, where $\eta = y/\delta$ and σ is a parameter defined as a function of δ^+ and Peclet number, $Pe_\tau = Pr\delta^+$. Consequently, the corresponding thermal mesoscale, $\sqrt{(\Theta_w - \Theta_c)/(\Theta_\tau Pr\delta^+)}$ where $\Theta_\tau = q_w/\rho C_p u_\tau$, is different from the geometric mean of the inner and outer thermal length scales, $\sqrt{\alpha\delta/u_\tau}$. Existing DNS,

however, significantly limited the range of parameters over which Wei et al. could validate their analysis. Based on DNS data covering a broader range of both Reynolds and Prandtl numbers, Saha et al. (2014) explored the scaling properties of scalar transport under a larger range of constant wall flux conditions. They showed that, based upon the magnitude ordering of terms, a four-layer thermal regime exists when $Pr \gtrsim 0.6$ at $\delta^+ = 180$. This four layer regime is analogous to that first identified by Wei et al. (2005a). Their analysis incorporates the inner normalized mesoscale, $\sqrt{Pe_\tau}$, which they show can be used to effectively merge both the mean temperature and turbulent heat flux over a domain that starts inside the peak heat flux location out to a position near the centerline.

The previous analyses of the mean thermal energy equation by Wei et al. (2005b) and Saha et al. (2014) investigated flows having a constant surface heat flux boundary condition. Analytically, this presents a significant challenge when compared to the corresponding streamwise momentum equation analysis where the pressure gradient in the inner-normalized form of the equation is represented by $1/\delta^+$. Additionally, the low Reynolds numbers of previous data make it difficult (and less convincing) to validate the veracity of the analytical results associated with an asymptotic analysis. In particular, their data analyses of the mean scalar equation failed to provide comparable evidence for a scaling layer hierarchy as has been shown for the mean momentum equation, or clearly delineate trends for varying Reynolds number and Prandtl number.

The present study follows the same methodology as the mean momentum (Wei et al., 2005a) and kinetic energy budget (Zhou and Klewicki, 2016) to investigate the mean scalar equation (Zhou et al., 2017) and scalar variance equation with constant heat generation for

the fully-developed turbulent channel flow. The uniform heat generation term addresses the previous challenge and reduces the mean scalar equation into a form that is much more analogous to the mean momentum equation. Furthermore, herein I employ DNS data from Pirozzoli et al. (2016) covering a significantly larger range of Reynolds Prandtl numbers, which provide much more compelling support for the analytical conclusions and theoretical predictions, and more clearly Re and Pr trends.

In what follows, the ratio of the molecular diffusion (MD) term to the gradient of turbulent heat flux (GT) term in the mean scalar equation is employed to reveal a four-layer leading balance structure. Both the Reynolds number and Prandtl number dependent scaling of these layer thicknesses is then empirically quantified with DNS data and verified through analysis of the mean equation. Like for the momentum field, the analysis also indicates that the mean scalar equation can be cast into an invariant form that properly reflects the local dominant physical mechanism, and which exposes the effect of the governing small parameter on an intrinsic scaling layer hierarchy. The Prandtl number impact on the width distribution of the layer hierarchy is quantified and discussed relative to the underlying physics. Consistent with the analysis, on the layer hierarchy there exists a domain where molecular diffusion effects are sub-dominant, and the layer width function becomes proportional to the distance from the wall. Here the mean equation is shown to asymptotically admit a similarity solution in the form of a logarithmic mean temperature profile. The behaviors of the coefficients in the logarithmic expression, including k_θ, are also described. Also the total scalar variance equation is explored to reveal another four layer structure with properties similar to that of the total kinetic

energy equation. Finally, The factors that lead to the difference between the Kármán constant, k, and thermal Kármán constant, k_θ are quantitatively explored.

4.2 Mean Scalar Equation

The time-averaged steady state mean scalar equation is

$$U\frac{\partial\Theta}{\partial x}+V\frac{\partial\Theta}{\partial y}+W\frac{\partial\Theta}{\partial z}=\alpha\left[\frac{\partial^2\Theta}{\partial x^2}+\frac{\partial^2\Theta}{\partial y^2}+\frac{\partial^2\Theta}{\partial z^2}\right]-\frac{\partial\left\langle u\theta\right\rangle}{\partial x}-\frac{\partial\left\langle v\theta\right\rangle}{\partial y}-\frac{\partial\left\langle w\theta\right\rangle}{\partial z}+Q, \quad (4.1)$$

where Θ is the mean temperature and θ is the corresponding fluctuating temperature (and similarly for the velocity components), α is the thermal diffusivity, and Q is the unit heat generation.

The analysis considers statistically stationary, fully-developed, incompressible turbulent flow and passive scalar transport in a two dimensional channel. The half channel height is given by δ. Note that, unlike the typical heat transfer case in which there is a constant surface heat flux (Saha et al., 2014), this form is simpler, and thus affords a more comprehensive analytical treatment. Under a uniform heat generation Q with the zero temperature on both the upper and lower walls, the mean scalar equation reduces to

$$\alpha\frac{d^2\Theta}{dy^2}-\frac{d\left\langle v\theta\right\rangle}{dy}=-Q. \quad (4.2)$$

Integration of Eq. (4.2) from y to δ with the conditions $d\Theta/dy = 0$ and $\langle v\theta \rangle = 0$ at the centerline gives

$$\alpha \frac{d\Theta}{dy} - \langle v\theta \rangle = Q\,(\delta - y)\,. \tag{4.3}$$

Using the boundary condition that at $y = 0$,

$$-\langle v\theta \rangle|_{wall} = 0. \tag{4.4}$$

gives

$$\alpha \frac{d\Theta}{dy}|_{wall} = Q\delta. \tag{4.5}$$

Inner-normalization is applied to each term in Eq. (4.3) with the friction temperature, i.e., $\theta_\tau = \frac{\alpha}{u_\tau}\frac{d\Theta}{dy}|_{wall}$, u_τ and ν, which can be deduce from dimensional analysis.

$$\Theta^+ = \frac{\Theta}{\theta_\tau}, \quad -\left\langle v^+\theta^+ \right\rangle = -\frac{\langle v\theta \rangle}{u_\tau \theta_\tau}, \quad y^+ = \frac{y u_\tau}{\nu}. \tag{4.6}$$

With the boundary condition (4.5), the inner-normalized version of Eq. (4.3) becomes

$$\frac{1}{Pr}\frac{d\Theta^+}{dy^+} - \left\langle v^+\theta^+ \right\rangle = 1 - \frac{y^+}{\delta^+}, \tag{4.7}$$

where the Prandtl number (Pr) is $Pr = \nu/\alpha$. Differentiating Eq. (4.7) with respect to y^+ yields

$$\frac{1}{Pr}\frac{d^2\Theta^+}{dy^{+2}} + \frac{dT_\theta^+}{dy^+} + \epsilon^2 = 0, \tag{4.8}$$

where $T_\theta^+ = -\left\langle v^+\theta^+ \right\rangle$, and $\epsilon^2 = 1/\delta^+ = 1/Re_\tau$. These three terms are respectively

referred to as the molecular diffusion (MD), gradient of turbulent flux (GT), and heat generation (HG).

4.3 Empirical Observations

4.3.1 Four-layer leading balance structure

Previous studies of mean momentum transport revealed a four-layer structure based on the relative order of magnitude of the terms in the mean momentum equation (Wei et al., 2005a). To determine the relative size of terms, the ratio of the viscous force term (VF), i.e., $\partial^2 U^+/\partial y^{+2}$, to the turbulent inertia term (TI), i.e., $-\partial \langle uv \rangle^+ / \partial y^+$, was considered as a function of wall-normal position. The success of this approach motivates using same methodology to explore the leading order terms in Eq. (4.8), i.e., as was previously pursued by Wei et al. (2005b) and Saha et al. (2014). Here the ratio of the MD term to the GT term is under consideration. If this ratio is

$$|MD/GT| \ll 1, \tag{4.9}$$

then the MD term is small, and the GT and HG terms are nominally in balance. If

$$|MD/GT| \cong 1, \tag{4.10}$$

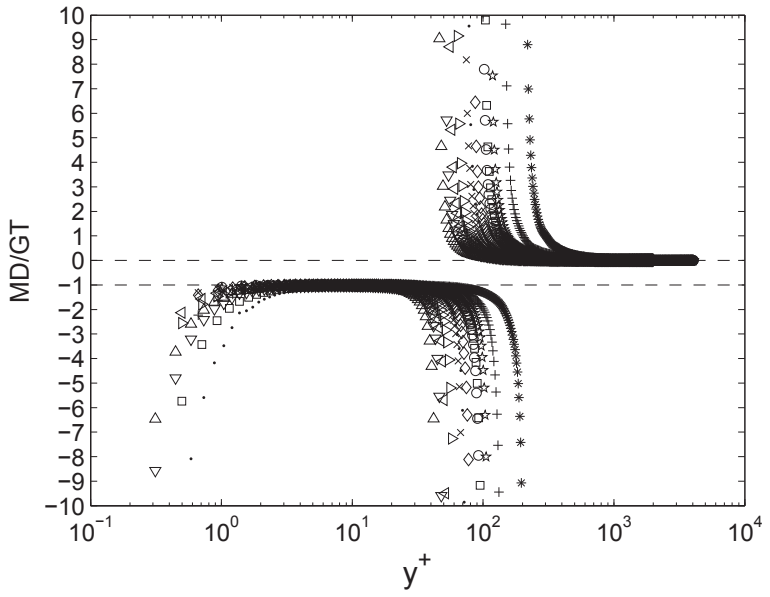

FIGURE 4.1: Ratio of the molecular diffusion term (MD) to the gradient of turbulent transport flux term (GT). DNS data are from Pirozzoli et al. (2016): $\triangle, \delta^+/Pr = 548$; $\bigtriangledown, \delta^+/Pr = 772$; $\triangleleft, \delta^+/Pr = 995$; $\triangleright, \delta^+/Pr = 1401$; $\times, \delta^+/Pr = 2017$; $\cdot, \delta^+/Pr = 2740$; $\diamond, \delta^+/Pr = 2841$; $\circ, \delta^+/Pr = 4088$; $\square, \delta^+/Pr = 4975$; $\star, \delta^+/Pr = 5758$; $+, \delta^+/Pr = 10085$; $*, \delta^+/Pr = 20440$.

then the HG term is either of the same order of magnitude or much smaller. Else, if

$$|MD/GT| \gg 1, \tag{4.11}$$

the GT term is small, and the MD and the HG terms approximately balance.

Direct numerical simulations that incorporate the constant heat generation term described in the analysis leading to Eq. (4.8) were conducted by Pirozzoli et al. (2016). Notably, these simulations cover a previously unrealized ranges of Prandtl and Reynolds numbers, $0.2 < Pr < 1$ and $550 < \delta^+ < 4080$. Ratio profiles covering this range are shown in Fig. 4.1 versus the inner-normalized distance from the wall. Consistent with

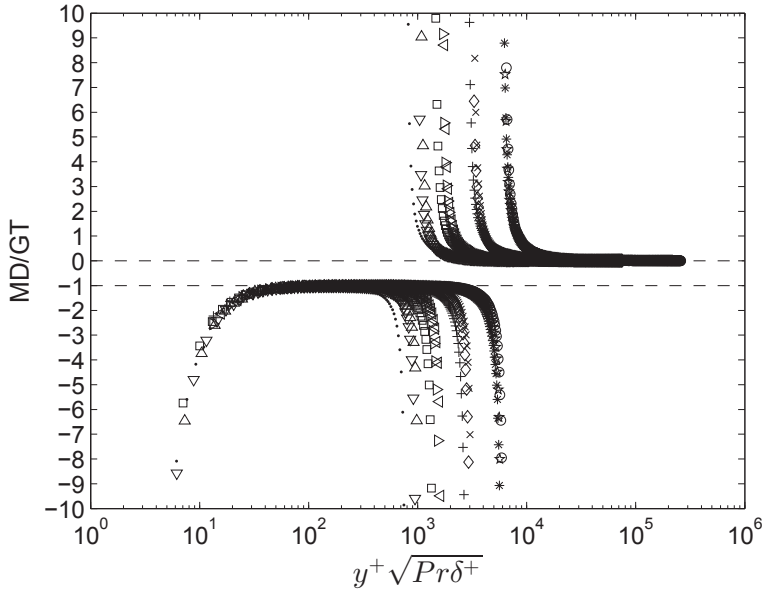

FIGURE 4.2: Ratio of the molecular diffusion term (MD) to the gradient of turbulent transport flux term (GT) versus $y^+\sqrt{Pr\delta^+}$. Symbols are the same as in Fig. 4.1.

the criterion used in the momentum balance analysis (Wei et al., 2005a), the ending position of layer I is where the ratio becomes greater than -2. The external bound layer II is determined where the ratio is less than -2, while that of layer III is based on where the ratio decreases below 0.5. Layer I lies close to the wall, $y^+ \lesssim 2$. In this domain, the leading balance is between the molecular diffusion (MD) and heat generation (HG) term.

4.3.2 Layer widths

The present profiles reveal that normalization of y using ν and u_τ (i.e., $y^+ = yu_\tau/\nu$) fails to produce an invariant profile of the heat flux gradient ratio in layer I for varying δ^+ and Pr. A length scale that characterizes the influence of Prandtl number is used in Fig. 4.2. A thermal inner length scale, i.e., $\sqrt{\nu^2\alpha/u_\tau^3\delta}$ is introduced here to normalize

the distance from the wall, and varying Pr and δ^+ appear to merge the profiles under this normalization.

Note here that the product of the Reynolds number and Prandtl number is the Peclet number, i.e., $Pe_\tau = Pr\delta^+$. The curve fit indicates that $y^+_{I\,end}$ varies with increasing $Pe_\tau^{-\frac{1}{2}}$. The leading coefficient is 16.69. Outside this near-wall layer, the ratio is approximately equal to -1, and this region (layer II) is characterized by a dominant balance between the MD and GT terms. With greater distance from the wall, the turbulent transport flux attains its maximum value, and about this location, all three terms attain equal order. As with the mean momentum field structure, there is an exchange of leading balance across layer III. Beyond this layer, the ratio decreases and gradually approaches 0, since the MD term becomes much smaller than either the GT or HG terms in the outer region (layer IV). Fig. 4.2 reveals that in layer III the ratio profiles nominally segregate into four groups of profiles depending on Reynolds number. This is consistent with the thermal inner-normalization, since for each Pr $y^+_{II\,end}\sqrt{Pr\delta^+}$ and $y^+_{III\,end}\sqrt{Pr\delta^+}$ only depend on Reynolds number.

The Reynolds and Prandtl number dependence of the inner-normalized external bounds of layers II and III are respectively shown in Fig. 4.3 and Fig. 4.4. Both $y^+_{II\,end}$ and $y^+_{III\,end}$ follow a linear trend with increasing $\sqrt{\delta^+/Pr}$. Curve fits give that the layer III is bounded between $y^+ \simeq 1.07\sqrt{\delta^+/Pr}$ and $y^+ \simeq 2.51\sqrt{\delta^+/Pr}$. However, if the curve fits are only applied to the data where $\sqrt{\delta^+/Pr} > 50$, since these data best approximate the high $\sqrt{\delta^+/Pr}$ condition, the layer III extends from $y^+ \simeq 1.04\sqrt{\delta^+/Pr}$ to $y^+ \simeq 2.50\sqrt{\delta^+/Pr}$. The effects of δ^+ and Pr on the heat flux gradient ratio act opposite to each other. An

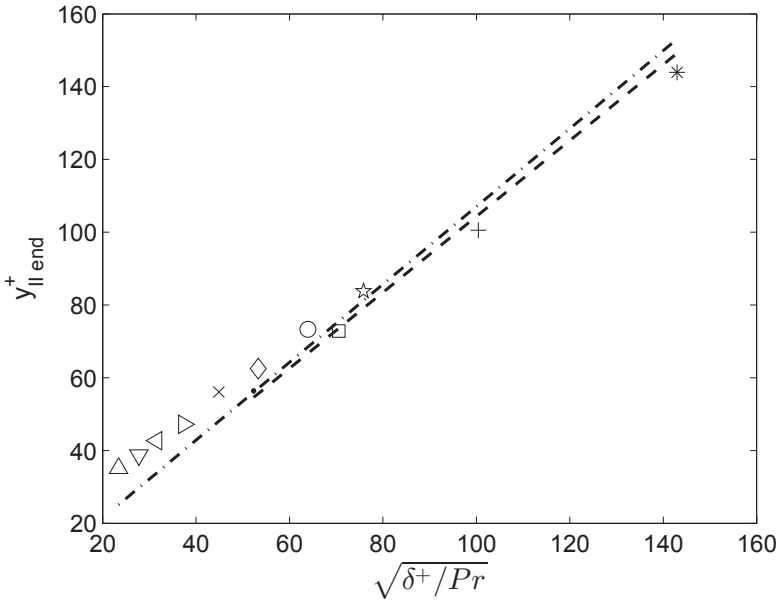

FIGURE 4.3: Reynolds and Prandtl number dependence of the external bound of layer II. Curve fit for all data (dashed-dotted line) is given by $y^+_{II\,end} = 1.07\sqrt{\delta^+/Pr}$. Curve fit for $\sqrt{\delta^+/Pr} > 50$ (dashed line) is given by $y^+_{II\,end} = 1.04\sqrt{\delta^+/Pr}$.

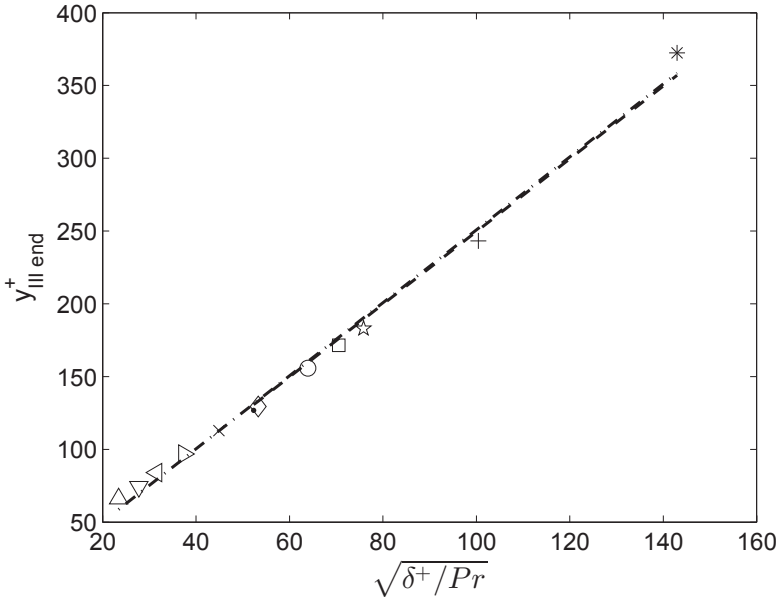

FIGURE 4.4: Reynolds and Prandtl number dependence of the external bound of layer III. Curve fit for all data (dashed-dotted line) is given by $y^+_{III\,end} = 2.51\sqrt{\delta^+/Pr}$. Curve fit for $\sqrt{\delta^+/Pr} > 50$ (dashed line) is given by $y^+_{III\,end} = 2.50\sqrt{\delta^+/Pr}$.

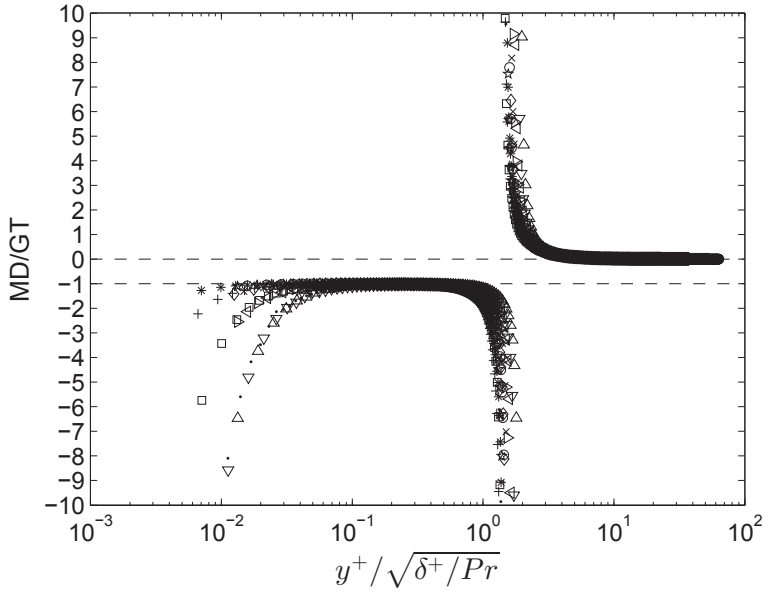

FIGURE 4.5: Ratio of the MD term to the GT term vs $y^+/\sqrt{\delta^+/Pr}$. Symbols are the same as in Fig. 4.1.

intermediate thermal length scale, $\sqrt{\delta\alpha/u_\tau}$, is characteristic of the heat transport layer III. Fig. 4.5 re-plots the data of Fig. 4.1 vs $y^+/\sqrt{\delta^+/Pr}$. The data of this figure suggest invariance under this normalization, with the estimated end points of layers II and III remaining nearly fixed when measured in units of $\sqrt{\delta^+/Pr}$.

4.3.3 Mean temperature increments

The mean scalar increments across each balance layer for each Prandtl number is determined as a function of Reynolds number. These results are shown in Fig. 4.6, Fig. 4.7 and Fig. 4.8. It is apparent that the mean temperature increment has a Prandtl number dependence. Under outer-normalization, the increment across layer II exhibits a decreasing variation, relative to the total increment, with increasing Reynolds number. The highest

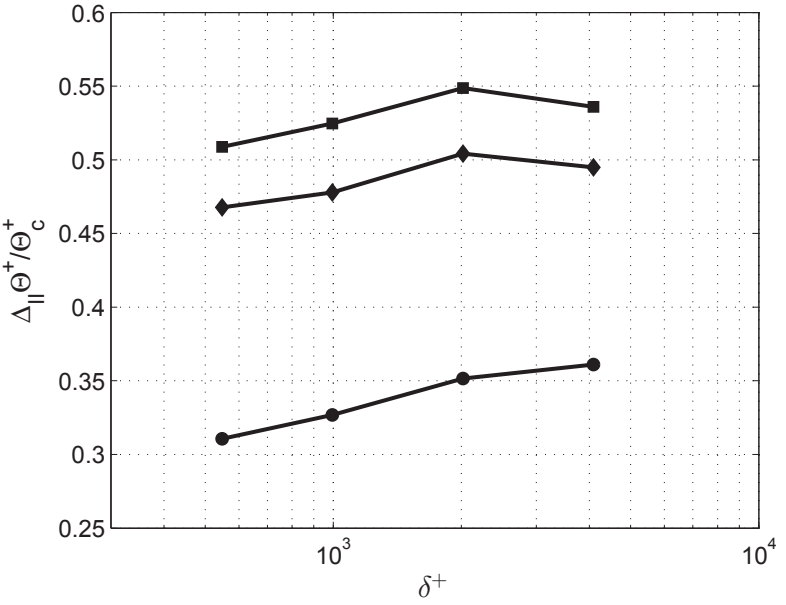

FIGURE 4.6: Ratio of the mean temperature increment across layer II to the mean centerline temperature. •, $Pr = 0.20$; ♦, $Pr = 0.71$; ■, $Pr = 1$. Θ_c is the mean temperature at the centerline.

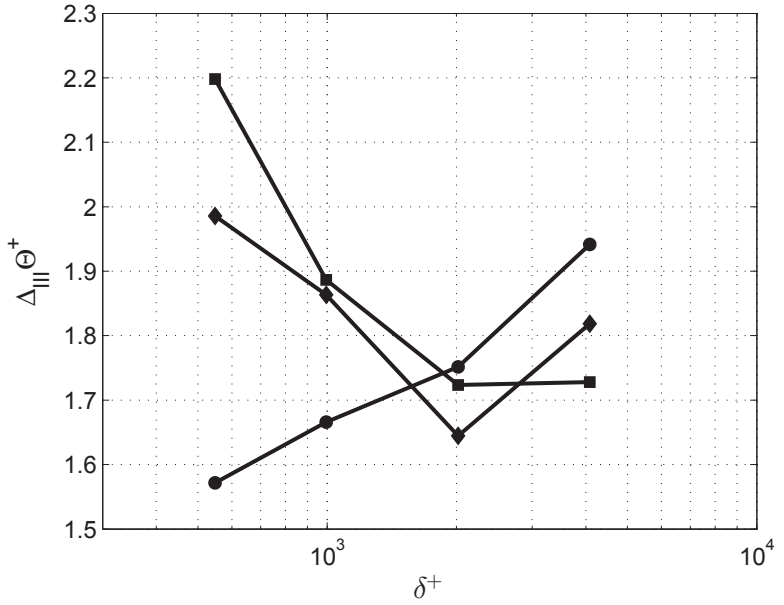

FIGURE 4.7: Inner-normalized mean temperature increment across layer III. •, $Pr = 0.20$; ♦, $Pr = 0.71$; ■, $Pr = 1$. Θ_c is the mean temperature at the centerline.

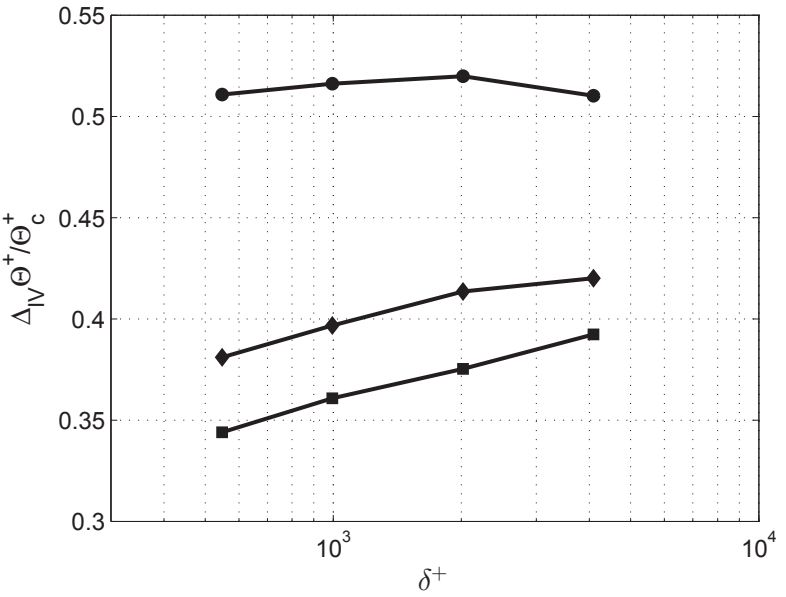

FIGURE 4.8: Ratio of the mean temperature increment across layer IV to the mean centerline temperature. $\bullet, Pr = 0.20$; $\blacklozenge, Pr = 0.71$; $\blacksquare, Pr = 1$. Θ_c is the mean temperature at the centerline.

Reynolds number values of the different curves are approximately 0.35, 0.5 and 0.55 for $Pr = 0.2$, 0.71 and 1, respectively. The present scaling theory predicts that these values should attain constancy at sufficiently high Reynolds number. The inner-normalized increments across layer III apparently remain $O(1)$ but exhibit a significant relative variation, with values ranging between 1.5 and 2.3. Under the present scaling theory, this temperature increment under this normalization is expected to attain invariance for any given Prandtl number at sufficiently high Reynolds number. Here it is worth noting that the layer III width grows like $\sqrt{\delta^+/Pr}$, that is not invariant with δ^+. Similar to the behavior in layer II, the outer-normalized mean temperature increment across layer IV shows significant variations with Reynolds number at each Prandtl number. Relative to the mean velocity increments associated with the mean momentum analysis, these layer IV increments are distinct. Namely, they show that the Prandtl number effect causes

them to exceed 0.5 for $Pr = 0.2$, while the layer IV velocity increment approaches 0.5 from below as $\delta^+ \to \infty$ (Wei et al., 2005a). As expected from the present theory, the inner-normalized mean temperature increments across layer I remain $O(1)$, and the inner-normalized mean temperature increments across both layers II and IV increase at a rate close to proportionality of Θ_c^+. Lastly, it is noted that similarly complex δ^+ and Pr trends are observed when the mean temperature increments are normalized by the bulk temperature instead of Θ_c^+.

4.4 Multiscale Analysis

A multiscale analysis of the mean scalar equation is now performed. There is no inherent limitation on the range of Pr for which the analysis applies. A central element of this analysis involves describing the scaling behaviors associated with the transitions between the leading balance layers. In this regard, the analysis of this section does not address the transition from layer II into layer I as $y^+ \to 0$. This is because the problem in this layer is insufficiently constrained to allow analytical determination of the stretching constants in the required transformations.

The primary focus below is thus on the scaling behaviors associated with layer III, which is the region where there is an exchange of balance that culminates with the loss of a leading order molecular diffusion (conduction) effect. The scaling properties of layer III are especially significant, as these properties are subsequently shown to replicate as a function of size with wall-normal distance across a self-similar hierarchy of well-defined

scaling layers. This layer hierarchy is then demonstrated to underlie the asymptotic emergence of a logarithmic mean temperature profile on the domain where molecular diffusion is negligible.

4.4.1 Rescaling across layer III

A multiscale analysis is now applied to mean scalar equation. For reasons to become apparent, a central element here is to analytically describe the scaling behaviors across layer III, as revealed by the above data presentation. Recall that across layer III all three terms have leading order contributions to the balance of Eq. (4.8). In this inner-normalized balance equation, however, the generation term is given by ϵ^2, and hence its *formal* order of magnitude is sub-dominant. A rescaling is sought that yields a parameter free form of Eq. (4.8) in which all three terms are $O(1)$ across layer III. And thus it yields a formal order of magnitude of each term that comports with their actual (empirically observed) order of magnitude. Based upon previous such analyses, only the y^+ and T_θ^+ variables require rescaling.

The process begins by setting

$$y^+ = y_{\theta m}^+ + \alpha \hat{y}, \quad T_\theta^+ = T_{\theta m}^+ + \beta \hat{T}_\theta, \tag{4.12}$$

where $y_{\theta m}^+$ is the position where T_θ^+ attains its maximum value, $T_{\theta m}^+$. This position provides a natural choice for the origin of the layer III rescaling since $y_{\theta m}^+$ necessarily

resides in layer III. The rescaled variables $\hat{y}$ and $\hat{T}$, which are equal to 0 at $y^+ = y^+_{\theta m}$, are independently $O(1)$ with the factors α and β to be determined in terms of ϵ and Pr.

Application of 4.12 transforms the first two terms in Eq. (4.8) as:

$$\frac{1}{Pr}\frac{d^2\Theta^+}{dy^{+2}} = \frac{1}{\alpha^2}\frac{1}{Pr}\frac{d^2\Theta^+}{d\hat{y}^2}, \quad \frac{dT^+_\theta}{dy^+} = \frac{\beta}{\alpha}\frac{d\hat{T}_\theta}{d\hat{y}}. \tag{4.13}$$

Both the derivatives on the right of (4.13) are $O(1)$. Now it is required that each term on the right of Eq. (4.8) match the third term in magnitude, i.e.,

$$\frac{1}{\alpha^2 Pr} = \frac{1}{\delta^+}, \quad \frac{\beta}{\alpha} = \frac{1}{\delta^+}. \tag{4.14}$$

This requires that

$$\alpha = \frac{1}{\epsilon\sqrt{Pr}}, \quad \beta = \frac{\epsilon}{\sqrt{Pr}}, \tag{4.15}$$

and thus

$$y^+ = y^+_{\theta m} + \frac{1}{\epsilon\sqrt{Pr}}\hat{y}, \quad T^+_\theta = T^+_{\theta m} + \frac{\epsilon}{\sqrt{Pr}}\hat{T}_\theta. \tag{4.16}$$

The variable representations given in Eq. (4.16) are valid in layer III, and here the mean balance equation becomes

$$\frac{d^2\Theta^+}{d\hat{y}^2} + \frac{d\hat{T}_\theta}{d\hat{y}} + 1 = 0. \tag{4.17}$$

Eq. (4.17) is a parameter-free form of the mean scalar equation in the layer III that faithfully reflects the empirical fact that each term is $O(1)$ in layer III.

4.4.2 Approach to asymptotic conditions in layer III

The variable stretching properties determined to construct the invariant form given by Eq. (4.17) allow testable predictions regarding the asymptotic properties of T_θ. In this regard, note that rearrangement of Eq. (4.7) gives

$$\frac{1}{Pr}\frac{d\Theta^+}{dy^+} = 1 - T_\theta^+ - \epsilon^2 y^+. \tag{4.18}$$

The three terms $\frac{1}{Pr}\frac{d\Theta^+}{dy^+}$, $\left(1 - T_\theta^+\right)$, and $\epsilon^2 y^+$ are thus of the same order of magnitude in this region. From Eq. (4.18) it is also seen that for any fixed Pr, $T_{\theta m}^+ \to 1$ as $\delta^+ \to \infty$.

From the fact that

$$\frac{1}{Pr}\frac{d\Theta^+}{dy^+} = \frac{\epsilon}{\sqrt{Pr}}\frac{d\Theta^+}{d\hat{y}}, \tag{4.19}$$

one finds that

$$1 - T_\theta^+ = (1 - T_{\theta m}^+) + (T_{\theta m}^+ - T_\theta^+) = \Delta - \frac{\epsilon}{\sqrt{Pr}}\hat{T}_\theta, \tag{4.20}$$

where Δ is a small quantity that constitutes the deviation of $T_{\theta m}^+$ from its asymptotic value of 1. Now, since $\hat{T}_\theta$ is by construction $O(1)$, $1 - T_\theta^+ = O(max[\Delta, \epsilon/\sqrt{Pr}])$, and the balance of these three terms requires that

$$max\left[\Delta, \frac{\epsilon}{\sqrt{Pr}}\right] = O\left(\frac{\epsilon}{\sqrt{Pr}}\right), \quad \epsilon^2 y^+ = O\left(\frac{\epsilon}{\sqrt{Pr}}\right). \tag{4.21}$$

Thus

$$\Delta \leqslant O\left(\frac{\epsilon}{\sqrt{Pr}}\right), \quad y^+ = O\left(\frac{1}{\epsilon\sqrt{Pr}}\right). \tag{4.22}$$

TABLE 4.1: Numerically determined Δ values. Data are from Pirozzoli et al. (2016).

$\delta^+ \, (Re_\tau)$	Pr	Δ	$\frac{\epsilon}{\sqrt{Pr}}$	$\Delta / \frac{\epsilon}{\sqrt{Pr}}$
548	0.20	0.2806	0.0955	2.9378
548	0.71	0.1591	0.0507	3.1375
548	1	0.1387	0.0427	3.2467
995	0.20	0.2068	0.0709	2.9166
995	0.71	0.1138	0.0376	3.0244
995	1	0.0979	0.0317	3.0873
2017	0.20	0.1458	0.0498	2.9288
2017	0.71	0.0767	0.0264	2.9029
2017	1	0.0652	0.0223	2.9285
4088	0.20	0.1022	0.0350	2.9232
4088	0.71	0.0534	0.0186	2.8788
4088	1	0.0452	0.0156	2.8870

These relations indicate that in layer III, y^+ is $O(1/\epsilon\sqrt{Pr})$, while T_θ^+ attains its maximum value $T_{\theta m}^+$ at $y_{\theta m}^+$. This implies that $y_{\theta m}^+ = O(1/\epsilon\sqrt{Pr})$, i.e., the analysis leads to a scaling for the peak position of the turbulent heat flux.

For the asymptotic approach of $T_{\theta m}^+ \to 1$, Eq. (4.18) is arranged and set $y^+ = y_{\theta m}^+$. This gives

$$\Delta = 1 - T_{\theta m}^+ = \frac{1}{Pr}\frac{d\Theta^+}{dy^+}(y_{\theta m}^+) + \epsilon^2 y_{\theta m}^+ \geqslant O\left(\frac{\epsilon}{\sqrt{Pr}}\right). \tag{4.23}$$

Combination of (4.22) and (4.23) yields

$$\Delta = O\left(\frac{\epsilon}{\sqrt{Pr}}\right). \tag{4.24}$$

The data of Table 4.1 support the analytically predicted behavior for Δ. Additionally the dependence of $y_{\theta m}^+$ on the combined influences of Pr and δ^+ are shown in Fig. 4.9. These results are also in accord with the present analyses. The curve fit on this figure

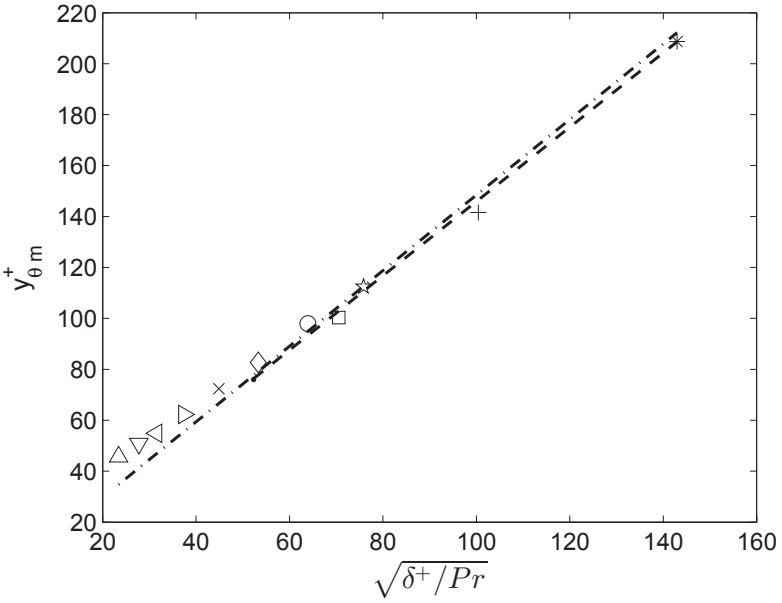

FIGURE 4.9: Maximum $T^+_{\theta m}$ position, $y^+_{\theta m}$, versus $\sqrt{\delta^+/Pr}$. Curve fit for all data (dashed-dotted line) is given by $y^+_{\theta m} = 1.48\sqrt{\delta^+/Pr}$. Curve fit for $\sqrt{\delta^+/Pr} > 50$ (dashed line) is given by $y^+_{\theta m} = 1.46\sqrt{\delta^+/Pr}$. Symbols are the same as in Fig. 4.1.

for all data is given by $y^+_{\theta m} = 1.48\sqrt{\delta^+/Pr}$. Curve fit for $\sqrt{\delta^+/Pr} > 50$ is given by $y^+_{\theta m} = 1.46\sqrt{\delta^+/Pr}$.

4.4.3 Mean temperature and turbulent flux scalings

The above analyses provide a rescaling for the turbulent heat flux that is formally valid for a $\hat{y} = O(1)$ domain nominally centered about $y^+_{\theta m}$. To explicitly see this, note that the finite transformations (4.12) shift the origin of the *hat* variables to this location. It is a straightforward matter, however, to verify that $d\hat{T}_\theta/d\hat{y} = dT^+_\theta/d\eta$, where $\eta = y/\delta$. Thus, the analysis predicts that, when plotted versus $\hat{y}$, the $\hat{T}_\theta$ scaling should hold from a position that begins on the wallward side of the peak in T^+_θ (by an amount that is $\hat{y} = O(1)$), and extends all the way to the channel centerline. Fig. 4.10 (b) provides

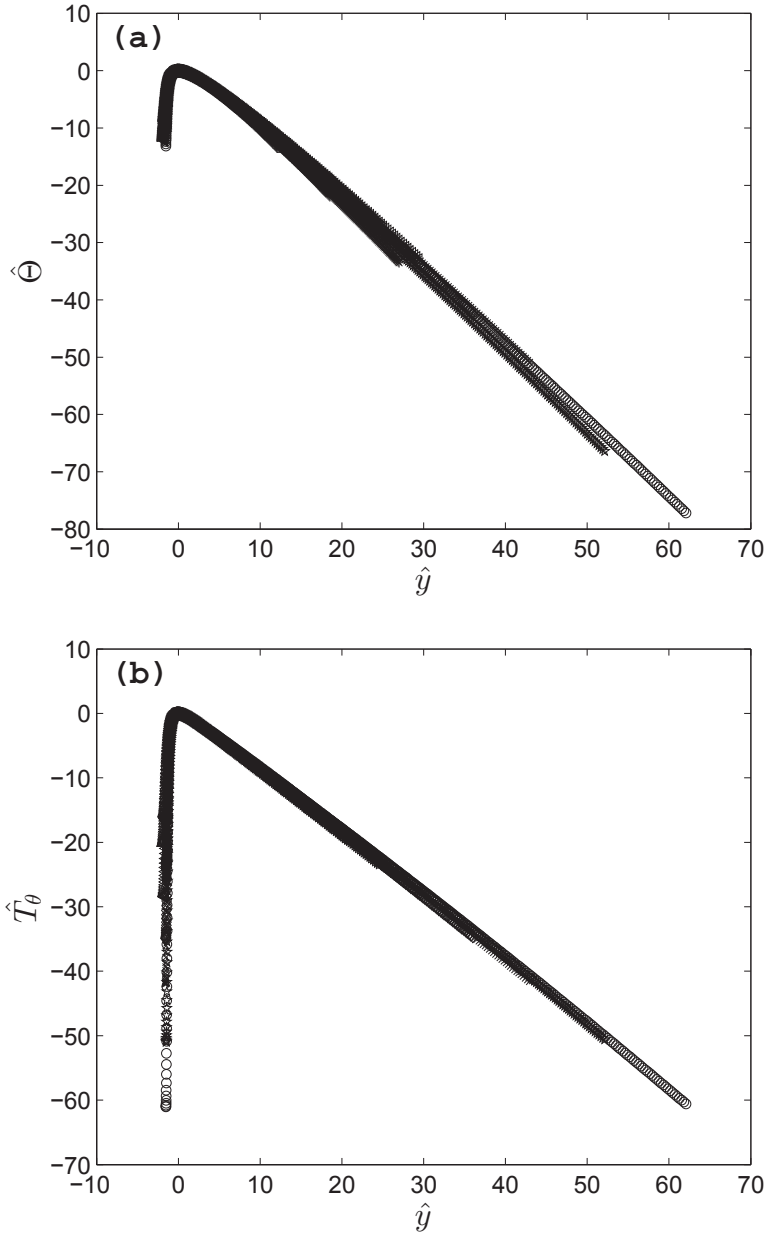

FIGURE 4.10: (a)Profiles of Θ normalzied by $\hat{\Theta}(\hat{y}) = \Theta^+ - \Theta(y^+_{\theta m}) - m(y^+ - y^+_{\theta m})$,where $m = (d\Theta^+/dy^+)(y^+ = y^+_{\theta m})$.(b)Profiles of T_θ normalized according to the variable scaling given by Eq. 4.16. Figure includes all Reynolds and Prandtl numbers from the study of Pirozzoli et al. (2016).

compelling evidence that this is indeed the case. Lastly, note that the scaling shows small be noticeable deviations as the wall is approached. This is because here the scaling associated with layer I becomes operative.

According to the scales in Eq. (4.16), the mean temperature Θ also admits an invariant scaling across layer III. That is, $\Theta^+ = \Theta^+(y^+_{\theta m}) + m(y^+ - y^+_{\theta m}) + \hat{\Theta}(\hat{y})$, where $m = (d\Theta^+/dy^+)(y^+ = y^+_{\theta m})$, and $\hat{\Theta}$ is $O(1)$ across layer III. This rescaled Θ should be valid across layer III over a range of $\hat{y} =\mid O(1) \mid$. The prediction is verified in Fig. 4.10 (a), where all $\hat{\Theta}$ curves merge together around $\hat{y} = 0$ within layer III. As anticipated, deviations from this scaling are observed as the wall and centerline are approached.

4.5 L_λ Layer Hierarchy

4.5.1 Hierarchy construction

The scaling properties associated with the four-layer structure for mean scalar equation have been empirically determined and analytically verified. As described above, the rescaling across layer III is central to determining these scaling behaviors. In a manner similar to what has been previously shown with regard to the mean momentum balance, it is now demonstrated that Eq. (4.17) can be written in an invariant form on each of a continuous hierarchy of finite width scaling layers, herein called the L_λ hierarchy. Significantly, each member of this layer hierarchy has a structure that mimics that of layer III.

To reveal the layer hierarchy a transformation is applied to T_θ^+

$$T_{\theta\lambda}^+ = T_\theta^+ + \epsilon^2 y^+ - \lambda y^+. \tag{4.25}$$

Here λ is treated as a small positive and constant parameter, i.e., like ϵ^2. This transformation allows the contribution to wall-normal transport by the turbulent scalar flux to be characterized as a function of scale with distance from the wall. Inserting it into Eq. (4.17) yields

$$\frac{1}{Pr}\frac{d^2\Theta^+}{dy^{+2}} + \frac{dT_{\theta\lambda}^+}{dy^+} + \lambda = 0, \tag{4.26}$$

which is still exact. Note that Eq. (4.26) takes on a form that looks like Eq. (4.17), but with the ϵ^2 term replaced by the λ term.

Concentration is applied to the domain where the GT term in Eq. (4.17) is monotonically decreasing. This region resides between a near-wall peak (at $y^+ \simeq 7$ for $Pr = 1$), and a maximally negative position near $y/\delta \simeq 0.5$ (essentially independent of Pr). From its definition, it is shown that for each λ value on this domain, $T_{\theta\lambda}^+$ attains a maximum value $T_{\theta\lambda m}^+$ at $y_{\theta\lambda m}^+$. For this construction, it is similarly shown that each λ value precisely corresponds to a specific wall normal location, for which there is a corresponding member of the layer hierarchy. Furthermore, on each of these layers Eq. (4.26) undergoes a balance breaking and exchange of terms analogous to what occurs across layer III. Thus, the scaling properties of each finite width layer on the hierarchy can be determined via the same mathematical procedure used for layer III.

Across each hierarchy layer, all three terms in Eq. (4.26) are of leading order. To reiterate, at $y^+ = y^+_{\theta\lambda m}$, it follows from (4.25) that

$$\frac{dT^+_{\theta\lambda}}{dy^+}\left(y^+_{\theta\lambda m}\right) = \frac{dT^+_{\theta}}{dy^+}\left(y^+_{\theta\lambda m}\right) + \epsilon^2 - \lambda = 0. \tag{4.27}$$

Rearrangement of Eq. (4.27) gives

$$\lambda = \frac{dT^+_{\theta}}{dy^+}\left(y^+_{\theta\lambda m}\right) + \epsilon^2. \tag{4.28}$$

Recognizing that each $y^+_{\theta\lambda m}$ uniquely corresponds to a y^+ position on the hierarchy, without loss of generality one can replace it with y^+. Eq. (4.27) then becomes

$$\lambda = \frac{dT^+_{\theta}}{dy^+} + \epsilon^2. \tag{4.29}$$

Thus, λ is determined from the gradient of turbulent transport flux term and the Reynolds number (heat generation term).

Now, to ensure that each value of λ uniquely corresponds to a single wall-normal position and associated scaling layer, i.e., $\lambda \xrightarrow{uniquely} y^+_{\theta\lambda m}$, λ must necessarily correspond to bounds between the inner and outer extreme values of dT^+_θ/dy^+. On this domain dT^+_θ/dy^+ decreases monotonically with increasing y. At any given Reynolds number, $y^+_{\theta\lambda m}$ increases as λ decreases. Fig. (4.11) and Fig. (4.12) show profiles of the turbulent transport flux term, and identify the range of $\lambda = dT^+_\theta/dy^+ + \epsilon^+$ positions that bound the hierarchy domain. It is now shown that within each hierarchy layer the variables

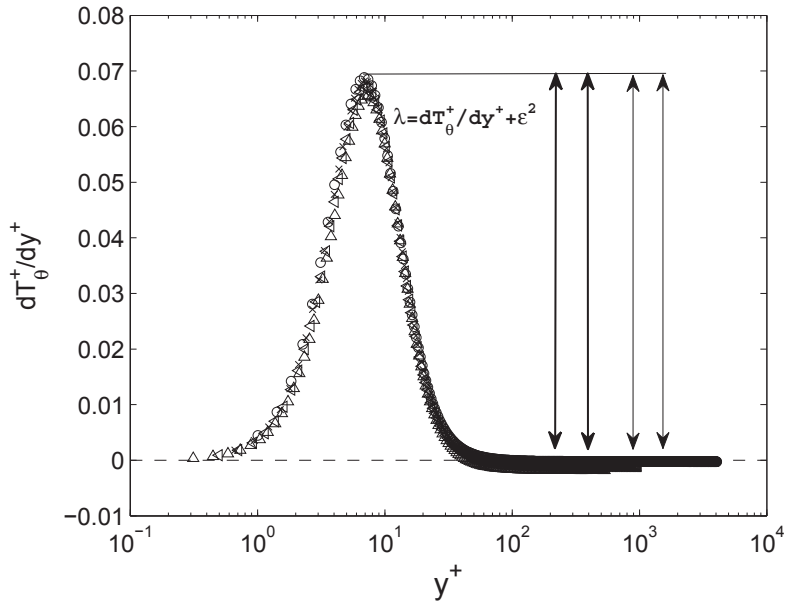

FIGURE 4.11: Profiles of dT_θ^+/dy^+ at $Pr = 1$: $\triangle, \delta^+ = 548$; $\triangleleft, \delta^+ = 995$; $\times, \delta^+ = 2017$; $\circ, \delta^+ = 4088$. Vertical double-arrows denote the range of dT_θ^+/dy^+ determining the value of λ for each case. The horizontal location of the arrows depends on where dT_θ^+/dy^+ attains its minimum value.

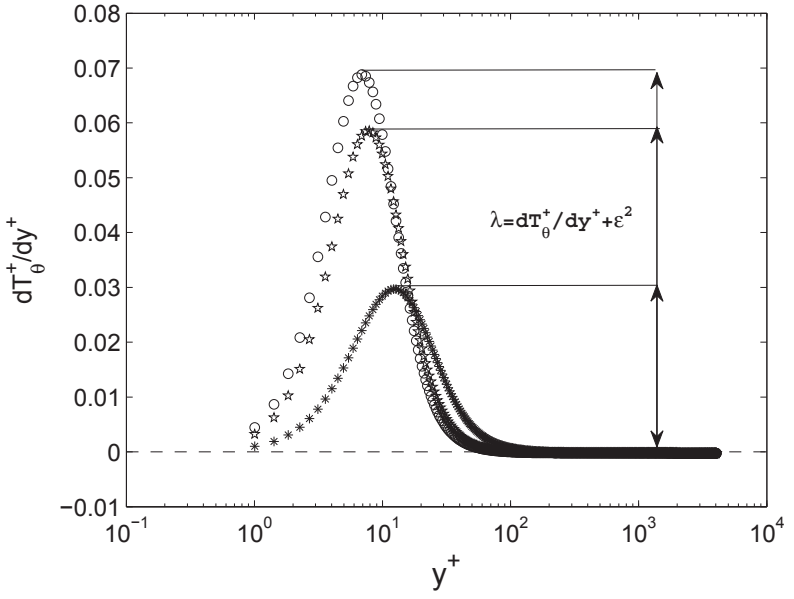

FIGURE 4.12: Profiles of dT_θ^+/dy^+ at $\delta^+ = 4088$: $\ast$, $Pr = 0.20$; $\star$, $Pr = 0.71$; $\circ, Pr = 1$. Vertical double-arrows denote the range of dT_θ^+/dy^+ determining the value of λ for each case. The horizontal location of the arrows depends on where dT_θ^+/dy^+ attains its minimum value.

y^+ and $T^+_{\theta\lambda}$ may be rescaled in such a way that the basic differential equation (4.26) is transformed into an exact equation having no explicit dependence on λ. As with layer III, rescaling is applied to $T^+_{\theta\lambda}$ and y^+ in such a way that all terms are $O(1)$ independent of λ. Here transformations are posed,

$$y^+ = y^+_{\theta\lambda m} + \zeta \hat{y}_{\theta\lambda}, \quad T^+_{\theta\lambda} = T^+_{\theta\lambda m} + \kappa \hat{T}_{\theta\lambda}, \tag{4.30}$$

and solve for the unknown variable stretching parameters, ζ and κ. Under these transformations Eq. (4.26) becomes

$$\frac{1}{\zeta^2}\frac{1}{Pr}\frac{d^2\Theta^+}{d\hat{y}^2_{\theta\lambda}} + \frac{\kappa}{\zeta}\frac{d\hat{T}_{\theta\lambda}}{d\hat{y}_{\theta\lambda}} + \lambda = 0. \tag{4.31}$$

The three terms in Eq. (4.31) are required to be of the same order of magnitude, which means

$$\frac{1}{\zeta^2}\frac{1}{Pr} = \lambda, \quad \frac{\kappa}{\zeta} = \lambda. \tag{4.32}$$

From these constraints it is apparent that

$$\zeta = \frac{1}{\sqrt{\lambda Pr}}, \quad \kappa = \sqrt{\frac{\lambda}{Pr}}, \tag{4.33}$$

and therefore,

$$y^+ = y^+_{\theta\lambda m} + \frac{1}{\sqrt{\lambda Pr}}\hat{y}_{\theta\lambda}, \quad T^+_{\theta\lambda} = T^+_{\theta\lambda m} + \sqrt{\frac{\lambda}{Pr}}\hat{T}_{\theta\lambda}. \tag{4.34}$$

Under these transformations, Eq. (4.26) takes on an invariant form

$$\frac{d^2\Theta^+}{d\hat{y}^2_{\theta\lambda}} + \frac{d\hat{T}_{\theta\lambda}}{d\hat{y}_{\theta\lambda}} + 1 = 0, \tag{4.35}$$

that is operative on every layer of the L_λ hierarchy.

4.5.2 Hierarchy layer width scaling

As was done for layer III, analytical description of the layer widths of the L_λ hierarchy is explored. From (4.34), the inner-normalized width of each hierarchy layer is $O(1/\sqrt{\lambda Pr})$. This width is a central element of the hierarchy structure, since it physically characterizes the size of the motions responsible for scalar transport, and is mathematically related to the underlying similarity structure of the mean scalar equation. This length is formally defined as the function W^+_θ

$$W^+_\theta = O(\lambda^{-\frac{1}{2}} Pr^{-\frac{1}{2}}), \tag{4.36}$$

but $\lambda^{-\frac{1}{2}} Pr^{-\frac{1}{2}}$ can be used to calculate the W^+_θ without loss of generality. In Eq. (4.25), setting $y^+ = y^+_{\theta\lambda m}$ yields

$$\lambda = \frac{\partial T^+_\theta}{\partial y^+}(y^+_{\theta\lambda m}) + \epsilon^2 = -\frac{1}{Pr}\frac{\partial^2\Theta^+}{\partial y^{+2}}(y^+_{\theta\lambda m}), \tag{4.37}$$

As before, it is noted that $y^+_{\theta\lambda m}$ uniquely corresponds to y^+ on the hierarchy, and thus can be replaced by y^+. Combination of (4.36) and (4.37) results in the best way to evaluate

TABLE 4.2: Inner and outer edges of the L_λ hierarchy.

$\delta^+ (Re_\tau)$	Pr	$y^+_{\theta ip}$	$y^+_{\theta op}/\delta^+$
548	0.20	13.0361	0.6643
548	0.71	8.1616	0.6533
548	1	7.2725	0.6533
995	0.20	12.8296	0.6848
995	0.71	8.0550	0.6838
995	1	7.1743	0.6828
2017	0.20	12.6361	0.7208
2017	0.71	7.9136	0.7208
2017	1	7.0501	0.7208
4088	0.20	12.4574	0.7107
4088	0.71	7.7977	0.7170
4088	1	6.9649	0.7178

W^+_θ from DNS data

$$W^+_\theta = \left(-\frac{d^2\Theta^+}{dy^{+2}} \right)^{-\frac{1}{2}}. \tag{4.38}$$

Physically, $W^+_\theta(y^+)$ is recognized as the average size of the motions responsible for the net wallward flux of heat from layer to layer, or, equivalently, it is the average size of the motions responsible for the generation of turbulent transport flux, i.e., T^+_θ. The inner ($y^+_{\theta ip}$) and outer ($y^+_{\theta op}$) edges of the layer hierarchy correspond to where the W^+_θ profile respectively attains its minimum and maximum values, since

$$\frac{dW^+_\theta}{dy^+} = -\frac{1}{2}\frac{1}{\sqrt{\lambda^3 Pr}}\frac{d^2T^+_\theta}{dy^{+2}}. \tag{4.39}$$

The values of $y^+_{\theta ip}$ and $y^+_{\theta op}$ for various δ^+ and Pr are listed in Table (4.2), while Fig. (4.13) and Fig. (4.14) show distributions of W^+_θ. Note that the Prandtl number only has apparent effects on the domain interior to layer IV. All of the W^+_θ profiles

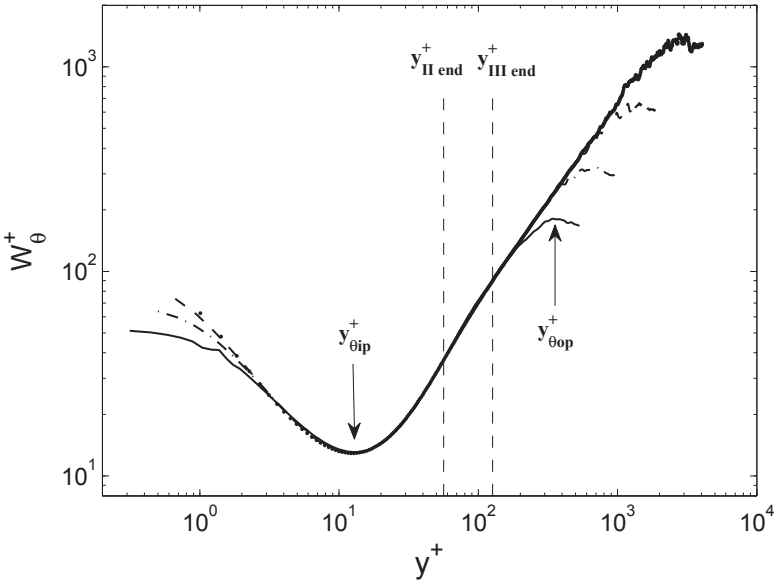

FIGURE 4.13: Distribution of W_θ^+. Solid line: $\delta^+ = 548, Pr = 0.20$. Dashed-dotted line: $\delta^+ = 995, Pr = 0.20$. Dashed line: $\delta^+ = 2017, Pr = 0.20$. Dotted line: $\delta^+ = 4088, Pr = 0.20$. Vertical dashed lines respectively denote the internal and external bounds of layer III as computed for $\delta^+ = 548, Pr = 0.20$.

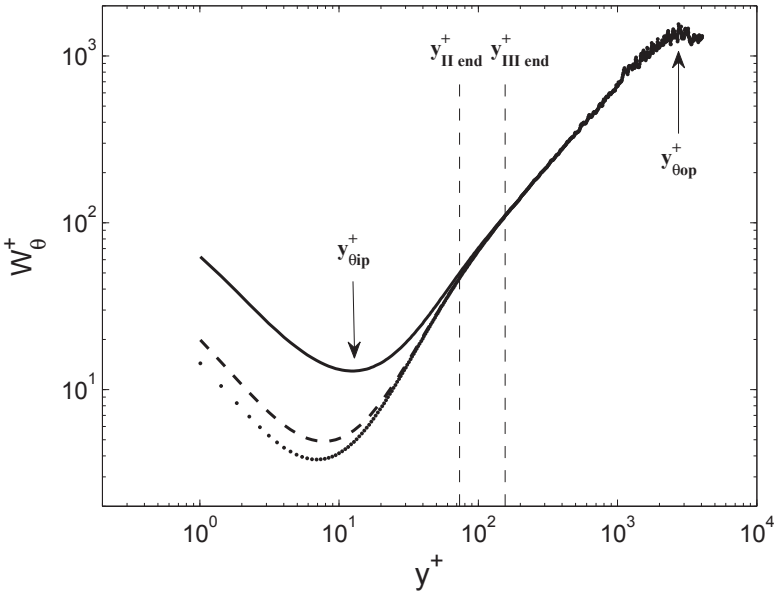

FIGURE 4.14: Distribution of W_θ^+. Solid line: $\delta^+ = 4088, Pr = 0.20$. Dashed line: $\delta^+ = 4088, Pr = 0.71$. Dotted line: $\delta^+ = 4088, Pr = 1$.Vertical dashed lines respectively denote the internal and external bounds of layer III as computed for $\delta^+ = 4088, Pr = 1$.

in Fig. (4.13) and Fig. (4.14) merge onto a single profile beyond the external bound of layer III, and remain as such until near the end of the hierarchy for each flow. In accord with the present theory, on this domain W_θ^+ becomes increasingly well-approximated by a linear function of y^+, with the accuracy of this linear approximation increasing with δ^+. On this portion of the hierarchy (i.e., $y^+ \gtrsim 2.5\sqrt{\delta^+/Pr}$) the gradient of turbulent transport flux and heat generation terms form the leading order balance.

4.5.3 Self-similarity

The analytical results pertaining to the invariant form of the mean scalar equation (Eq. 4.35) on the layer IV portion of the L_λ hierarchy are directly associated with the logarithmic dependence of the mean temperature profile. Clarification is conducted now that this invariance is associated with a self-similar structure that is reflected in the curvature of the T_θ^+ profile, or equivalently the linearity of the W_θ^+ profile. From Eq. (4.25),

$$\frac{dT_\theta^+}{dy^+}\left(y_{\theta\lambda m}^+\right) + \epsilon^2 - \lambda = 0. \tag{4.40}$$

Differentiating Eq. (4.40) with respect to λ gives

$$\frac{d^2T_\theta^+}{dy^{+2}}\frac{dy_{\theta\lambda m}^+}{d\lambda} - 1 = 0, \tag{4.41}$$

and from (4.34)

$$\frac{d^2T_\theta^+}{dy^{+2}} = \sqrt{\lambda^3 Pr}\frac{d^2\hat{T}_{\theta\lambda}}{d\hat{y}_{\theta\lambda}^2}. \tag{4.42}$$

The underlying theory indicates that the condition for a self-similarity from layer to layer on the hierarchy is that

$$A_\theta = -\frac{d^2\hat{T}_{\theta\lambda}}{d\hat{y}^2_{\theta\lambda}} = -\frac{d^2T^+_\theta}{dy^{+2}}\lambda^{-\frac{3}{2}}Pr^{-\frac{1}{2}} = -\frac{d^2T^+_\theta}{dy^{+2}}\left(\frac{dT^+_\theta}{dy^+}+\epsilon^2\right)^{-\frac{3}{2}}Pr^{-\frac{1}{2}} = -\frac{d^2T^+_\theta}{dy^{+2}}\left(-\frac{d^2\Theta^+}{dy^{+2}}\right)^{-\frac{3}{2}}Pr \tag{4.43}$$

approaches constancy for any fixed Pr as $\delta^+ \to \infty$. This condition stems from the fact that the only means to interrupt the self similar behavior on the hierarchy is through *edge effects* acting at its periphery. Thus, as δ^+ becomes large the number of layers on the hierarchy increases, and those on its interior become increasingly insulated from these edge effects. Differentiating and rearranging Eq. (4.8) gives

$$-\frac{d^2T^+_\theta}{dy^{+2}} = \frac{1}{Pr}\frac{d^3\Theta^+}{dy^{+3}}, \tag{4.44}$$

and thus Eq. (4.43) becomes

$$A_\theta = \frac{d^3\Theta^+}{dy^{+3}}\left(-\frac{d^2\Theta^+}{dy^{+2}}\right)^{-\frac{3}{2}}. \tag{4.45}$$

Following Klewicki et al. (2009); Klewicki (2013b), it is now identified that

$$\phi_\theta = \frac{dy^+}{dW^+_\theta}. \tag{4.46}$$

Mathematically, ϕ_θ is the stretching of the y coordinate required to produce the invariant form given by Eq. (4.35). Furthermore from (4.39) and (4.43) one can show that

$$\frac{dW_\theta^+}{dy^+} = \frac{A_\theta}{2}, \tag{4.47}$$

and therefore A_θ and W_θ are related by

$$\frac{dW_\theta^+}{dy^+} = \frac{A_\theta}{2} = \frac{1}{\phi_\theta}. \tag{4.48}$$

Owing to the properties of A_θ just described, over an interior domain within the L_λ hierarchy where the molecular diffusion term loses its leading order, ϕ_θ, which is necessarily $O(1)$, approaches a constant, $\phi_{\theta c}$, as $\delta^+ \to \infty$.

4.5.4 Logarithmic dependence

The invariance properties described above provide a basis for constructing a similarity solution for the mean temperature on the domain where $\phi_\theta \to \phi_{\theta c}$. Here, (4.45) is written as

$$\frac{2}{\phi_{\theta c}} = \frac{d^3\Theta^+}{dy^{+3}} \left(-\frac{d^2\Theta^+}{dy^{+2}} \right)^{-\frac{3}{2}}. \tag{4.49}$$

Eq. (4.49) is a ordinary differential equation with a single unknown, Θ^+.

Following Klewicki and Oberlack Klewicki and Oberlack (2015), setting $f_\theta = -\frac{d^2\Theta^+}{dy^{+2}}$ yields

$$\frac{df_\theta}{dy^+} = -\frac{2}{\phi_{\theta c}} f_\theta^{\frac{3}{2}}. \tag{4.50}$$

Separating variables and integrating gives

$$f_\theta = -\frac{d^2\Theta^+}{dy^{+2}} = \phi_{\theta c}^2 \left(y^+ - C_1\right)^{-2}, \tag{4.51}$$

and two more integrations yield

$$\Theta^+ = \phi_{\theta c}^2 \, ln\left(y^+ - C_1\right) + C_2 y^+ + C_3. \tag{4.52}$$

In Eq. (4.52) $\phi_{\theta c}^2$ is usually written as $1/k_\theta$, where k_θ is the scalar Kármán constant. Eq. (4.52) adheres to the classic logarithmic variation, but with an additive linear term and an offset in the logarithmic argument. The offset C_1 is empirically set to be 0, since it is much smaller than the distance from the wall where the logarithmic dependence begins, i.e., the onset of layer IV, $y^+ \simeq 2.5\sqrt{\delta^+/Pr}$. In the analogous momentum case the offset in the velocity log law is estimated be between ± 7 viscous lengths, Klewicki (2013b).

In the lower part of layer IV, Eq. (4.48) becomes

$$\frac{dW_\theta^+}{dy^+} = \frac{1}{\phi_{\theta c}}. \tag{4.53}$$

TABLE 4.3: Slope of W_θ^+, scalar Karman constant k_θ and Curve-fit coefficients in (4.52) for $C_1 = 0$

$\delta^+\,(Re_\tau)$	Pr	$\frac{dW_\theta^+}{dy^+}$	$\left(\frac{dW_\theta^+}{dy^+}\right)^2$	k_θ	C_2	C_3
548	0.20	0.6857	0.4702	0.5202	2.9603×10^{-3}	-2.2018
548	0.71	0.7438	0.5533	0.4724	1.6420×10^{-3}	3.6422
548	1	0.7544	0.5692	0.4609	1.2204×10^{-3}	6.2077
995	0.20	0.6731	0.4530	0.5037	1.7050×10^{-3}	-2.4381
995	0.71	0.7156	0.5121	0.5007	1.5442×10^{-3}	4.0651
995	1	0.7250	0.5256	0.4966	1.4386×10^{-3}	6.7364
2017	0.20	0.6293	0.3960	0.4796	8.2534×10^{-4}	-2.8648
2017	0.71	0.6627	0.4391	0.4945	8.9567×10^{-4}	3.9169
2017	1	0.6677	0.4459	0.4964	8.9830×10^{-4}	6.6601
4088	0.20	0.6824	0.4657	0.4502	2.2988×10^{-4}	-3.5559
4088	0.71	0.6782	0.4599	0.4705	3.1904×10^{-4}	3.3615
4088	1	0.6789	0.4609	0.4755	3.4528×10^{-4}	6.1612

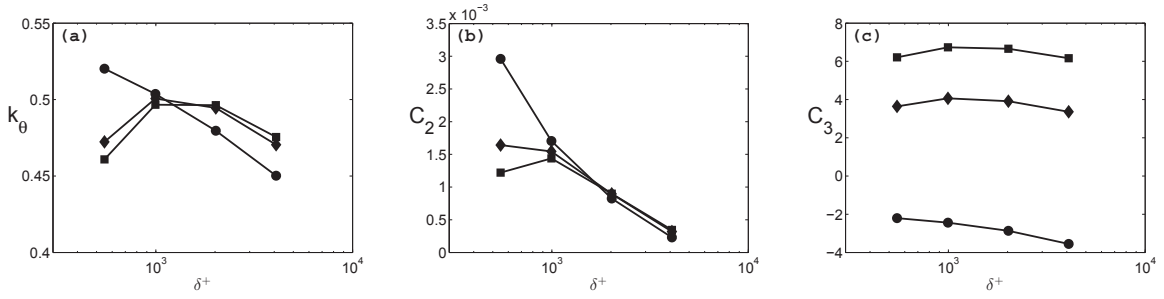

FIGURE 4.15: Curve-fit coefficients in (4.52) for $C_1 = 0$ versus δ^+. (a)$k_\theta = \phi_{\theta c}^{-2}$. (b)$C_2$. (c)$C_3$. •, $Pr = 0.20$; ♦, $Pr = 0.71$; ■, $Pr = 1$.

Therefore,

$$\left(\frac{dW_\theta^+}{dy^+}\right)^2 = k_\theta. \tag{4.54}$$

Both W_θ^+ and Θ^+ profile data are fitted from the external bound of layer III to $y/\delta = 0.3$ so as to respectively explore the value of $\left(\frac{dW_\theta^+}{dy^+}\right)$, k_θ, C_2 and C_3. These values are listed in Table (4.3) and presented in Fig. (4.15). The maximum deviation of the W_θ^+ data points from the linear fit is less than 10%, while that of the Θ^+ from the logarithmic fit is less than 0.07%. It is noted that the value of $\left(\frac{dW_\theta^+}{dy^+}\right)^2$ appears to asymptotically approach

TABLE 4.4: Curve-fit coefficients in (4.52) with $\phi_{\theta c}^{+}$ set to the corresponding $\left(dW_{\theta}^{+}/dy^{+}\right)^{-2}$ value and for $C_1 = 0$.

$\delta^{+}\,(Re_{\tau})$	Pr	C_2	C_3
548	0.20	1.5404×10^{-3}	-3.0122
548	0.71	4.3528×10^{-3}	4.7922
548	1	5.0162×10^{-3}	7.7168
995	0.20	7.4601×10^{-4}	-3.4221
995	0.71	1.7860×10^{-3}	4.2498
995	1	2.0852×10^{-3}	7.1894
2017	0.20	-2.7122×10^{-4}	-5.0488
2017	0.71	8.5220×10^{-5}	2.7291
2017	1	1.4187×10^{-4}	5.6110
4088	0.20	3.3172×10^{-4}	-3.1475
4088	0.71	2.3420×10^{-4}	3.1072
4088	1	2.2125×10^{-4}	5.8207

that of k_{θ}, while C_2 tends to zero with increasing δ^{+}. This second result is anticipated from the $y^{+} \to \infty$ boundary condition on $d\Theta^{+}/dy^{+}$. Prandtl number has a remarkable effect on C_3, and for each value of Pr, C_3 seems to gradually approach a constant with increasing Reynolds number. All of the k_{θ} values estimated from the curve fit exceed 0.45. These values are consistent with the estimates of Pirozzoli et al. (2016), $k_{\theta} \simeq 0.46$. This scalar Kármán constant is greater than the Kármán constant, which asymptotically approaches something close to 0.39 as $\delta^{+} \to \infty$, e.g., see Klewicki and Oberlack (2015).

To investigate the internal self-consistency of the present analyses, another curve-fit was also applied to (4.52). In this case the value of $\phi_{\theta c}^{2}$ was set by the corresponding value of $\left(\frac{dW_{\theta}^{+}}{dy^{+}}\right)^{-2}$. Over all of the profiles examined, the maximum deviation from this logarithmic fit is less than 0.39%. The coefficient values associated with this case are listed in Table (4.4), and shown in Fig. (4.16). Analogous to the previous curve-fit, C_2 is characterized by a diminishing behavior, and C_3 varies towards a constant value

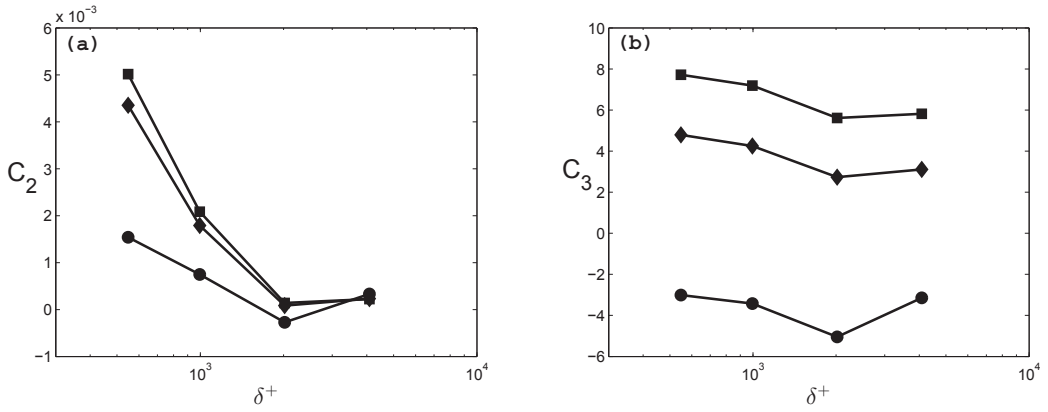

FIGURE 4.16: Curve-fit coefficients in (4.52) with $\phi^+_{\theta c}$ set to the corresponding $\left(dW^+_\theta/dy^+\right)^{-2}$ value and for $C_1 = 0$ versus δ^+. (a)C_2. (b)C_3. •, $Pr = 0.20$; ♦, $Pr = 0.71$; ■, $Pr = 1$.

for each Prandtl number. Overall, like the analogous momentum equation analysis, the present scalar results suggest that the standard logarithmic law (i.e., with zero offset and single additive constant) naturally arises as an asymptotic condition of the more general expression given by Eq. (4.52).

4.6 Scalar Variance Analysis

4.6.1 Basic equation

The time-averaged mean scalar variance and turbulence scalar variance equations respectively are

$$\frac{\partial}{\partial t}\left(\frac{1}{2}\Theta^2\right) + U_j\frac{\partial}{\partial x_j}\left(\frac{1}{2}\Theta^2\right) + \Theta\frac{\partial}{\partial x_j}\left\langle u_j\theta\right\rangle = \alpha\frac{\partial^2}{\partial x_j\partial x_j}\left(\frac{1}{2}\Theta^2\right) - \alpha\left\langle\frac{\partial\Theta}{\partial x_j}\frac{\partial\Theta}{\partial x_j}\right\rangle + \Theta Q, \tag{4.55}$$

and

$$\frac{\partial}{\partial t}\left\langle \frac{1}{2}\theta^2 \right\rangle + U_j \frac{\partial}{\partial x_j}\left\langle \frac{1}{2}\theta^2 \right\rangle + \langle u_j\theta \rangle \frac{\partial \Theta}{\partial x_j} + \frac{\partial}{\partial x_j}\left\langle u_j \frac{1}{2}\theta^2 \right\rangle = \alpha \frac{\partial^2}{\partial x_j \partial x_j}\left\langle \frac{1}{2}\theta^2 \right\rangle - \alpha \left\langle \frac{\partial \theta}{\partial x_j}\frac{\partial \theta}{\partial x_j} \right\rangle. \tag{4.56}$$

Same as the previous mean scalar analysis, Θ is the mean temperature and θ is the corresponding fluctuating temperature (and similarly for the velocity components), α is the thermal diffusivity, and Q is the unit heat generation. The condition of a statistically stationary steady flow yields

$$\frac{\partial}{\partial t}\left(\frac{1}{2}\Theta^2\right) = 0; \tag{4.57}$$

$$\frac{\partial}{\partial t}\left\langle \frac{1}{2}\theta^2 \right\rangle = 0. \tag{4.58}$$

The fully-developed condition and $V = 0$ give

$$U_i \frac{\partial}{\partial x_j}\left(\frac{1}{2}\Theta^2\right) = 0; \tag{4.59}$$

$$U_i \frac{\partial}{\partial x_j}\left\langle \frac{1}{2}\theta^2 \right\rangle = 0; \tag{4.60}$$

$$\Theta \frac{\partial}{\partial x_j}\langle u_j\theta \rangle = \Theta \frac{d}{dy}\langle v\theta \rangle; \tag{4.61}$$

$$\langle u_j\theta \rangle \frac{\partial \Theta}{\partial x_j} = \langle v\theta \rangle \frac{d\Theta}{dy}; \tag{4.62}$$

$$\alpha \frac{\partial^2}{\partial x_j \partial x_j}\left(\frac{1}{2}\Theta^2\right) = \frac{d^2}{dy^2}\left(\frac{1}{2}\Theta^2\right); \tag{4.63}$$

$$\frac{\partial}{\partial x_j}\left\langle u_j \frac{1}{2}\theta^2 \right\rangle = \frac{d}{dy}\left\langle v \frac{1}{2}\theta^2 \right\rangle; \tag{4.64}$$

$$-\alpha\left\langle\frac{\partial\Theta}{\partial x_j}\frac{\partial\Theta}{\partial x_j}\right\rangle=-\alpha\left\langle\frac{d\Theta}{dy}\frac{d\Theta}{dy}\right\rangle \tag{4.65}$$

and

$$\alpha\frac{\partial^2}{\partial x_j\partial x_j}\left\langle\frac{1}{2}\theta^2\right\rangle=\alpha\frac{d^2}{dy^2}\left\langle\frac{1}{2}\theta^2\right\rangle. \tag{4.66}$$

Combination and rearrangement of (4.57), (4.59), (4.61), (4.63) and (4.64) give the simplified form of the mean scalar variance equation for turbulent channel flow

$$\frac{d^2}{dy^2}\left(\frac{1}{2}\Theta^2\right)-\Theta\frac{d}{dy}\langle v\theta\rangle-\alpha\left\langle\frac{d\Theta}{dy}\frac{d\Theta}{dy}\right\rangle+\Theta Q=0. \tag{4.67}$$

Combination and rearrangement of (4.58), (4.60), (4.62), (4.64) and (4.66) give the simplified form of the turbulence scalar variance equation for turbulent channel flow

$$-\frac{d}{dy}\left\langle v\frac{1}{2}\theta^2\right\rangle+\alpha\frac{d^2}{dy^2}\left\langle\frac{1}{2}\theta^2\right\rangle-\langle v\theta\rangle\frac{d\Theta}{dy}-\alpha\left\langle\frac{\partial\theta}{\partial x_j}\frac{\partial\theta}{\partial x_j}\right\rangle=0. \tag{4.68}$$

Inner-normalization is applied to each term in Eq. (4.67) and Eq. (4.68) with the friction temperature, i.e., $\theta_\tau=\frac{\alpha}{u_\tau}\frac{d\Theta}{dy}|_{wall}$, u_τ and ν.

$$\Theta^+=\frac{\Theta}{\theta_\tau},\quad \theta^+=\frac{\theta}{\theta_\tau},\quad v^+=\frac{v}{u_\tau},\quad -\left\langle v^+\theta^+\right\rangle=-\frac{v\theta}{u_\tau\theta_\tau},\quad y^+=\frac{yu_\tau}{\nu}. \tag{4.69}$$

The inner-normalized Eq. (4.67) becomes

$$\frac{1}{Pr}\frac{d^2}{dy^{+2}}\left(\frac{1}{2}\Theta^{+2}\right)-\Theta^+\frac{d}{dy^+}\left\langle v^+\theta^+\right\rangle-\frac{1}{Pr}\frac{d\Theta^+}{dy^+}\frac{d\Theta^+}{dy^+}+\Theta^+\frac{1}{\delta^+}=0. \tag{4.70}$$

These four terms are respectively referred to as mean molecular transport (MMT), product gradient of turbulent flux (PGT), mean dissipation (MD) and product heat generation (PG).

The inner-normalized Eq. (4.68) becomes

$$-\frac{d}{dy^+}\left\langle v^+\frac{1}{2}\theta^{+2}\right\rangle+\frac{1}{Pr}\frac{d^2}{dy^{+2}}\left\langle\frac{1}{2}\theta^{+2}\right\rangle-\left\langle v^+\theta^+\right\rangle\frac{d\Theta^+}{dy^+}-\frac{1}{Pr}\left\langle\frac{\partial\theta^+}{\partial x_j^+}\frac{\partial\theta^+}{\partial x_j^+}\right\rangle=0, \quad (4.71)$$

These four terms are respectively referred to as turbulent diffusion (TD), turbulent molecular transport (TMT), gradient production (GP) and turbulent dissipation (TD).

Combination of Eq. (4.70) and Eq. (4.71) gives the inner-normalized total scalar variance equation

$$\begin{aligned}&\frac{1}{Pr}\frac{d^2}{dy^{+2}}\left[\frac{1}{2}\Theta^{+2}+\left\langle\frac{1}{2}\theta^{+2}\right\rangle\right]+\frac{d}{dy^+}\left[\Theta^+T_\theta^+-\left\langle v^+\frac{1}{2}\theta^{+2}\right\rangle\right]\\&\quad+\left[-\frac{1}{Pr}\frac{d\Theta^+}{dy^+}\frac{d\Theta^+}{dy^+}-\frac{1}{Pr}\left\langle\frac{\partial\theta^+}{\partial x_j^+}\frac{\partial\theta^+}{\partial x_j^+}\right\rangle\right]+\Theta^+\frac{1}{\delta^+}=0,\end{aligned} \quad (4.72)$$

where $T_\theta^+=-\left\langle v^+\theta^+\right\rangle$. These four terms are respectively referred to as molecular transport (MT), gradient production/turbulent diffusion (GPTD), dissipation (D) and product heat generation (PG).

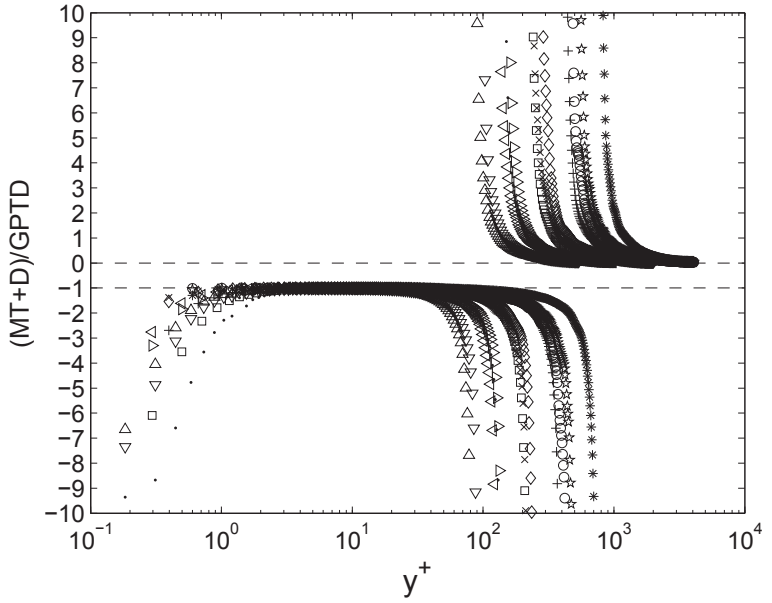

FIGURE 4.17: Ratio of the sum of the molecular transport (MT) and dissipation (D) terms to the gradient production/turbulent diffusion term (GPTD). Symbols are the same as in Fig. (4.1).

4.6.2 Four-layer structure

Analogous to previous study of the total kinetic energy budget equations, here, the ratio of the sum of the molecular transport term and the dissipation term to the gradient production/turbulent diffusion term (MT+D/GPTD) is considered to explore the layer structure of the total scalar variance equation. Consistent with the criterion used in the previous analysis, the ending position of layer i is where the ratio becomes greater than -2. The external bound layer ii is determined where the ratio is less than -2, while that of layer iii is based on where the ratio decreases below 0.5. The ratio profiles are shown in Fig. (4.17). Layer i lies close to the wall, $y^+ \lesssim 1$. In this domain, the leading balance is between the molecular transport term and the dissipation term. Consistent with the layer I in previous mean scalar structure, the inner length scale, $\sqrt{\nu^2\alpha/u_\tau^3\delta}$, also scales

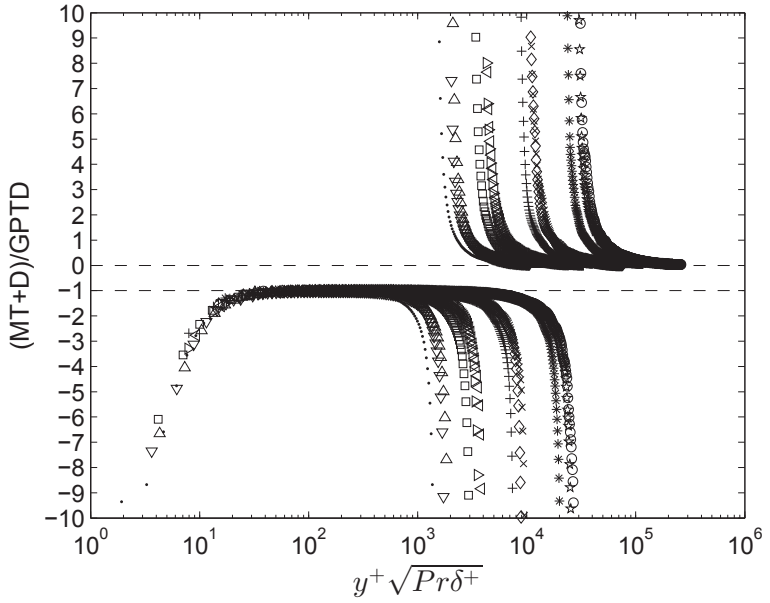

FIGURE 4.18: Ratio of the sum of the molecular transport (MT) and dissipation (D) terms to the gradient production/turbulent diffusion term (GPTD) versus $y^+\sqrt{Pr\delta^+}$. Symbols are the same as in Fig. (4.1).

the first layer (layer i). The length scale is reflected in Fig. (4.18). Curve fit gives $y^+_{i\,end}$ varies with $12.58Pe_\tau^{-\frac{1}{2}}$. Outside layer i, the ratio is approximately -1. Across this layer iii, the molecular transport, dissipation and the gradient production/turbulent diffusion terms constitute the leading balance. There is a balance breaking and exchange in layer iii, since the gradient production/turbulent diffusion term changes its sign within this layer. Except the molecular diffusion term, the other three terms are the leading order. With greater distance from the wall, the magnitude of the dissipation term become much smaller. The last layer is the region where the gradient production/turbulent diffusion term is balanced by the product heat generation term.

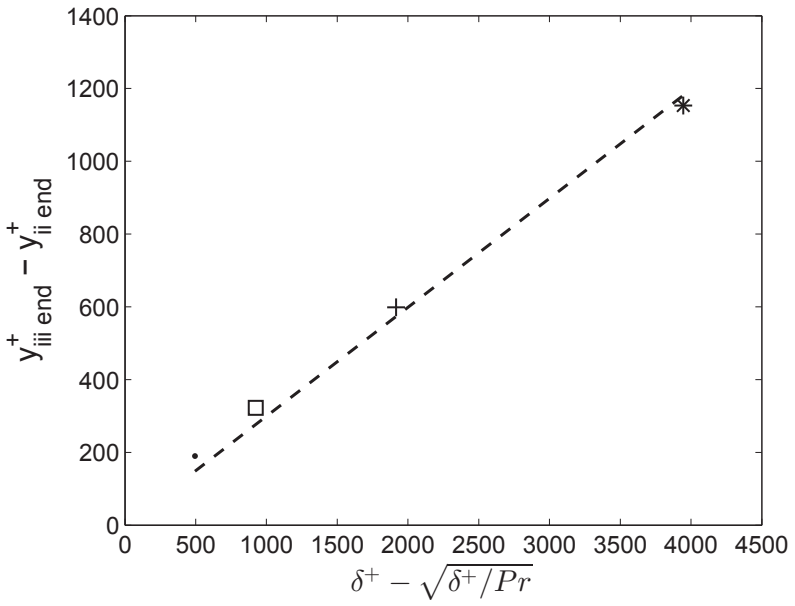

FIGURE 4.19: Inner-normalized width of layer iii for $Pr = 0.20$. $\cdot, \delta^+ = 548, Pr = 0.20, \delta^+/Pr = 2740$;$\square, \delta^+ = 995, Pr = 0.20, \delta^+/Pr = 4975$; $+, \delta^+ = 2017, Pr = 0.20, \delta^+/Pr = 10085$; $\ast$, $\delta^+ = 4088, Pr = 0.20, \delta^+/Pr = 20440$. Curve fit is given by $0.29(\delta^+ - \sqrt{\delta^+/Pr})$.

4.6.3 Width of layer iii

The Reynolds and Prandtl number dependence of the inner-normalized width of layer iii are shown in Fig. 4.19, Fig. 4.20 and Fig. 4.21 for $Pr = 0.20$, 0.71 and 1 respectively. Per the following scaling analysis (see Section 4.6.5), here, the inner-normalized width of layer iii is plotted for fixed Pr and is versus $\delta^+ - \sqrt{\delta^+/Pr}$. This is reasoned to account for the finite Reynolds number effect on the outer normalization. For fixed Pr, the inner-normalized width of layer iii increases following the linear trend of $\delta^+ - \sqrt{\delta^+/Pr}$. But the leading scaling coefficients are different for different Pr.

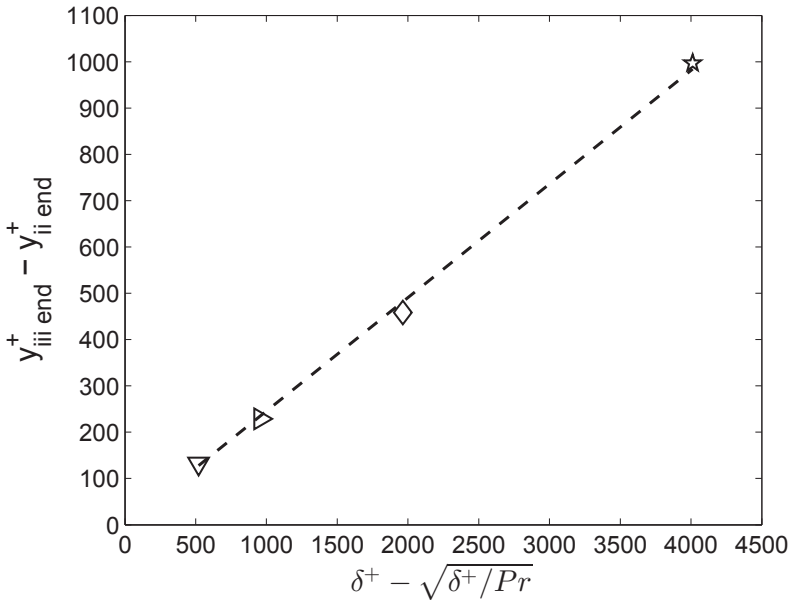

FIGURE 4.20: Inner-normalized width of layer iii for $Pr = 0.71$. $\bigtriangledown, \delta^+ = 548, Pr = 0.71, \delta^+/Pr = 772$; $\triangleright, \delta^+ = 995, Pr = 0.71, \delta^+/Pr = 1401$; $\diamond, \delta^+ = 2017, Pr = 0.71, \delta^+/Pr = 2841$; $\star$, $R\delta^+ = 4088, Pr = 0.71, \delta^+/Pr = 5758$. Curve fit is given by $0.25(\delta^+ - \sqrt{\delta^+/Pr})$.

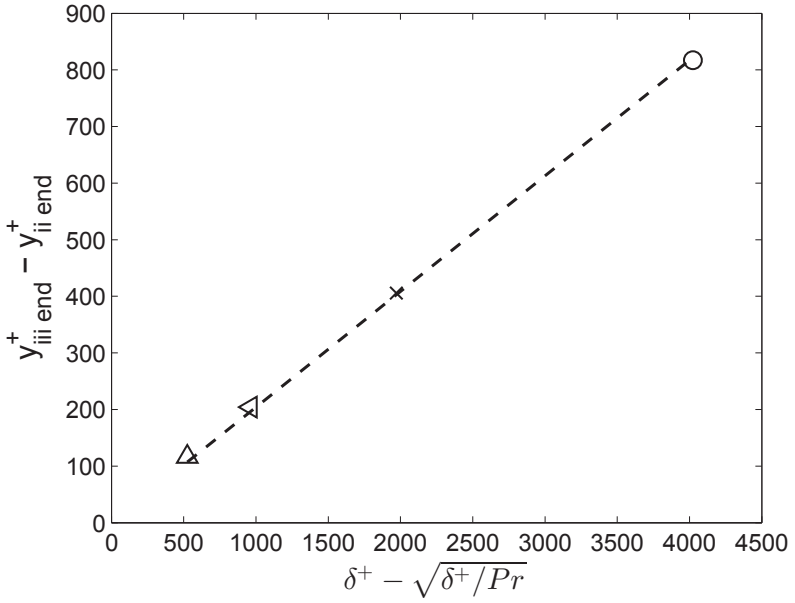

FIGURE 4.21: Inner-normalized width of layer iii for $Pr = 1$. $\triangle, \delta^+ = 548, Pr = 1, \delta^+/Pr = 548$; $\triangleleft, \delta^+ = 995, Pr = 1, \delta^+/Pr = 995$; $\times, \delta^+ = 2017, Pr = 1, \delta^+/Pr = 2017$; $\circ, \delta^+ = 4088, Pr = 1, \delta^+/Pr = 4088$. Curve fit is given by $0.21(\delta^+ - \sqrt{\delta^+/Pr})$.

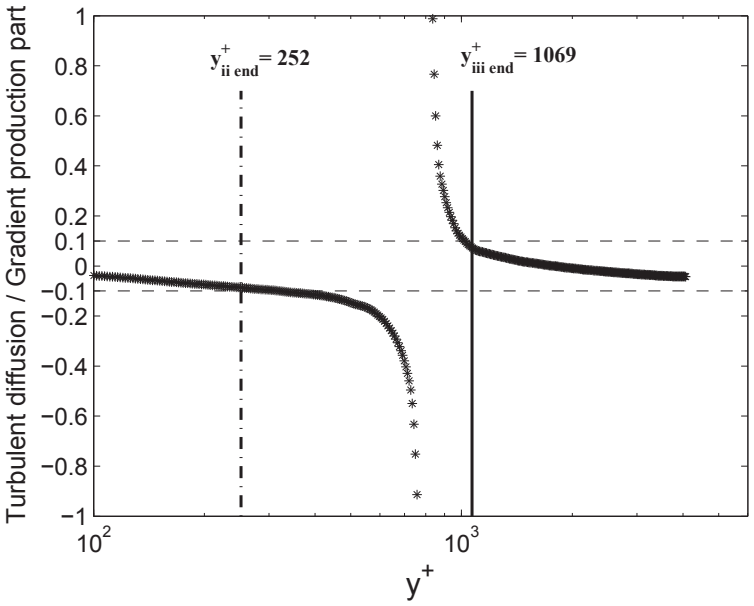

FIGURE 4.22: Ratio of the turbulent diffusion to the gradient production part at $Re_\tau = 4088, Pr = 0.20, Re_\tau/Pr = 20440$. The vertical dashed-dotted line denotes the external bound of layer ii. The vertical solid line denotes the external bound of layer iii.

4.6.4 Balance in layers iii and iv

Close examination indicates that across layers iii and iv, the contribution from turbulent diffusion is much smaller when compared to the contribution from the gradient generation part, $d[\Theta^+ T_\theta^+]/dy^+$. This characteristic is reflected in the results of Fig. 4.22. It is surmised that the turbulent diffusion term attains negligible value in layers iii and iv. The dissipation term is dominated by its turbulence contribution in layers iii and iv. This is demonstrated in Fig. 4.23, which show the ratios of the mean to turbulent dissipation. In these figures, the data curves consistently segregate into three groups depending on the Prandtl number. The vertical dashed-dotted, dashed and solid lines respectively represent the end of layer ii for $Re_\tau = 548, Pr = 1, Re_\tau/Pr = 548$, $Re_\tau = 548, Pr = 0.71, Re_\tau/Pr = 772$ and $Re_\tau = 548, Pr = 0.20, Re_\tau/Pr = 2740$.

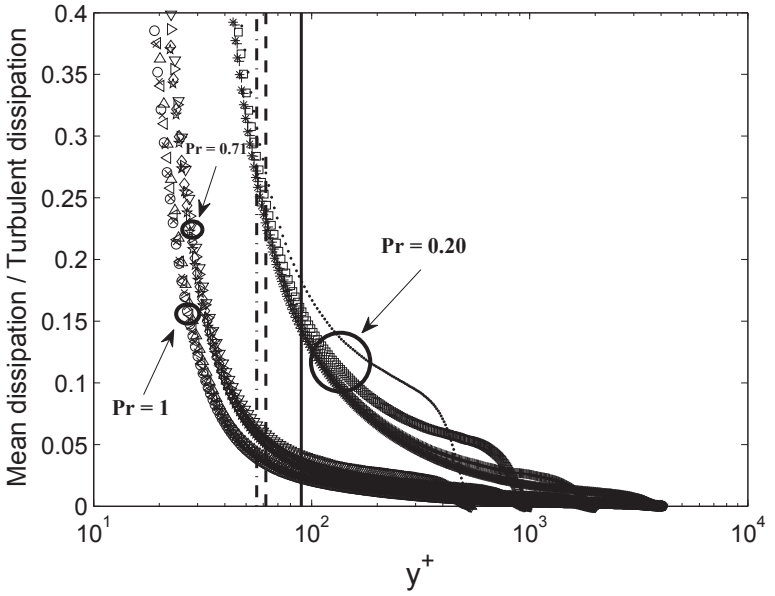

FIGURE 4.23: The ratio of the mean dissipation to the turbulent dissipation. The vertical dashed-dotted line denotes the external bound of layer ii at $Re_\tau = 548, Pr = 1, Re_\tau/Pr = 548$. The vertical dashed line denotes the external bound of layer ii at $Re_\tau = 548, Pr = 0.71, Re_\tau/Pr = 772$. The vertical solid line denotes the external bound of layer ii at $Re_\tau = 548, Pr = 0.20, Re_\tau/Pr = 2740$.

Beyond the start of layer iii the mean dissipation is at least 6 times smaller than the turbulent dissipation, and its effect over layer iii diminishes with increasing δ^+. So the layer iii balance therefore simplifies to be composed of $\Theta^+(dT_\theta^+/dy^+)$, $T_\theta^+(d\Theta^+/dy^+)$, turbulent dissipation and Θ^+/δ^+. Fig. 4.24 shows profiles of these four terms across layers iii and iv. Beyond layer iii, $T_\theta^+(d\Theta^+/dy^+)$ and turbulent dissipation lose leading order, becoming negligible compared to $\Theta^+(dT_\theta^+/dy^+)$ and Θ^+/δ^+. Fig. 4.25 shows profile of the ratio of $\Theta^+(dT_\theta^+/dy^+)$ to Θ^+/δ^+ and the ratio of $T_\theta^+(d\Theta^+/dy^+)$ to turbulent dissipation. As might be expected, although both the $T_\theta^+(d\Theta^+/dy^+)$ and turbulent dissipation terms are much smaller than the other two terms (and thus are not leading order), their ratio is nearly 1. This ratio then approaches zero at the edge of layer iv. Beyond layer ii, the gradient production term, $T_\theta^+(d\Theta^+/dy^+)$, is balanced by the turbulent dissipation

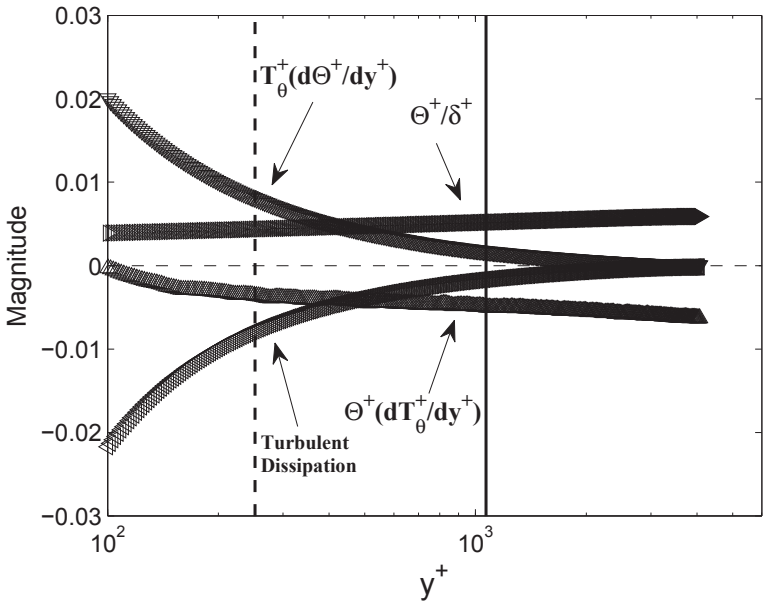

FIGURE 4.24: Profiles of $\Theta^+(dT_\theta^+/dy^+)$ ($\triangle$),$T_\theta^+(d\Theta^+/dy^+)$ ($\triangledown$), turbulent dissipation ($\triangleleft$) and Θ^+/δ^+ ($\triangleright$) across layers iii and iv at $Re_\tau = 4088, Pr = 1, Re_\tau/Pr = 4088$. The vertical dashed-dotted line denotes the external bound of layer ii. The vertical solid line denotes the external bound of layer iii.

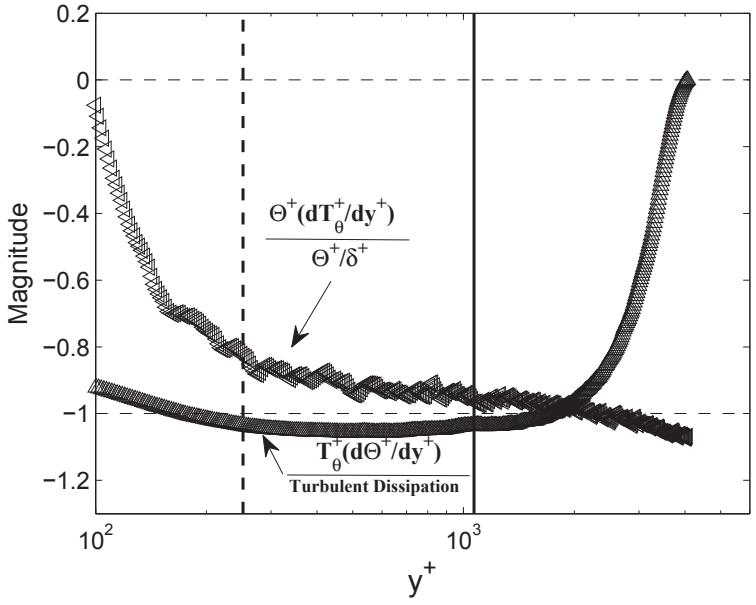

FIGURE 4.25: Ratios of $\Theta^+(dT_\theta^+/dy^+)$ to Θ^+/δ^+ ($\triangleleft$) and $T_\theta^+(d\Theta^+/dy^+)$ to turbulent dissipation ($\triangle$) at $Re_\tau = 4088, Pr = 1, Re_\tau/Pr = 4088$. The vertical dashed-dotted line denotes the external bound of layer ii. The vertical solid line denotes the external bound of layer iii.

term with the gradient production term approaching 0 rapidly as $y^+ \to \delta^+$. The ratio of $\Theta^+(dT_\theta^+/dy^+)$ to Θ^+/δ^+ is also approximately 1 throughout layer iv. It is concluded that beyond layer ii, the production gradient of turbulent transport flux term balances the product heat generation term. These two separate balance reflect the individual balances of the mean and turbulence scalar variance equations.

4.6.5 Theoretical prediction of the characteristic length scale of layer iii

This section provides a rigorous scaling verification supporting the use of the $(\delta^+ - \sqrt{\delta^+/Pr})$ in Section 4.6.3 as the characteristic length scale of the width of layer iii.

The layer iii is located in the non-diffusive domain associated with the similarity solution of the mean scalar transport equation. Over this domain, Eq. (4.51) gives

$$\frac{1}{Pr}\frac{d^2\Theta^+}{dy^{+2}} = -\frac{1}{Pr}\frac{\phi_{\theta c}^2}{\left(y^+ - C_1\right)^2}. \tag{4.73}$$

Relation in Eq. (4.8) yields

$$\begin{aligned}
\frac{dT_\theta^+}{dy^+} &= -\frac{1}{Pr}\frac{d^2\Theta^+}{dy^{+2}} - \epsilon^2 \\
&= \frac{1}{Pr}\frac{\phi_{\theta c}^2}{\left(y^+ - C_1\right)^2} - \epsilon^2 \\
&= \frac{1}{Pr}\frac{\phi_{\theta c}^2}{\left(y^+ - C_1\right)^2} - \frac{1}{Pr}\frac{\phi_{\theta c}^2}{\left(y_{\theta m}^+ - C_1\right)^2},
\end{aligned} \tag{4.74}$$

where T_θ^+ is evaluated maximum at $y_{\theta m}^+$. Integration of Eq. (4.74) leads to

$$T_\theta^+ = C_4 - \frac{1}{Pr}\frac{\phi_{\theta c}^2}{y^+ - C_1} - \frac{1}{Pr}\frac{\phi_{\theta c}^2 y^+}{\left(y_{\theta m}^+ - C_1\right)^2}. \tag{4.75}$$

Neglecting C_1 as $\delta^+ \to \infty$ and using $y_{\theta m}^+ = H\sqrt{\delta^+/Pr}$ (see Section 4.4.2, where $H \simeq 1.48$) gives

$$\frac{dT_\theta^+}{dy^+} = \frac{1}{Pr}\frac{\phi_{\theta c}^2}{y^{+2}} - \frac{\phi_{\theta c}^2}{H^2\delta^+} \tag{4.76}$$

and

$$T_\theta^+ = C_4 - \frac{1}{Pr}\frac{\phi_{\theta c}^2}{y^+} - \frac{\phi_{\theta c}^2 y^+}{H^2\delta^+}. \tag{4.77}$$

Evaluating $T_\theta^+ = 0$ at $y^+ = \delta^+$ as $\delta^+ \to \infty$ with fixed Pr yields

$$C_4 = \frac{\phi_{\theta c}^2}{H^2}. \tag{4.78}$$

Evaluating $T_\theta^+ = 1$ at $y^+ = y_{\theta m}^+ = H\sqrt{\delta^+/Pr}$ as $\delta^+ \to \infty$ with fixed Pr yields

$$1 = \frac{\phi_{\theta c}^2}{H^2}, \tag{4.79}$$

and thus $C_4 \to 1$ as $\delta^+ \to \infty$.

The balance requirement that $\Theta^+(dT_\theta^+/dy^+) \sim \epsilon^2\Theta^+$ in layer iii gives

$$\frac{dT_\theta^+}{dy^+} = \frac{1}{Pr}\frac{\phi_{\theta c}^2}{y^{+2}} - \frac{\phi_{\theta c}^2}{H^2\delta^+} = O\left(\epsilon^2\right). \tag{4.80}$$

As $\delta^+ \to \infty$, $\phi_{\theta c}^2 = O(1)$ and $\phi_{\theta c}^2/H^2 = O(1)$, Eq. (4.80) is only valid when $y^+ \geqslant O(1/\sqrt{Pr}\epsilon)$. Requiring $y^+ \geqslant O(1/\sqrt{Pr}\epsilon)$ in Eq. (4.77) and noting that C_4 is $O(1)$ gives

$$T_\theta^+ = O\left(1 - \frac{\epsilon}{\sqrt{Pr}}\right) \tag{4.81}$$

for fixed Pr in layer iii. This order of magnitude is corroborated by the layer iii that is beyond the peak of T_θ^+, since the $T_{\theta m}^+$ is $1 - O(\epsilon/\sqrt{Pr})$.

Within layer iii, Eq. (4.80) gives

$$\frac{dT_\theta^+}{dy^+} = O\left(\epsilon^2\right). \tag{4.82}$$

Rescaling begins by setting

$$T_\theta^+ = R\bar{T}_\theta, \quad y^+ = y_0^+ + S\bar{y}, \tag{4.83}$$

where $\bar{T}_\theta$, $\bar{y}$ are $O(1)$ as $\delta^+ \to \infty$. Analogously, y_0^+ is the position where the gradient production/turbulent diffusion term changes its sign in layer iii. Rescaling transformation gives

$$\frac{dT_\theta^+}{dy^+} = \frac{R}{S}\frac{d\bar{T}_\theta}{d\bar{y}}. \tag{4.84}$$

Thus

$$\frac{R}{S} = \epsilon^2, \tag{4.85}$$

or

$$S = \frac{1}{\epsilon^2} R. \tag{4.86}$$

R is the order of T_θ^+ in layer iii that is $1 - \epsilon/\sqrt{Pr}$, S is determined by

$$\begin{aligned} S &= \frac{1}{\epsilon^2}\left(1 - \frac{\epsilon}{\sqrt{Pr}}\right) \\ &= \frac{1}{\epsilon^2} - \frac{1}{\epsilon\sqrt{Pr}}, \end{aligned} \tag{4.87}$$

or

$$\begin{aligned} y^+ &= y_0^+ + \left(\frac{1}{\epsilon^2} - \frac{1}{\epsilon\sqrt{Pr}}\right)\bar{y} \\ &= y_0^+ + \left(\delta^+ - \sqrt{\frac{\delta^+}{Pr}}\right)\bar{y}. \end{aligned} \tag{4.88}$$

By definition, $\bar{y}$ is $O(1)$ in layer iii, and thus it follows that the inner-normalized width of layer iii is $O(\delta^+ - \sqrt{\delta^+/Pr})$ with fixed Pr. This scaling is interpreted as a finite Reynolds number correction to traditional outer scaling, since it is apparent that $(\delta^+ - \sqrt{\delta^+/Pr}) \to \delta^+$ for fixed Pr as $\delta^+ \to \infty$.

4.7 Comparison between streamwise velocity fluctuation and scalar fluctuation

Analysis in Section 4.5.4 indicates the scalar Kármán constant for $Pr = 1$ is $k_\theta > 0.45$. This is greater than the Kármán constant, i.e., $k \simeq 0.39$. The fact that the mean momentum equation, Eq. (1.1), and mean scalar equation, Eq. (4.8), take on the same form with the same boundary conditions if $Pr = 1$ might lead one to naively expect the scalar Kármán constant should be numerically the same as the Kármán constant. Namely, an identical equation with the same boundary conditions is expected to yield the same result. Here, however, there is the inherent issue associated with the indeterminacy of these equations.

The present theory indicates that the values of k and k_θ are directly related to the gradient of width distribution functions, W^+ and W_θ^+, of the scaling layer hierarchy in the inertial domain and non-diffusive domain, respectively. The definitions of the W^+ and W_θ^+ are

$$W^+ = \left(\frac{dT^+}{dy^+} + \frac{1}{\delta^+} \right)^{-\frac{1}{2}}, \tag{4.89}$$

and

$$W_\theta^+ = \left(\frac{dT_\theta^+}{dy^+} + \frac{1}{\delta^+} \right)^{-\frac{1}{2}}. \tag{4.90}$$

The only difference comes from the dT^+/dy^+ and dT_θ^+/dy^+. The Reynolds stress, $T^+ = -\langle uv \rangle^+$, is the inner-normalized covariance of the streamwise velocity fluctuation u and

the wall-normal velocity fluctuation v. The turbulent flux, $T_\theta^+ = -\langle v\theta \rangle^+$, is the inner-normalized covariance of the scalar fluctuation θ and the wall-normal velocity fluctuation v. Since the v fluctuations are unchanged, the different transport of the u and the θ and their correlation with the v account for the difference between the gradient of Reynolds stress and the gradient of turbulent flux in the inertial (non-diffusive) domains of interest. This section explores the differences in greater details.

4.7.1 Streamwise velocity budget balance and scalar budget balance

The difference in the streamwise velocity u and scalar θ can be elaborated via their respective budget equations. The inner-normalized streamwise velocity budget equation for fully-developed turbulent channel flow is

$$-\frac{d}{dy^+}\left\langle u^+u^+v^+\right\rangle + \frac{d^2}{dy^{+2}}\left\langle u^+u^+\right\rangle + 2T^+\frac{dU^+}{dy^+} - 2\left\langle \frac{\partial u^+}{\partial x_j^+}\frac{\partial u^+}{\partial x_j^+}\right\rangle + 2\left\langle p^+\frac{\partial u^+}{\partial x^+}\right\rangle = 0. \quad (4.91)$$

As expected, this equation has five terms of a form similar to those found in the turbulence kinetic energy equation. The five terms are referred to as turbulent diffusion, viscous diffusion, production, dissipation and pressure-strain.

The inner-normalized scalar budget equation with uniform heat generation is

$$-\frac{d}{dy^+}\left\langle v^+\theta^+\theta^+\right\rangle + \frac{1}{Pr}\frac{d^2}{dy^{+2}}\left\langle \theta^+\theta^+\right\rangle + 2T_\theta^+\frac{d\Theta^+}{dy^+} - 2\frac{1}{Pr}\left\langle \frac{\partial\theta^+}{\partial x_j^+}\frac{\partial\theta^+}{\partial x_j^+}\right\rangle = 0. \quad (4.92)$$

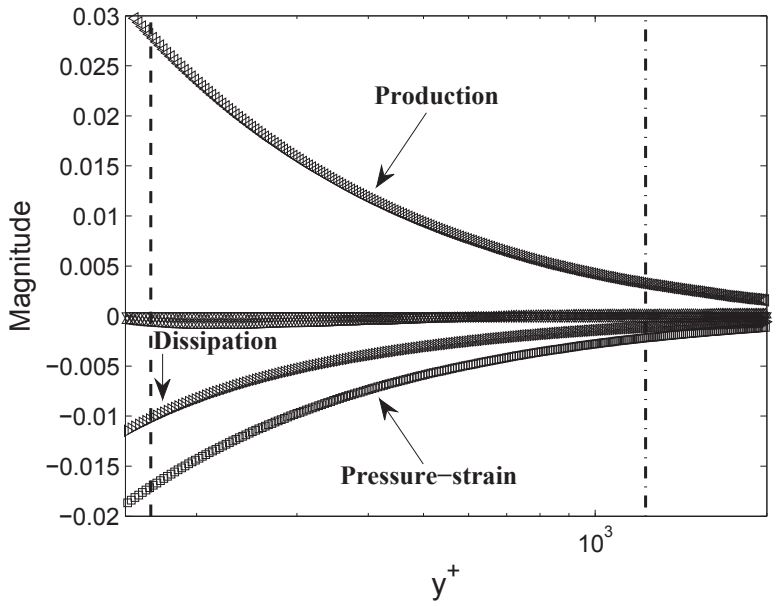

FIGURE 4.26: Profiles of terms in Eq. (4.91) across inertial domain at $\delta^+ = 4088$. $\triangle$, turbulent diffusion; $\triangledown$, viscous diffusion; $\triangleleft$, production; $\triangleright$, dissipation; $\square$, pressure-strain. The vertical dashed line denotes the external bound of layer III for mean momentum balance. The vertical dashed-dotted line denotes $y^+ = 0.3\delta^+$.

The four terms are referred to as turbulent diffusion, molecular transport, gradient production and dissipation.

There are five terms in u budget equation, while there are only four terms in θ budget equation. As is apparent, the pressure-strain terms play non-trivial role in streamwise velocity transport. Since the similarity solution for both the mean velocity and mean scalar are valid over the inertial (non-diffusive) domain, the leading balance for the budget equations, i.e., Eq. (4.91) and Eq. (4.92) are considered in this region. Specifically, $2.6\sqrt{\delta^+} \lesssim y^+ \lesssim 0.3\delta^+$ is used for the u budget equation, and $2.5\sqrt{\delta^+/Pr} \lesssim y^+ \lesssim 0.3\delta^+$ with $Pr = 1$, is used for the v budget equation. Fig. 4.26 and Fig. 4.27 respectively show representative profiles of the terms in Eq. (4.91) and Eq. (4.92) across the noted domains. Similar production and generation production profiles are observed across this domain.

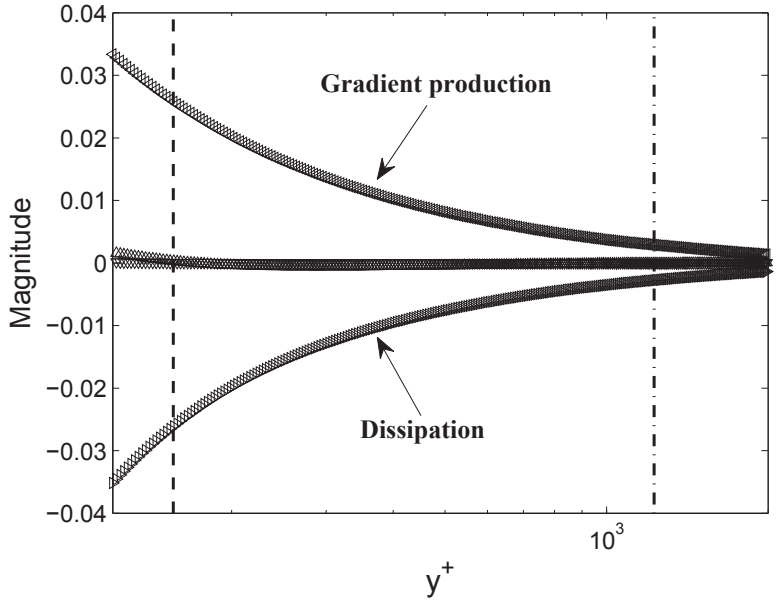

FIGURE 4.27: Profiles of terms in Eq. (4.92) across non-diffusive domain at $\delta^+ = 4088$ and $Pr = 1$. $\triangle$, turbulent diffusion; $\triangledown$, molecular transport; $\triangleleft$, gradient production; $\triangleright$, dissipation. The vertical dashed line denotes the external bound of layer III for mean scalar balance. The vertical dashed-dotted line denotes $y^+ = 0.3\delta^+$.

The $\langle uu \rangle^+$ budget in the logarithmic region of the mean velocity profile is characterized by the leading balance of three terms, production, dissipation and pressure-strain. However, only the dissipation term balances to the gradient production terms in the logarithmic region of the mean scalar profile. The magnitude of the streamwise velocity dissipation is less than that of the scalar dissipation. This difference is physically compensated by the pressure-strain. The negative work done by the fluctuating pressure of turbulence and the lower streamwise velocity dissipation rate are regarded to be responsible for the higher mean velocity gradient compared to the mean scalar gradient, i.e., $k < k_\theta$. This is consistent with Pirozzoli et al. (2016), where the instantaneous cross-stream visualizations of u' and θ' show the interfaces between neighbouring eddies are sharper in the θ' field than the u' field. This observation is related to the lower dissipation and the work

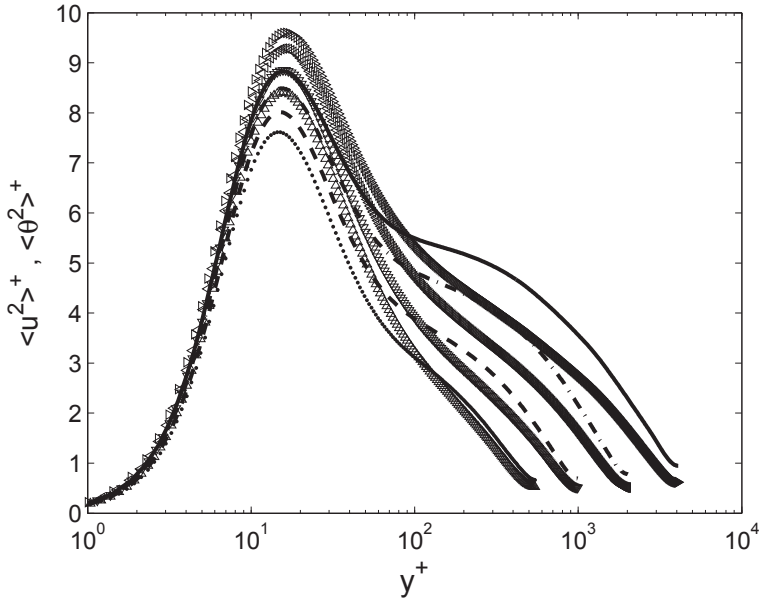

FIGURE 4.28: Streamwise velocity and scalar variances. Dotted line, $\langle u^2 \rangle^+, \delta^+ = 548$; Dashed line, $\langle u^2 \rangle^+, \delta^+ = 995$; Dashed-dotted line, $\langle u^2 \rangle^+, \delta^+ = 2017$; Solid line, $\langle u^2 \rangle^+, \delta^+ = 4088$; $\triangle$, $\langle \theta^2 \rangle^+, \delta^+ = 548, Pr = 1$; $\bigtriangledown$, $\langle \theta^2 \rangle^+, \delta^+ = 995, Pr = 1$; $\triangleleft$, $\langle \theta^2 \rangle^+, \delta^+ = 2017, Pr = 1$; $\triangleright$, $\langle \theta^2 \rangle^+, \delta^+ = 4088, Pr = 1$.

done by the pressure in the inertial (non-diffusive) domain.

4.7.2 Correlation

Streamwise velocity variance and scalar variance for $Pr = 1$ are shown in Fig. 4.28. The stream velocity variances attain a higher values and tend to form a mid peak just prior to its logarithmic decay. However, the Reynolds stress, T^+, and turbulent flux, T_θ^+, are nearly indistinguishable from each other, which is shown in Fig. 4.29. A tiny difference between T^+ and T_θ^+ is observed in the inertial (non-diffusive) domain, where the T_θ^+ is higher.

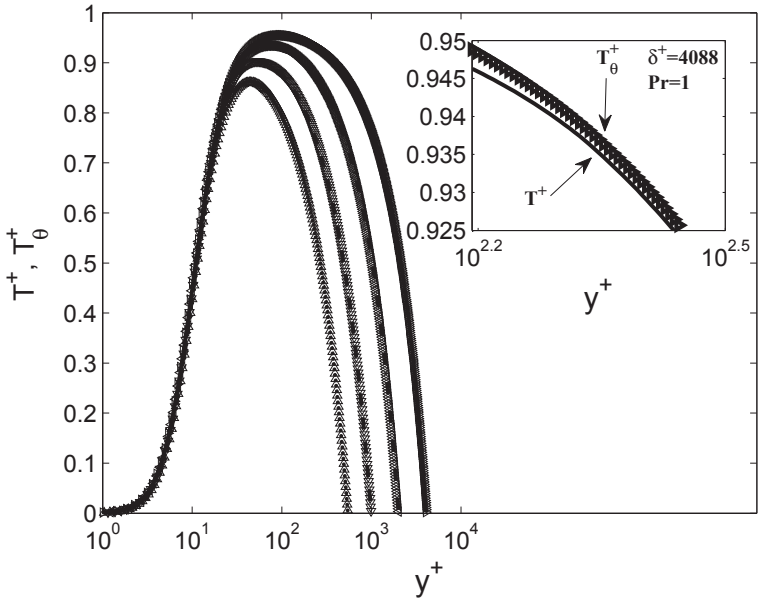

FIGURE 4.29: Reynolds stress and turbulent flux. Symbols are the same as in Fig. 4.28. Inset: Solid line, $T^+, \delta^+ = 4088$; $\triangleright, T_\theta^+, \delta^+ = 4088, Pr = 1$.

The connection of the u and θ to the v is investigated through the profile of the statistical correlation coefficient that is defined as

$$C_{ab} = \frac{\langle ab \rangle}{\sqrt{\langle a^2 \rangle}\sqrt{\langle b^2 \rangle}}. \tag{4.93}$$

It is the ratio of the covariance of two time series to the product of the standard deviation of these two time series. The profiles of the $-C_{uv}$ and $-C_{v\theta}$ is shown in Fig. 4.30. Specifically, $-C_{uv}$ and $-C_{v\theta}$ for $\delta^+ = 4088$ is shown in Fig. 4.31. In the logarithmic region, both $-C_{uv}$ and $-C_{v\theta}$ stay close to 0.4, and increases with distance from the wall, with a reduction in the magnitude as δ^+ increases. However, the increment of $-C_{v\theta}$ in the inertial (non-diffusive) domain is greater than that of the $-C_{uv}$, where θ becomes more linearly correlated with the v than the u. This property also leads to the higher

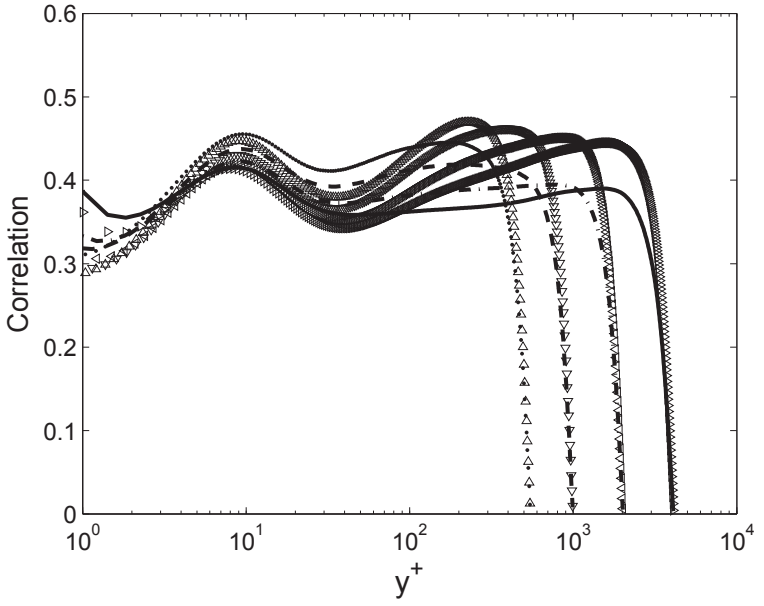

FIGURE 4.30: Profiles of correlation coefficient. Dotted line, $-C_{uv}, \delta^+ = 548$; Dashed line, $-C_{uv}, \delta^+ = 995$; Dashed-dotted line, $-C_{uv}, \delta^+ = 2017$; Solid line, $-C_{uv}, \delta^+ = 4088$; $\triangle$, $-C_{v\theta}, \delta^+ = 548, Pr = 1$; $\bigtriangledown$, $-C_{v\theta}, \delta^+ = 995, Pr = 1$; $\triangleleft$, $-C_{v\theta}, \delta^+ = 2017, Pr = 1$; $\triangleright$, $-C_{v\theta}, \delta^+ = 4088, Pr = 1$.

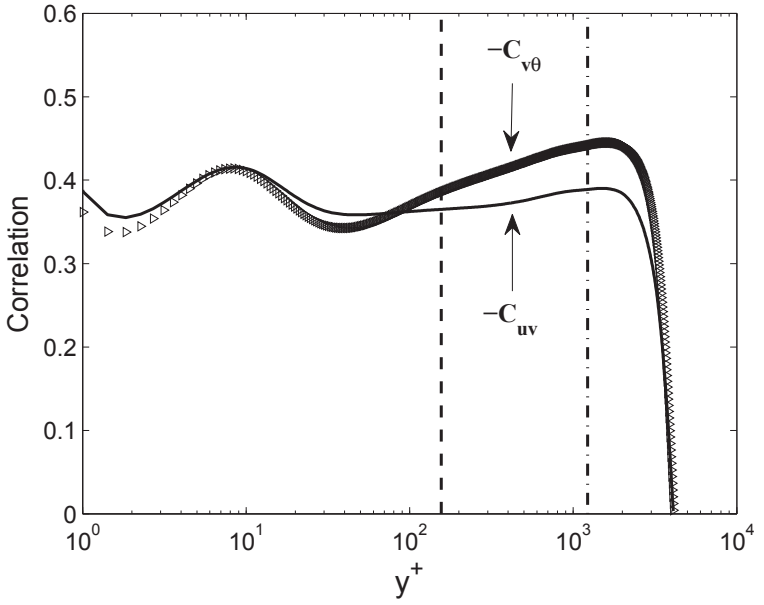

FIGURE 4.31: Profiles of correlation coefficient. Solid line, $-C_{uv}, \delta^+ = 4088$; $\triangleright$, $-C_{v\theta}, \delta^+ = 4088, Pr = 1$; The vertical dashed line denotes the external bound of layer III for mean scalar balance. The vertical dashed-dotted line denotes $y^+ = 0.3\delta^+$.

slope of the logarithmic mean velocity than the mean scalar. For incompressible flow, based on the continuity equation and Poisson equation, the streamwise velocity, u, and the wall-normal velocity, v, are related to each other. The incompressibility constrains the development of u by that of the v and the pressure-strain. However, the correlation coefficient indicates the unconstrained θ is more linearly correlated with the v than u. This phenomenon leads to the expectation that the restrictions between the u and v make them correlated more non-linearly in the flow.

4.8 Summary

A multi-scale analysis of the mean equation for heat transport in fully developed turbulent channel flow subjected to volumetrically uniform heat generation was presented herein. These analyses were both aided by, and validated with, the recent DNS of Pirozzoli et al. (2016) which cover unprecedented ranges in Reynolds and Prandtl numbers via DNS. As noted at a number of points in the analysis, the present flow configuration is especially attractive for the purposes of elucidating the underlying self-similar structure admitted by the the mean equation. This physically stems from the fact that the uniform heat generation is identically balanced by an outward flux of heat across the bounding surfaces. Mathematically, this leads to an analytical structure that is very similar to that for the mean momentum field.

The mean equation for scalar transport is unclosed. Thus, analytical approaches seeking to employ this equation must either invoke hypotheses or assumptions of a mathematical or phenomenological nature (or both), or at some point invoke empirical observations. For example, the distance-from-the-wall scaling (y-scaling) hypothesis is regularly invoked without proof, even though it is a central tenet of many models, e.g., Townsend's attached eddy scaling paradigm. Similarly, the notions of an inner/outer/overlap layer structure are regularly assumed to exist. So much so, that *overlap layer* is often used as a synonym for the *logarithmic layer*. Owing, however, to the unclosed governing equation, both this structure and the form of the expansions employed in the associated mathematical analyses must be assumed. In fact, this approach proceeds with essentially no reliance on the governing equations.

The present approach formally invokes an empirical step at its inception. (Albeit, given what has been learnt regarding wall-flow structure over the past decade, the results of this empirical step are now well-established.) Namely, when data are used to elucidate the leading balance structure of the terms in the mean heat equation, the layer structure indicated in Fig. 4.1 is observed. With only the information that these leading balance layers exist (but not their extent or their scaling properties), the present approach then determines all its subsequent results directly from the properties admitted by the governing mean equation and its boundary conditions. These results include: the scaling properties associated with the extent of layers II and III (and thus layer IV as well), the scaling for the location of the peak in T_θ^+ and the asymptotic rate that T_θ^+ approaches unity, an invariant scaling for T_θ that is extends from a position interior to its peak to

the centerline, the formal admittance of an asymptotically self-similar scaling layer hierarchy, and the exploitation of this self-similar structure to develop the logarithmic mean temperature profile equation via direct integration of the mean equation. Here it is also noted that the hierarchy layer widths are shown to asymptotically scale with y (Fife et al., 2009), and thus this result provides a basis for *distance from the wall* scaling. All of the noted results are strongly supported by the DNS data comparisons herein.

Conversely, other results from the present analyses are less clear. Based upon previous analyses of the momentum equation, the expectation is that the respective temperature increments across layers I and IV should scale with θ_τ and Θ_c as $\delta^+ \to \infty$, while the increments across layers II and III should scale with Θ_c and θ_τ, respectively (Wei et al., 2005a). The data of Fig. 4.6, Fig. 4.7 and Fig. 4.8 are, however, not conclusive in this regard. Namely, it is apparent that Pr has a significant effect on the mean temperature increments, and furthermore the DNS are not at high enough δ^+ to convincingly provide evidence of an asymptotic limit.

Similarly, while the results of Fig. 4.2 provide rather compelling empirical support for invariant profiles at the boundary between layers I and II, a purely analytical reason for this is apparently beyond our current capabilities. Note that for this boundary region one cannot simply neglect the GT term in Eq. 4.8 and rescale the remaining terms into a parameter free invariant form. This is because as the wall is approached from above there is a region, akin to the boundary region between layers II and III, where all three terms in Eq. (4.8) come into balance. Similar to the rescaling as $y^+ \to y^+_{\theta m}$, the GT term approaches zero as $y^+ \to 0$. Additionally, however, so do T^+_θ and $d^2T^+_\theta/dy^{+2}$, and therefore

there exists a different set of constraints. As described by Wei et al. (2007), determining the appropriate scaling in the region approaching this *truncated* scaling region (truncated by the wall) depends upon the nonlinear variations in T_θ^+ and Θ^+ in the region just outside the conduction sublayer. How to analytically proceed here, however, is not readily apparent, since other guiding attributes, like those associated with the scaling hierarchy, are not available. Analysis is performed as far as possible, and then use the empirical result of Fig. 4.2 to investigate their ramifications as well as check for self-consistency. This is done in Appendix B.

Lastly, the present theory provides ways of estimating the value for k_θ that extend beyond directly fitting to the profile slope. In accord with previous empirical observations, the dW_θ^+/dy^+ based results herein reveal that k_θ is distinctly larger than its mean velocity counterpart. Insights regarding this are gained by noting that for $Pr = 1$ Eq. (4.8) and its boundary conditions are identical to those for the channel flow mean momentum equation. This suggests that the different value for k_θ arises from properties that lead to (slight) differences between the Reynolds stress and turbulent heat flux. Specifically, because the wall normal fluctuations are unchanged, the culprit is identified as being associated the differences between the u and θ fluctuations. The pressure-strain term that influences the transport of $\langle u^2 \rangle$ is at least partly the cause, as no such effect is present in the transport equation for scalar variance. Also, the magnitude of the correlation coefficient between θ and v grows more greatly than that between the u and v. The less linear correlation between u and v seems also leads to the $k > k_\theta$ in the inertial (non-diffusive) domain.

Relative to this, different Pr results in the data profiles clearly segregating into individual groups in layer iii of the total scalar variance balance. And the inner-normalized layer width of layer iii in each group strictly follows a linear trend with increasing $\delta^+/Pr - \sqrt{\delta^+/Pr}$. The layer scaling behaviors associated with the total scalar variance differ obviously differ from those of the mean scalar balance. The layer iii of total scalar variance exhibits a complex balance exchange. Although both the magnitude of the gradient production and turbulent dissipation terms in the turbulence scalar variance equation tends to approach zero, they balance each other throughout the layers iii and iv, while the production gradient of turbulent transport flux and product heat generation terms from mean scalar equation constitute the leading balance over layers iii and layer iv.

CHAPTER 5

CONCLUSIONS

Significant work has been carried out over the past decade on wall-bounded turbulent flows. Wei et al. (2005a) explored the mean momentum balance in turbulent channel, pipe and boundary layer flows experimentally and theoretically. Empirical observation and multi-scale analysis revealed a dynamically relevant four-layer structure that is different from the traditional mean-profile-based four-layer description of the structure in wall turbulence. Each of the four layers is characterized by a leading balance of two or three terms in the mean momentum equation. Layers I and Iv respectively comply with the inner and outer length scale, but layers II and III exhibit an intermediate length scale, i.e., $\sqrt{\nu\delta/u_\tau}$, which plays as a good transition from inner to the outer scales. A scaling layer hierarchy was quantitatively characterized for the mean momentum balance. And the mean momentum equation admits its self-similarity over the domain where the derivative of the scaling layer width distributions function is a constant.

In this dissertation research, three measures that quantify the properties of inertial domain are explored based on the experimentally acquired turbulent boundary layer data

measured at Flow Physics Facility in University of New Hampshire to be in comparison where these measures provide evidence of self-similarity with where the mean momentum equation exhibits its self-similar behavior. Research findings indicate that the region where the KLD and higher order even moments exhibit the evidence of emerging self-similar behavior are indistinguishable from each other. The region is between $2.6\sqrt{\delta^+}$ and $0.3\delta^+$. It lies interior to the estimated bound of the inertial domain associated with the self-similarity admitted by the mean momentum equation. The self-similarity region of the diagnostic plot is indistinguishable from the inertial domain. It is from $2.6\sqrt{\delta^+}$ to $0.5\delta^+$. similar approach in previous study of the mean momentum equation is used to explore the kinetic energy budgets in wall turbulence. Kinetic energy equations are simplified based on reasonable assumptions and approximations. Available simulation data are used to explore the total kinetic energy equation. It reveals that there exists an four-layer structure with the properties that in each of the layer, the leading balance occurs between some of the four grouped terms in the total kinetic energy equation. The layer iii exhibits a complex balance exchange and the inner-normalized width of layer iii has a dependence on $\delta^+ - \sqrt{\delta^+}$. Rigorous analytical scaling analysis is provided to describe the length scale of layer iii. The last part of this dissertation continues the empirical and multi-scale analysis onto the scalar transport in turbulent channel flow with zero temperature on both upper and lower walls but a uniform heat generation over the whole domain. Two different four-layer structures are respectively found for the mean scalar and total scalar variance transport equations based on the simulation data. As for the mean scalar transport, the external bounds of layers II and III have a dependence on

$\sqrt{\delta^+/Pr}$. There is also a scaling layer hierarchy across a interior region, where the mean scalar equation exhibits an invariant form. Properties of a similarity solution to the mean scalar equation for fully developed turbulent channel flow are quantified. The similarity solution is found by analytically integrating an invariant form of the mean scalar equation on a non-diffusion sub-domain. The resulting mean temperature profile function adheres to the classical logarithmic profile function. At finite Reynolds number, however, the solution has an additive linear term, and an offset in the argument to the logarithm. As for the total variance transport, the data strictly segregate into three groups across layer iii based on three different values of Pr. In each group, the inner-normalized width of layer iii independently has a dependence on $\delta^+/Pr - \sqrt{\delta^+/Pr}$. Across layers iii and iv, two individual balance occurs between the production gradient of turbulent transport flux and product heat generation terms from the mean scalar variance equation, and between the gradient production and turbulent dissipation terms from the turbulence scalar variance equation.

APPENDIX A

TURBULENT PRESSURE NORMALIZATION

As described in Section 3.2.2, in the present analysis turbulent pressure is effectively normalized by $\rho u_\tau \nu/\delta$, rather than by ρu_τ^2. If ρu_τ^2 is used for turbulent pressure normalization, the turbulent pressure diffusion term is simply given by $-\partial \left\langle p^+ v^+ \right\rangle / \partial y^+$, and the normalized magnitude of this term increases by a factor of δ^+. This appendix quantifies, however, that the leading order balances do not change owing to the present choice for fluctuating pressure normalization.

Figs. A.1 (a) and (b) show the ratio of $-\partial \left\langle p^+ v^+ \right\rangle / \partial y^+$ to D^+. In layer i, all its values fall between 0 and -0.02, and thus the dominant balance determined for layer i herein is retained. In layer ii,$-\partial \left\langle p^+ v^+ \right\rangle / \partial y^+$ is always observed to be less than 1/10 of the sum of the VD and D terms, and generally much less. This behavior is shown in Figs. A.1 (c) and (d) for two representative Reynolds numbers. There is no apparent Reynolds number trend associated with this ratio. Across layers iii and iv the total pressure diffusion contribution in channel flows (or the advection/turbulent pressure diffusion in boundary layers) is still much larger than the turbulent pressure diffusion contribution. The profiles

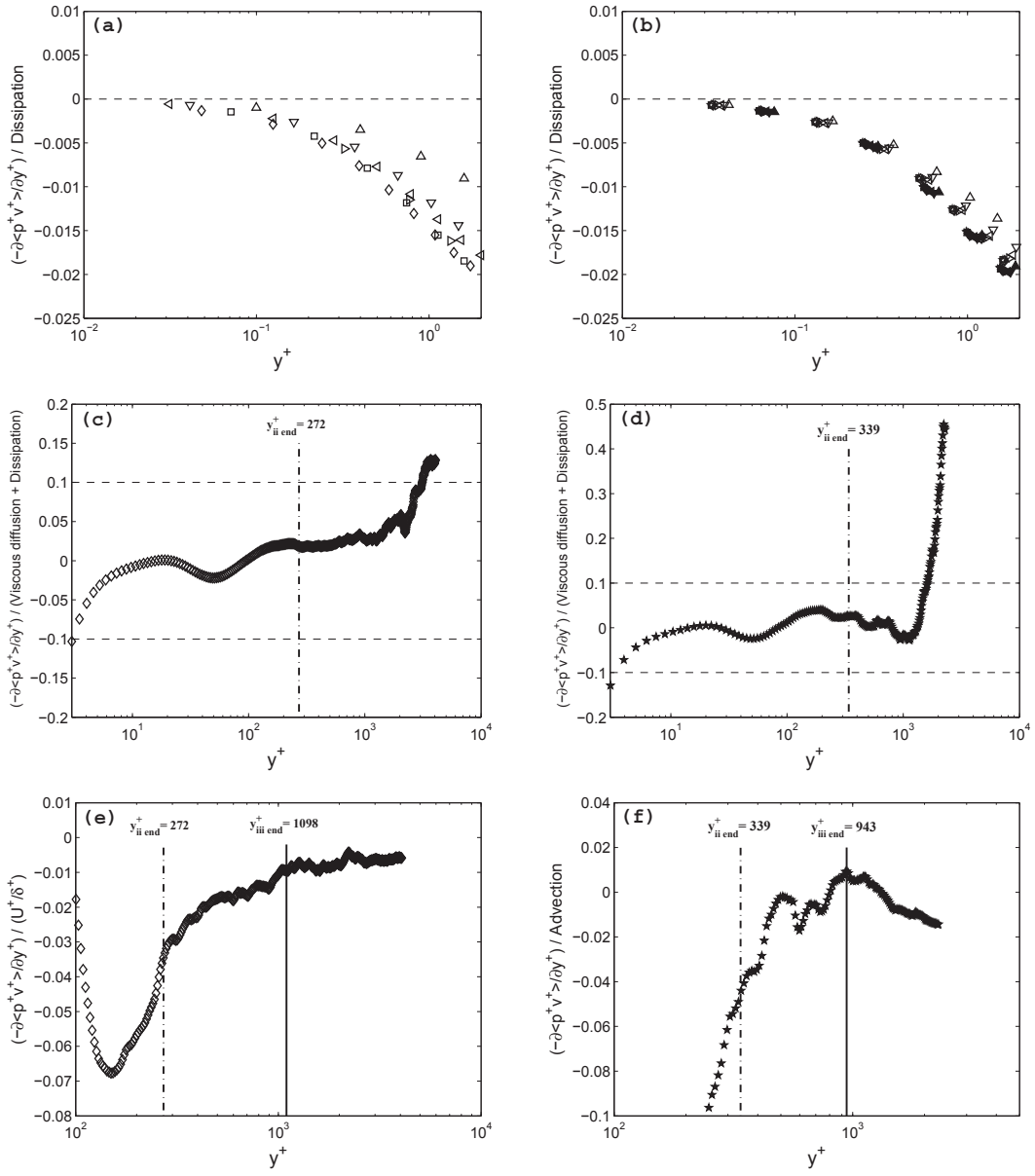

FIGURE A.1: Ratio of $-\partial \langle p^+v^+ \rangle / \partial y^+$ to D term in layer i for (a) channels; (b)boundary layers. Ratio of $-\partial \langle p^+v^+ \rangle / \partial y^+$ to the sum of the VD and D terms for (c) channel at $\delta^+ = 4079$; (d) boundary layer at $\delta^+ = 2299$. (e) Ratio of $-\partial \langle p^+v^+ \rangle / \partial y^+$ to the mean pressure diffusion term for channel at $\delta^+ = 4079$; (f) Ratio of $-\partial \langle p^+v^+ \rangle / \partial y^+$ to the advection term for boundary layer at $\delta^+ = 2299$.

of Figs. A.1 (e) and (f) at a fixed Reynolds number reflect representative behavior in this regard.

APPENDIX B

RESCALING INTO LAYER I OF MEAN SCALAR BALANCE

As the wall is approached from layer II, somewhere in layer I all three terms in Eq. (4.8) attain the same *actual* order of magnitude. Eq. (4.8), however, *formally* indicates that the HG term is sub-dominant. Thus, we now seek a rescaling of Eq. (4.8) such that each of the terms is formally $O(1)$. Here it is useful to note that at $y^+ = 0$, $\Theta^+ = 0$, $T_\theta^+ = 0$, $\frac{dT_\theta^+}{dy^+} = 0$ and $\frac{d\Theta^+}{dy^+} = Pr$. As with the analysis of layer III, conditions such as these set constraints on the nature of the transition into layer I. In contrast, however, the transition here is truncated by the wall, whereas in layer III the analogous location is the peak position of T_θ^+, and the exchange of balance across layer III completes into layer IV.

To accomplish the desired representation of Eq. (4.8), we seek a rescaling according to the finite transformations,

$$y^+ = \alpha \bar{y}, \quad T_\theta^+ = \beta \bar{T}, \quad \Theta^+ = Pry^+ + \gamma \bar{\Theta}. \tag{B.1}$$

Here we note that $\frac{dT_\theta^+}{dy^+} = 0$ at $y^+ = 0$, which is similar to $\frac{dT_\theta^+}{dy^+}$ passing through zero in layer III. Unlike the situation in layer III, T_θ^+ also equals zero at $y^+ = 0$, whereas T_θ

passes through its maximal value in layer III.

Inserting the above transformations into Eq. (4.8) gives

$$\frac{1}{Pr}\frac{d^2\Theta^+}{dy^{+2}} = \frac{1}{Pr}\frac{\gamma}{\alpha^2}\frac{d^2\bar{\Theta}}{d\bar{y}^2}, \quad \frac{dT_\theta^+}{dy^+} = \frac{\beta}{\alpha}\frac{d\bar{T}_\theta}{d\bar{y}}, \tag{B.2}$$

and the conditions that satisfy the requirement that the order of magnitude of each term match are

$$\frac{1}{Pr}\frac{\gamma}{\alpha^2} = \frac{1}{\delta^+} = \frac{\beta}{\alpha}. \tag{B.3}$$

At this point, we have insufficient information to uniquely determine the variable stretching parameters, α, β and γ, and thus the wholly analytical process ends.

If, however, the first balance is considered and

$$\frac{1}{Pr}\frac{\gamma}{\alpha^2} = \frac{1}{\delta^+}, \tag{B.4}$$

and invoke the empirical observation from Fig. 4.2 that the stretching is given by the factor $\sqrt{Pr\delta^+}$, then

$$\alpha = \frac{1}{\sqrt{Pr\delta^+}}, \tag{B.5}$$

and Eq. (B.4) becomes

$$\frac{1}{Pr}\gamma Pr\delta^+ = \frac{1}{\delta^+}, \tag{B.6}$$

or

$$\gamma = \frac{1}{\delta^{+2}}. \tag{B.7}$$

TABLE B.1: Semi-empirically surmised Θ scaling in layer I.

δ^+	Pr	$\Theta^+_{layer\,I}$	$\sqrt{\frac{Pr}{\delta^+}}$	$\Theta^+_{layer\,I}/\sqrt{\frac{Pr}{\delta^+}}$
548	0.20	0.2238	0.0191	16.9493
548	0.71	0.6205	0.0360	17.2386
548	1	0.7423	0.0427	17.3768
995	0.20	0.2256	0.0142	15.9124
995	0.71	0.4614	0.0267	17.2727
995	1	0.5484	0.0317	17.2985

The ramifications of this are that in layer I

$$\Theta^+ = Pry^+ + \frac{1}{\delta^{+2}}\bar{\Theta}, \tag{B.8}$$

and with

$$y^+ = O\left(\frac{1}{\sqrt{Pr\delta^+}}\right), \tag{B.9}$$

one gets

$$\begin{aligned} \Theta^+ &= PrO\left(\frac{1}{\sqrt{Pr\delta^+}}\right) + O\left(\frac{1}{\delta^{+2}}\right) \\ &= O\left(\sqrt{\frac{Pr}{\delta^+}}\right) + O\left(\frac{1}{\delta^{+2}}\right). \end{aligned} \tag{B.10}$$

Since, however, $O\left(\sqrt{\frac{Pr}{\delta^+}}\right) \gg O\left(\frac{1}{\delta^{+2}}\right)$, in the asymptotic limit

$$\Theta^+ = O\left(\sqrt{\frac{Pr}{\delta^+}}\right). \tag{B.11}$$

Albeit limited, the data of Table (B.1) seem to lend support for this semi-empirically based result. In this table, the value of $\Theta^+_{layer\,I}$ denotes the mean temperature increment

from the wall to the outer edge of layer I.

BIBLIOGRAPHY

Adrian, R., Meinhart, C., and Tomkins, C. (2000). Vortex organization in the outer region of the turbulent boundary layer. *J. Fluid Mech.*, 422:1–54.

Adrian, R. J. (2007). Hairpin vortex organization in wall turbulence. *Phys. Fluids*, 19(4):041301.

Afzal, N. (1982). Fully developed turbulent flow in a pipe: an intermediate layer. *Ingenieur-Archiv.*, 52(6):355–377.

Afzal, N. (1984). Mesolayer theory for turbulent flows. *AIAA journal*, 22:437–439.

Alfredsson, P. and Örlü, R. (2010). The diagnostic plota litmus test for wall bounded turbulence data. *Euro. J. Mech. B/Fluids*, 29(6):403–406.

Alfredsson, P., Segalini, A., and Örlü, R. (2011). A new scaling for the streamwise turbulence intensity in wall-bounded turbulent flows and what it tells us about the outer peak. *Phys. Fluids*, 23(4):041702.

Antonia, R. and Kim, J. (1994). Low-Reynolds-number effects on near-wall turbulence. *J. Fluid Mech.*, 276:61–80.

Bernardini, M., Pirozzoli, S., and Orlandi, P. (2014). Velocity statistics in turbulent channel flow up to $Re_\tau = 4000$. *J. Fluid Mech.*, 742:171–191.

Bradshaw, P. and Huang, G. P. (1995). The law of the wall in turbulent flow. In *Proc. R. Soc. London. Ser. A: Math. Phys. Sci.*, volume 451, pages 165–188. The Royal Society.

Castillo, L. and George, W. K. (2001). Similarity analysis for turbulent boundary layer with pressure gradient: outer flow. *AIAA journal*, 39:41–47.

Castro, I., Segalini, A., and Alfredsson, P. (2013). Outer-layer turbulence intensities in smooth-and rough-wall boundary layers. *J. Fluid Mech.*, 727:119–131.

Coleman, G., Kim, J., and Spalart, P. (2003). Direct numerical simulation of a decelerated wall-bounded turbulent shear flow. *J. Fluid Mech.*, 495:1–18.

Davidson, P. (2015). *Turbulence: An introduction for scientists and engineers*. Oxford University Press, USA.

De Graaff, D. and Eaton, J. (2000). Reynolds-number scaling of the flat-plate turbulent boundary layer. *J. Fluid Mech.*, 422:319–346.

Del Álamo, J. C., Jimenez, J., Zandonade, P., and Moser, R. D. (2006). Self-similar vortex clusters in the turbulent logarithmic region. *J. Fluid Mech.*, 561:329–358.

Eitel-Amor, G., Örlü, R., and Schlatter, P. (2014). Simulation and validation of a spatially evolving turbulent boundary layer up to $Re_\theta = 8300$. *Int. J. Heat Fluid Flow*, 47:57–69.

El Khoury, G., Schlatter, P., Noorani, A., Fischer, P., Brethouwer, G., and Johansson, A. (2013). Direct numerical simulation of turbulent pipe flow at moderately high Reynolds numbers. *Flow Turbul. Combust.*, 91:475–495.

Elsnab, J., Klewicki, J., Maynes, D., and Ameel, T. (2011). Mean dynamics of transitional channel flow. *J. Fluid Mech.*, 768:451–481.

Fernholz, H., Krause, E., Nockemann, M., and Schober, M. (1995). Comparative measurements in the canonical boundary layer at reδ2 6$\times$ 104 on the wall of the german–dutch windtunnel. *Phys. Fluids*, 7(6):1275–1281.

Fife, P., Klewicki, J., McMurtry, P., and Wei, T. (2005a). Multiscaling in the presence of indeterminacy: wall-induced turbulence. *Multiscale Model. Simul.*, 4(3):936–959.

Fife, P., Klewicki, J., and Wei, T. (2009). Time averaging in turbulence settings may reveal an infinite hierarchy of length scales. *J. Discrete Continuous Dyn. Syst.*, 24:781–807.

Fife, P., Wei, T., Klewicki, J., and McMurtry, P. (2005b). Stress gradient balance layers and scale hierarchies in wall-bounded turbulent flows. *J. Fluid Mech.*, 532:165–189.

George, W. K. and Castillo, L. (1997). Zero-pressure-gradient turbulent boundary layer. *Appl. Mech. Rev.*, 50:689–729.

Gowen, R. and Smith, J. (1967). The effect of the prandtl number on temperature profiles for heat transfer in turbulent pipe flow. *Chem. Eng. Sci*, 22:1701–1711.

Hoyas, S. and Jiménez, J. (2008). Reynolds number effects on the Reynolds-stress budgets in turbulent channels. *Phys. Fluids*, 20(10):101511.

Hutchins, N., Nickels, T., Marusic, I., and Chong, M. (2009). Hot-wire spatial resolution issues in wall-bounded turbulence. *J. Fluid Mech.*, 635:103–136.

Izakson, A. (1937). On the formula for the velocity distribution near walls. *Tech. Phys. USSR IV*, 2:155–162.

Kader, B. (1981). Temperature and concentration profiles in fully turbulent boundary layers. *Int. J. Heat Mass Transfer*, 24:1541–1544.

Kader, B. (1991). Heat and mass transfer in pressure-gradient boundary layers. *Int. J. Heat Mass Transfer*, 34:2837–2857.

Kader, B. and Yaglom, A. (1972). Heat and mass transfer laws for fully turbulent wall flows. *Int. J. Heat Mass Transfer*, 15:2329–2351.

Kawamura, H., Abe, H., and Matsuo, Y. (1999). Dns of turbulent heat transfer in channel flow with respect to reynolds and prandtl number effects. *Int. J. Heat Fluid Flow*, 20:196–207.

Klebanoff, P. (1955). *Characteristics of turbulence in a boundary layer with zero pressure gradient*. NACA Rep. 1247.

Klewicki, J. (2010). Reynolds number dependence, scaling, and dynamics of turbulent boundary layers. *J. Fluids Eng.*, 132(9):094001.

Klewicki, J. (2013a). A description of turbulent wall-flow vorticity consistent with mean dynamics. *J. Fluid Mech.*, 737:176–204.

Klewicki, J. (2013b). Self-similar mean dynamics in turbulent wall flows. *J. Fluid Mech.*, 718:596–621.

Klewicki, J., Chin, C., Blackburn, H., Ooi, A., and Marusic, I. (2012). Emergence of the four layer dynamical regime in turbulent pipe flow. *Phys. Fluids*, 24(4):045107.

Klewicki, J., Ebner, R., and Wu, X. (2011). Mean dynamics of transitional boundary-layer flow. *J. Fluid Mech.*, 682:617–651.

Klewicki, J. and Falco, R. (1990). On accurately measuring statistics associated with small-scale structure in turbulent boundary layers using hot-wire probes. *J. Fluid Mech.*, 219:119–142.

Klewicki, J., Fife, P., and Wei, T. (2009). On the logarithmic mean profile. *J. Fluid Mech.*, 638:73–93.

Klewicki, J., Morrill-Winter, C., and Zhou, A. (2015). Inertial logarithmic layer properties and self-similar mean dynamics. *TSFP-9*, 3A:4.

Klewicki, J. and Oberlack, M. (2015). Finite reynolds number properties of a turbulent channel flow similarity solution. *Phys. Fluids*, 27(9):095110.

Klewicki, J., Philip, J., Marusic, I., Chauhan, K., and Morrill-Winter, C. (2014). Self-similarity in the inertial region of wall turbulence. *Phys. Rev. E*, 90(6):063015.

Kolmogorov, A. (1941). The local structure of turbulence in incompressible viscous fluid for very large reynolds numbers. In *Dokl. Akad. Nauk SSSR*, volume 30, pages 301–305.

Kullback, S. and Leibler, R. (1951). On information and sufficiency. *Ann. Math. Stats.*, 22:79–86.

Landau, L. and Lifshitz, E. (2013). *Course of theoretical physics*. Elsevier.

Laufer, J. (1951). *Investigation of turbulent flow in a two-dimensional channel*. NACA Rep. 1053.

Laufer, J. (1954). *The structure of turbulence in full developed pipe flow*. NACA Rep. 1174.

Lee, M. and Moser, R. (2015). Direct numerical simulation of turbulent channel flow up to $Re_\tau = 5200$. *J. Fluid Mech.*, 774:395–415.

Lindgren, B., Johansson, A., and Tsuji, Y. (2004). Universality of probability density distributions in the overlap region in high reynolds number turbulent boundary layers. *Phys. Fluids*, 16:2587–2591.

Long, R. and Chen, T.-C. (1981). Experimental evidence for the existence of the meso-layerin turbulent systems. *J. Fluid Mech.*, 105:19–59.

Mansour, N., Kim, J., and Moin, P. (1988). Reynolds-stress and dissipation-rate budgets in a turbulent channel flow. *J. Fluid Mech.*, 194:15–44.

Marusic, I., McKeon, B., Monkewitz, P., Nagib, H., Smits, A., and Sreenivasan, K. (2010). Wall-bounded turbulent flows at high Reynolds numbers: Recent advances and key issues. *Phys. Fluids*, 22(6):065103.

Marusic, I., Monty, J., Hultmark, M., and Smits, A. (2013). On the logarithmic region in wall turbulence. *J. Fluid Mech.*, 716:R3.

Mehdi, F., Klewicki, J., and White, C. (2013). Mean force structure and its scaling in rough-wall turbulent boundary layers. *J. Fluid Mech.*, 731:682–712.

Meinhart, C. and Adrian, R. (1995). On the existence of uniform momentum zones in a turbulent boundary layer. *Phys. Fluids*, 7:694–696.

Meneveau, C. and Marusic, I. (2013). Generalized logarithmic law for high-order moments in turbulent boundary layers. *J. Fluid Mech.*, 719:R1.

Metzger, M. and Klewicki, J. (2001). A comparative study of near-wall turbulence in high and low reynolds number boundary layers. *Phys. Fluids*, 13:692–701.

Millikan, C. (1938). A critical discussion of turbulent flows in channels and circular tubes. In *Proc. 5th Int. Cong. Appl. Mech*, pages 386–392.

Morrill-Winter, C., Philip, J., and Klewicki, J. (2017). An invariant representation of mean inertia: theoretical basis for a log law in turbulent boundary layers. *J. Fluid Mech.*, 813:594–617.

Moser, R., Kim, J., and Mansour, N. (1999). Direct numerical simulation of turbulent channel flow up to $Re = 590$. *Phys. Fluids*, 11:943–945.

Örlü, R. (2009). *Experimental studies in jet flows and zero pressure-gradient turbulent boundary layers*. PhD thesis, KTH.

Österlund, J. (1999). *Experimental studies of zero pressure-gradient turbulent boundary layer flow*. Royal Institute of Technology, Department of Mechanics.

Panton, R. (2005). Review of wall turbulence as described by composite expansions. *Appl. Mech. Rev.*, 58:1–36.

Perry, A. and Marusic, I. (1995). A wall-wake model for the turbulence structure of boundary layers. part 1. extension of the attached eddy hypothesis. *J. Fluid Mech.*, 298:361–388.

Perry, A. E. and Chong, M. S. (1982). On the mechanism of wall turbulence. *J.Fluid Mech.*, 119:173C217.

Pirozzoli, S., Bernardini, M., and Orlandi, P. (2016). Passive scalars in turbulent channel flow at high reynolds number. *J.Fluid Mech.*, 788:614–639.

Pope, S. (2000). *Turbulent flows*. Cambridge university press.

Prandtl, L. (1925). Bericht über untersuchungen zur ausgebildeten turbulenz. *Z. Angew. Math. Mech*, 5:136–139.

Priyadarshana, P., Klewicki, J., Treat, S., and Foss, J. (2007). Statistical structure of turbulent-boundary-layer velocity–vorticity products at high and low reynolds numbers. *J. Fluid Mech.*, 570:307–346.

Saha, S., Klewicki, J., Ooi, A., Blackburn, H., and Wei, T. (2014). Scaling properties of the equation for passive scalar transport in wall-bounded turbulent flows. *Int. J. Heat Mass Transfer*, 70:779–792.

Schlatter, P. and Örlü, R. (2010). Assessment of direct numerical simulation data of turbulent boundary layers. *J.Fluid Mech.*, 659:116–126.

Seena, A. and Afzal, N. (2008). Intermediate scaling of turbulent momentum and heat transfer in a transitional rough channel. *J. Heat Transfer*, 130(3):031701.

Shannon, C., C. and Weaver, W. (1949). The mathematical theory of communication. *Univ. Illinois*, 19:1.

Smits, A., McKeon, B., and Marusic, I. (2011a). High-reynolds number wall turbulence. *Ann. Rev. Fluid Mech.*, 43:353–375.

Smits, A., Monty, J., Hultmark, M., Bailey, S., Hutchins, N., and Marusic, I. (2011b). Spatial resolution correction for wall-bounded turbulence measurements. *J. Fluid Mech.*, 676:41–53.

Spalart, P. (1988). Direct simulation of a turbulent boundary layer up to $R_\theta = 1410$. *J. Fluid Mech.*, 187:61–98.

Tennekes, H. and Lumley, J. (1972). *A first course in turbulence.* MIT Press.

Tennekes, H. and Lumley, J. (1976). *The structure of turbulent shear flow.* Cambridge University Press.

Townsend, A. (1961). Equilibrium layers and wall turbulence. *J.Fluid Mech.*, 11:97–120.

Townsend, A. (1980). *The structure of turbulent shear flow*. Cambridge university press.

Tsuji, Y., Lindgren, B., and Johansson, A. (2005). Self-similar profile of probability density functions in zero-pressure gradient turbulent boundary layers. *Fluid Dyn. Res.*, 37:293–316.

Tsuji, Y. and Nakamura, I. (1999). Probability density function in the log-law region of low reynolds number turbulent boundary layer. *Phys. Fluids*, 11:647–658.

Vincenti, P., Klewicki, J., Morrill-Winter, C., White, C., and Wosnik, M. (2013). Streamwise velocity statistics in turbulent boundary layers that spatially develop to high reynolds number. *Exp. Fluids*, 54:1–13.

Wei, T., Fife, P., and Klewicki, J. (2007). On scaling the mean momentum balance and its solutions in turbulent Couette–Poiseuille flow. *J.Fluid Mech.*, 573:371–398.

Wei, T., Fife, P., Klewicki, J., and McMurtry, P. (2005a). Properties of the mean momentum balance in turbulent boundary layer, pipe and channel flows. *J.Fluid Mech.*, 522:303–327.

Wei, T., Fife, P., Klewicki, J., and McMurtry, P. (2005b). Scaling heat transfer in fully developed turbulent channel flow. *Int. J. Heat Mass Transfer*, 48:5284–5296.

Wosnik, M., Castillo, L., and George, W. (2000). A theory for turbulent pipe and channel flows. *J.Fluid Mech.*, 421:115–145.

Yaglom, A. (1979). Similarity laws for constant-pressure and pressure-gradient turbulent wall flows. *Annu. Rev. Fluid Mech.*, 11:505–540.

Zhou, A. and Klewicki, J. (2015). Properties of the streamwise velocity fluctuations in the inertial layer of turbulent boundary layers and their connection to self-similar mean dynamics. *Int. J. Heat Fluid Flow*, 51:372–382.

Zhou, A. and Klewicki, J. (2016). Properties of the kinetic energy budgets in wall-bounded turbulent flows. *Phys. Rev. Fluids*, 1(4):044408.

Zhou, A., Pirozzoli, S., and Klewicki, J. (2017). Mean equation based scaling analysis of fully-developed turbulent channel flow with uniform heat generation. *Int. J. Heat Mass Transfer*, 115:50–61.